DISSERTATION

Titel der Dissertation

Low-frequency variability in global energy budgets

verfasst von

Mag. Michael Mayer

angestrebter akademischer Grad

Doktor der Naturwissenschaften (Dr. rer. nat.)

Wien, 2014

Abstract

Quantification of the global atmospheric and oceanic energy budgets is one major branch of climate research. Especially the variability of the budgets on various timescales is of great interest for fundamental research but also for climate change research. For example, validation of climate models requires sound observational estimates as reference. The two main aims of this study are to (i) give a new estimate of poleward atmospheric energy transports and (ii) to describe the variability of atmospheric and oceanic energy budgets in association with El Niño-Southern Oscillation (ENSO).

The first part of this thesis is concerned with the atmospheric energy budget as evaluated from the European Centre for Medium-Range Weather Forecasts (ECMWF) Re-Analysis Interim (ERA-Interim). Based on this state-of-the-art dataset, a new estimate of climatological mean poleward atmospheric energy transports is given. While results for peak transports in the Northern Hemisphere agree well with earlier estimates, results for the Southern Hemisphere suggest stronger mean atmospheric poleward transports than earlier studies. Moreover, several aspects regarding physical consistency and temporal homogeneity of the ERA-Interim dataset are discussed.

The second part of this thesis deals with the zonal structure of tropical atmospheric energy budget anomalies in association with ENSO. Results show strong zonal compensation of budget anomalies, for example in the fields of the divergence of total energy, dry-static energy and latent heat transports, during warm and cold ENSO events. For the transition period between warm and cold ENSO state, novel eastward propagating anomaly patterns are documented. The coherence of these patterns emphasizes the tendency of the atmosphere to compensate for tropical diabatic heating anomalies via heating anomalies of opposite sign in other regions in the tropics, realized via anomalous zonal circulation anomalies (atmospheric bridge).

For the third part of this thesis, the energy budget of the ocean is included in the diagnostic framework. It is found that on the scale of tropical ocean basins, the signal-to-noise ratio of current oceanic datasets is high enough to reasonably quantify energy exchanges between ocean and atmosphere in association with ENSO. Results show that the tropical Pacific expectably loses (gains) energy during El Niño (La Niña). However, only a relatively small fraction (15%) of this energy is exchanged immediately via net radiation at top of the atmosphere (TOA) or transported to the extratropics. It is shown that instead tropical Atlantic and Indian Oceans gain (lose) energy during El Niño (La Niña), almost fully accounting (85%) for the Pacific ocean heat content (OHC) variations during peak ENSO. These apparent energy exchanges between tropical ocean basins is mainly due to changes in net surface energy flux as a response to changed atmospheric conditions, which is a manifestation of the atmospheric bridge communicating ENSO signals across the tropical belt. A few months after peak ENSO the net radiative signal at TOA becomes stronger while the response of the atmospheric bridge weakens as SSTs in the Indian and Atlantic change due to the altered surface fluxes. As a consequence, the strength of the observed OHC exchanges also ceases.

This thesis contributes to our understanding of large-scale climate dynamics and also provides results which can serve as a quantitative benchmark for validation of coupled climate models.

Zusammenfassung

Die Quantifizierung globaler atmosphärischer und ozeanischer Energiehaushalte ist ein wichtiges Teilgebiet der Klimaforschung. Besonders die Variabilität dieser Haushalte ist von großem Interesse für die Grundlagenforschung und auch für die Erforschung des globalen Klimawandels, denn die Validierung globaler Klimamodelle erfordert glaubwürdige Referenzwerte. Die zwei Hauptziele dieser Dissertation sind (i) eine neue Abschätzung des mittleren polwärtigen atmosphärischen Energietransports und (ii) die Erforschung der Variabilität der atmosphärisch-/ozeanischen Energiehaushalte im Zusammenhang mit El Niño-Southern Oscillation (ENSO).

Der erste Teil der vorliegenden Arbeit betrachtet den Energiehaushalt der Atmosphäre unter Verwendung von "European Re-Analysis Interim" (ERA-Interim), dem aktuellen Reanalyseprodukt des Europäischen Zentrums für mittelfristige Wettervorhersage (EZMW). Auf Grundlage dieses modernen Datensatzes wird der zeitgemittelte polwärtige Energietransport in der Atmosphäre neu abgeschätzt. Das Transportmaximum in der Nordhemisphäre stimmt gut mit früheren Studien überein, die Ergebnisse für die Südhemisphäre deuten jedoch auf ein stärkeres Maximum als bisher angenommen hin. Darüber hinaus werden Aspekte der physikalischen Konsistenz und der zeitlichen Homogenität von ERA-Interim diskutiert.

Der zweite Teil dieser Dissertation beschäftigt sich mit der zonalen Struktur tropischer atmosphärischer Energiehaushaltsanomalien im Zusammenhang mit ENSO. Anomalien der Divergenz von totalem Energie-, trocken-statischem Energie- und latentem Wärmetransport zeigen starke zonale Kompensation während warmer und kalter ENSO-Ereignisse. Für die Übergangsphasen zwischen warmen und kalten ENSO-Ereignissen werden neue ostwärts wandernde Anomaliestrukturen dokumentiert. Die bemerkenswerte Kohärenz dieser Strukturen verdeutlicht die Eigenschaft der Atmosphäre, regionale Anomalien der diabatischen Heizung in den Tropen mit Anomalien mit umgekehrtem Vorzeichen in anderen tropischen Regionen zu kompensieren. Diese regionalen Anomalien hängen dynamisch über Anomalien der tropischen zonalen Zirkulation zusammen (in der Literatur oft als "atmosphärische Brücke" bezeichnet).

Im dritten Teil dieser Arbeit wird dem diagnostischen Konzept zusätzlich der ozeanische Energiehaushalt hinzugefügt, um Energieaustäusche zwischen Atmosphäre und Ozean im Zusammenhang mit ENSO auf der Skala tropischer Ozeanbecken zu quantifizieren. Die Ergebnisse zeigen, dass der ozeanische (thermische) Energiegehalt im tropischen Pazifik während El Niño (La Liña) ab- (zu-)nimmt . Es wird jedoch nur ein relativ kleiner Teil der freigesetzten (gespeicherten) Energie (15%) direkt am Oberrand der Atmosphäre ausgetauscht oder in die Extratropen transportiert. Stattdessen nimmt der ozeanische Energiegehalt des tropischen indischen Ozeans und Atlantik während El Niño (La Liña) stark zu (ab) (zusammen 85% der Änderungsrate im Pazifik). Dieser Energieaustausch zwischen den tropischen Ozeanbecken geschieht durch Änderungen im Nettooberflächenfluss als Reaktion auf die veränderte atmosphärische Zirkulation. Dies ist eine Auswirkung der "atmosphärischen Brücke", über die ENSO-Signale innerhalb der Tropen kommuniziert werden. Einige Monate nach dem Höhepunkt des jeweiligen ENSO-Ereignisses nimmt der Energieaustausch am Oberrand der Atmosphäre im Gebiet des tropischen Pazifik zu. Gleichzeitig schwächen die in Folge der geänderten Nettooberflächenflüsse veränderten Meeresoberflächentemperaturen im tropischen Indischen Ozean und Atlantik die Auswirkung der "atmosphärischen Brücke" ab. Deshalb schwächt sich zu diesem Zeitpunkt auch der Austausch des ozeanischen Energiegehaltes ab.

Die Ergebnisse dieser Dissertation tragen zum Verständnis großskaliger Klimadynamik bei und liefern neue Referenzwerte für die Validierung gekoppelter globaler Klimamodelle.

Contents

1 Introduction

The climate system, i.e., the earth and its atmosphere, as a very good approximation can be described as a closed physical system, which exchanges energy, but not matter with its surroundings. This energy exchange is established in the form of net solar radiation arriving (ASR) from the sun and outgoing longwave radiation (OLR), emitted from the atmosphere and the earth's surface. In contrast, the earth's climate system can be subdivided, with little arbitrariness, into five components atmosphere, hydrosphere, cryosphere, lithosphere, and biosphere, which all exchange energy, matter, and momentum on various spatial and temporal time scales, thus representing open physical systems. For example, energy (in the form of latent heat) and matter (in the form of water) are exchanged between hydrosphere and atmosphere during evaporation and precipitation, and momentum exchange between atmosphere and ocean is a main driver of the ocean circulation. Energy, matter, and momentum are also moved around within the climate components, most prominently within the atmosphere by the wind, but also in the ocean by its currents (Peixoto and Oort, 1992).

This thesis is concerned with quantitive diagnostics of energy transports and energy storage within the climate system. For this purpose, energy budgets in a vertically integrated framework are considered. Vertical integration of the three-dimensional budget equations simplifies the problem because the equations reduce to vertically integrated horizontal transports and vertically integrated storage of energy within the respective component. Moreover, vertical fluxes of energy reduce to energy fluxes across the vertical boundaries of the respective component which are much easier to determine than vertical fluxes *within* the respective component.

The main focus of this thesis is on interannual variability, i.e., variations on time scales which are longer than seasons but shorter than decades, of energy budgets in tropical regions. The considerations here are limited to the atmosphere and the hydrosphere (represented by the ocean), as these two components are the main drivers of tropical climate variability on the considered timescales. The other components, especially the cryosphere, also exhibit strong impact on global climate and its variability, but as this work has a focus on interannual tropical climate variability, those are not included in the diagnostic framework presented herein.

The prime cause for the existence of horizontal and especially poleward energy transports is the earth's spherical geometry and the resulting differential heating, i.e., tropical regions receive by far more energy through ASR than polar regions. A meridional gradient can also be found in OLR due to the meridional atmospheric temperature gradient, but it is weaker than the ASR gradient. This is the case mainly because the tropics are cooler than expected from ASR and the polar regions are warmer than expected from ASR. Additionally, OLR is also influenced by upper tropospheric moisture content. As a consequence, OLR in the tropics is weaker than expected from local temperatures due to high values of upper tropospheric moisture, while OLR in polar regions is relatively high due to low atmospheric moisture content (Pierrehumbert,

2010). Thus, in sum the climate system in the long-term average gains energy in the form of net radiation (ASR minus OLR) at top of the atmosphere (TOA) in the tropics and loses energy at TOA at the poles. This local imbalance of energy input into the system must be compensated, otherwise the tropics would continuously warm and the polar regions would cool, which would be at odds with observations of (to a large degree) locally stable climate. The observed energy balance is maintained by horizontal poleward energy transports within the atmosphere and ocean (Lorenz, 1967).

Net radiation at TOA and hence also the required poleward energy transport by the geofluids (atmosphere plus ocean) is known quite precisely from satellite measurements [e.g., from the Clouds and the Earth's Radiant Energy System (CERES, Wielicki et al. 1996)], see, e.g., Fasullo and Trenberth (2008b). However, the partitioning between atmospheric and oceanic contribution to the total poleward energy transport is known much less precisely and more difficult to determine, but these are fundamental quantities of the climate system (see, e.g., Czaja and Marshall 2006 or Held 2001). Realistic estimates of time mean poleward energy transports within the atmosphere and ocean are necessary for evaluation of global climate models. For example, modeled poleward energy transports which are different from the observed values can indicate model biases such as too weak or too few extratropical cyclones, see, e.g., Trenberth and Fasullo (2010).

The partitioning of these transports can be estimated either (i) by evaluation of the horizontal transports within the respective component or (ii) from the poleward transport implied from net radiation at TOA and the net energy flux at the atmosphere's lower boundary (the sum of radiative energy fluxes as well as turbulent sensible and latent heat fluxes). A third approach (iii) is a combination of (i) and (ii), i.e., oceanic heat transport is determined from the difference of required transport by the geofluids as implied from net radiation at TOA and atmospheric energy transport. Approaches (i), (ii) and (iii) are shortly outlined below, and the well established theory behind these approaches is described in section 2.

Atmospheric energy transport can be computed directly if fields of the required atmospheric state quantities pressure, wind, temperature, and moisture are known. This has been pioneered by Oort (1971) employing radiosonde data, but the spatial and temporal resolution of these data is too coarse to yield reasonable results, especially over the oceans and generally in the Southern Hemisphere. However, radiosonde data are still employed for evaluation of atmospheric energy transports across certain well-observed atmospheric cross-sections such as 70°N (see, e.g., Göber et al. 2003 or Sorokina and Esau 2011), providing valuable estimates purely from in-situ data. Computation of global atmospheric energy transports has been enormously facilitated by the availability of atmospheric reanalyses. These datasets provide a best estimate of the atmospheric state gridded in space (typically $\Delta x \simeq 80$km) and time (Δt typically 6 hours) using a fixed data assimilation system, which combines observations and model forecasts in a

dynamically consistent way. Many studies dealing with atmospheric poleward energy transports as evaluated from reanalyses have been published over the past two decades (e.g., Michaud and Derome 1991, Trenberth et al. 2001, or Hantel et al. 2005).

Oceanic reanalyses have become available recently (e.g., the Ocean Reanalysis System 4, see Balmaseda et al. 2012), and hence direct computation of ocean heat transport is now also possible (see, e.g., Haines et al. 2012). However, many regions of the world's ocean are not well observed, especially in the period prior to the introduction of the ARGO float (a global array of currently more than 3500 temperature and salinity profiling floats) in 2000. This leads to considerable model dependency of reanalyzed ocean fields in these data-sparse regions. Prior to the availability of ocean reanalyses, studies attempted to estimate oceanic heat transport from direct measurements (see, e.g., Bryden and Hall 1980). This method is accurate and still employed (see, e.g., Johns et al. 2011) but direct estimates require a dense observation system. Thus, estimates of ocean heat transport from observations are mostly limited to transports across certain cross-sections (e.g., Atlantic at 26.5°N).

Approach (ii) to obtain the partitioning of total poleward energy transports requires, besides net radiation at TOA, the net energy exchanges at the ocean surface to be known precisely. Direct measurements of surface fluxes are only very scarcely available and usually are obtained from parameterized formulas, i.e., from other better observable quantities such as wind speed, humidity and sea surface temperature, resulting in large uncertainties. A principal advantage of this approach is avoidance of the use of data from *within* the atmosphere and ocean. However, approach (ii) in this simple form is only suitable for evaluation of time mean transports. If the annual cycle or variability of the transports is to be explored, the local energy storage term and thus data from within the atmosphere and ocean has to be included.

The large uncertainties of net surface flux estimates represent the main difficulty associated with approach (ii), and due to the lack of global ocean (re-)analyses until recently approach (i) has not been viable for a long time. Hence, many authors chose approach (iii). Vonder Haar and Oort (1973) combined early satellite measurements at TOA and atmospheric transports as evaluated from radiosonde data. More recently, Trenberth and Fasullo (2008) combined net radiation at TOA from CERES with atmospheric transports as evaluated from atmospheric reanalyses. See Fig. 1 for an illustration of energy transports and fluxes across the horizontal and vertical boundaries of the atmospheric and oceanic domain.

Despite the great number of published studies (those cited herein and many others) employing the different approaches as outlined above, there is no definitive estimate of climatological mean poleward energy transports neither in the atmosphere nor the oceans (Stone, 2008), but at least estimates have been converging in recent decades. Regarding the partitioning between the transports in the geofluids, there is at least consensus that atmospheric and oceanic poleward energy transports are of similar size in the tropics, while atmospheric transports clearly
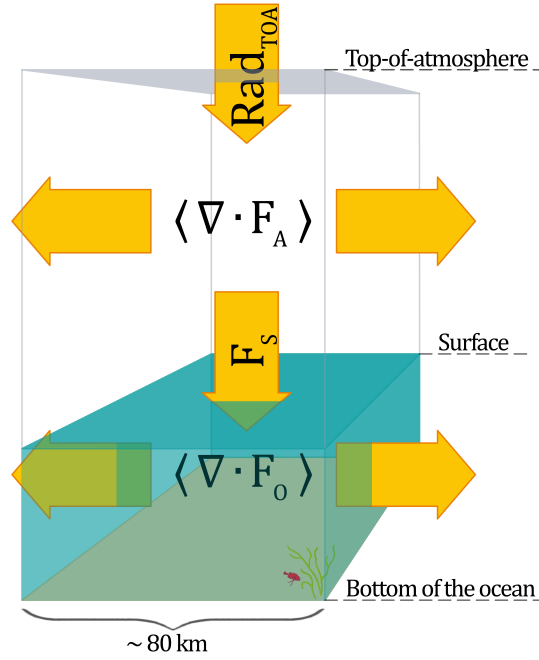
Figure 1: Schematic of net energy fluxes across vertical boundaries [net radiation at TOA (Rad_{TOA}) and net surface flux (F_S)] and vertically integrated horizontal transports out [denoted by the divergence of atmospheric and oceanic energy transport (F_A and F_O, respectively)] of an atmospheric and oceanic column (please see section 2 for equations and a more detailed description of the terms). The horizontal extent of the column represents the typical resolution of current global reanalysis products. Note how the different fluxes can be combined to obtain either the implied total energy transports by the geofluids (atmosphere plus ocean) or to obtain the horizontal energy transport by the individual components, as outlined in the text by approaches (i) to (iii). Note also that this schematic is only valid for the climatological mean of the column. Consideration of the annual cycle or budget variability requires to include a storage term in each component.

dominate in the extratropics (Fasullo and Trenberth, 2008b).

Climate variability is reflected in anomalous variability, i.e., anomalies of a state or flux quantity after removing the average annual cycle, of atmospheric and oceanic energy budgets, including storage terms. Variability of atmospheric energy storage is small in the tropics because of the small heat capacity of air (Trenberth, 2002), but ocean heat content (OHC) varies substantially (Balmaseda et al., 2013). The most important drivers of OHC changes on interannual timescales are volcanic eruptions and El Niño-Southern Oscillation (ENSO), the primary mode of global climate variability, with its origin in the tropical Pacific region (Trenberth et al., 2014). During warm ENSO events (El Niño) the Pacific loses energy, mainly to the atmosphere due to evaporation as a result of higher sea surface temperatures (SSTs) than normal in the eastern equatorial Pacific and altered wind conditions (Trenberth, 2002). El Niños are usually followed by cold ENSO events (La Niña), during which Pacific OHC increases again. These ENSO-related OHC changes are described conceptionally by an ocean recharge/discharge oscillator model by Jin (1997). Due to the changes in the SST field as well as altered precipitation and

consequently altered diabatic heating patterns, atmospheric circulation responds to ENSO with global effect. The term teleconnections was coined to describe these remote changes (Bjerknes, 1969).

As reanalyses cover a relatively long period of time (up to 100 years), it is not only possible to estimate time-averaged energy transports and exchanges but also to explore the temporal variability of energy transports within atmosphere and ocean. While climatological mean considerations require an as small as possible time-averaged bias of the employed data, exploration of variability requires also high temporal homogeneity, because artificial shifts in the data can cause erroneous shifts in the computed transports and fluxes. The main problem in this respect is the permanently changing observing system (e.g., changes of satellite data coverage or changes of radiosonde instruments) which leads to temporal changes of the input data for the reanalysis. Widespread efforts to account for these imperfect data [e.g., homogenization of radiosonde data (Haimberger, 2007) or variational bias correction (Dee and Uppala, 2009)] have improved the quality of current third generation atmospheric reanalyses compared to earlier products, but temporal homogeneity remains an important issue (see, e.g., Chiodo and Haimberger 2010, Dee et al. 2011, or Mayer and Haimberger 2012).

The first main goal set in the exposé of this thesis was to provide a new estimate of climatological mean poleward energy transports by the atmosphere, based on a state-of-the-art reanalysis dataset. Therefore, data from ERA-Interim (ERA-I, Dee et al. 2011), the most recent reanalysis of the European Centre for Medium-Range Weather Forecasts (ECMWF), have been employed and pre-existing evaluation methods have been refined to optimally use the available data. Results of this part of the thesis were published in Mayer and Haimberger (2012) and are presented in section 3. The second main goal of this thesis concerns interannual variability of atmospheric budgets in association with ENSO, motivated by the observation of eastward propagating anomalies of the atmospheric energy budget in association with ENSO, first presented in Mayer and Haimberger (2012). Results of a study exploring the zonal structure of atmospheric energy budget anomalies and especially their temporal evolution were published in Mayer et al. (2013) and are presented in section 4. During this work it became apparent that inclusion of oceanic heat budgets to the diagnostic framework was necessary in order to get a more holistic perspective of how atmosphere and ocean interact in terms of energy exchanges in association with ENSO. A quantitative assessment of pathways of energy through atmosphere and ocean is lacking in literature (Trenberth and Fasullo, 2012), mainly due to shortcomings in available data regarding spatial and temporal coverage. With state-of-the-art datasets for atmosphere and ocean energy exchanges between tropical ocean basins via the atmosphere in association with ENSO can be quantified. These novel results are documented in Mayer et al. (2014) and are presented in section 5.

The following sections contain complimentary information about the employed methods

(section 2), the three journal articles (sections 3, 4 and 5), a discussion bringing together the ideas and results of the three research papers (section 6), and a short outlook (section 7). A description of the employed datasets is given in the respective journal publications.

2 Methods

This section gives an introduction to the methods employed for evaluation of the atmospheric and oceanic energy budgets. The vertically integrated budget equations for atmosphere and ocean are described in sections 2.1 and 2.3, respectively. Issues complicating the budget evaluation, namely the mass budget in atmospheric reanalyses and evaluation of ocean heat content and the divergence of ocean enthalpy transport are discussed in some detail in sections 2.2, 2.4, and 2.5.

2.1 The vertically integrated energy budget of the atmosphere

Atmospheric energy exists in various forms, internal energy, potential energy, latent heat, and kinetic energy, the sum of which is referred to as total atmospheric energy. The sum of sensible heat (enthalpy), potential energy, and latent heat is referred to as moist static energy. The divergence of vertically integrated transport of atmospheric moist static plus kinetic energy out of an atmospheric column [TEDIV, left term in equation (2.1)] is balanced by local storage of total atmospheric energy [first term on the right-hand side of equation (2.1)], surface fluxes in the form of latent heat flux (LH) through evaporation, sensible heat flux (SH), net radiation at the surface (Rad_S), and net radiation at top of the atmosphere (Rad_{TOA}, vertical fluxes are defined as positive downward):

$$\frac{1}{g} \int_0^{p_s} \left[\nabla \cdot (c_p T + \Phi + Lq + k) v_2 \right] dp =$$

$$= -\frac{1}{g} \frac{\partial}{\partial t} \int_0^{p_s} (c_p T + \Phi_s + Lq + k) dp - LH - SH - Rad_s + Rad_{TOA}. \tag{2.1}$$

Here, g denotes the gravitational acceleration, p pressure (the subscript S means surface), c_p the specific heat at constant pressure, T temperature, Φ geopotential height , L the phase transition energy for evaporation, q specific humidity, k specific kinetic energy, and v_2 the horizontal wind. Note that the term on the lhs is the vertically integrated divergence of moist static plus kinetic energy, whereas the first term on the rhs denotes the vertically integrated total energy tendency. A derivation of this equation can be found in Nielsen and Chen (1993). Units are Wm^{-2}. Net radiation at TOA and at the surface can be decomposed into down- and upwelling solar and thermal radiation, but we will stay with the net radiation for most parts of this thesis.

To obtain a shorter form of equation (2.1), we introduce abbreviations F_A for the horizontal transport of moist static plus kinetic energy, e for total atmospheric energy, F_S for the net

7

surface flux (the sum of LH, SH and Rad_S), and a vertical integration operator which is defined as follows:

$$\frac{1}{g} \int\limits_0^{p_s} f(p)\,dp = \langle f(p) \rangle. \tag{2.2}$$

Therefore, equation (2.1) can be written more shortly as:

$$\langle \nabla \cdot F_A \rangle = -\frac{\partial \langle e \rangle}{\partial t} - F_S + Rad_{TOA}, \tag{2.3}$$

see also Fig. 1 for illustration. It is noted that instead of TEDIV the acronym DIVFA is used in Mayer et al. (2014). All other acronyms are used consistently throughout all sections of this thesis.

The divergence of atmospheric energy transport (short for moist static plus kinetic energy transport) can be determined either by evaluation of the left or right-hand side of equation (2.1). Evaluation of the left-hand side (direct method) requires atmospheric state quantities with a sufficiently high temporal resolution in order to resolve eddy transports. For example, ERA-Interim provides analyzed fields with a six-hourly time resolution, which is sufficient for this task. However, the instantaneous mass flux field exhibits unrealistic divergence patterns, which make the results seriously flawed when computed from un-adjusted fields. This problem was recognized already by Hantel and Haase (1983), and subsequent studies of the atmospheric energy budget employed various approaches to adjust the wind field to obtain more realistic results (see, e.g., Trenberth and Caron 2001, Hantel et al. 2005, or Mayer and Haimberger 2012). An illustration of this issue and the here employed adjustment method are given in 2.2.

An alternative approach to determine TEDIV is evaluation of the right-hand side of equation (2.1) (indirect method). The energy tendency term can be obtained from reanalyses, and the vertical fluxes can be obtained either from independent data sets (e.g., satellite data for Rad_{TOA}) or also from reanalyses. When using reanalyses data exclusively for all three terms, the results depend on the assimilating model (vertical fluxes from reanalyses are short term model forecasts rather than instantaneous analyses). For ERA-Interim, we employ twelve-hourly forecasts of vertical fluxes (radiative and turbulent) and, to be consistent and to close the budget, twelve-hourly energy tendency forecasts. When combining different data sets for the indirect method, model dependency is decreased, but the energy budget will generally not be closed, i.e., the global mean of the obtained TEDIV will be unequal zero. The disadvantages and advantages of the direct and indirect methods are discussed in more detail in Mayer and Haimberger (2012).

The divergence of vertically integrated moisture transport in the atmosphere is governed by storage of total column water $\frac{\partial}{\partial t}\langle q \rangle$ as well as by the sum of precipitation P and evaporation E (fresh water flux, the uncommon sign convention arises from consequently considering all

vertical fluxes to be positive downward). While the right-hand side of equation (2.1) consists of storage and energy fluxes across the vertical boundaries of the atmosphere, the moisture budget involves a conversion term, namely precipitation:

$$\frac{1}{g} \int_0^{p_s} [\nabla \cdot (v_2 q)] \, dp = -\frac{1}{g} \frac{\partial}{\partial t} \int_0^{p_s} q \, dp - E - P. \tag{2.4}$$

Units of equation (2.4) are kgm^{-2}s^{-1}, multiplication by the latent heat of vaporization L yields the equation for the divergence of latent heat transport (LEDIV) with units of Wm^{-2}. Analogously to equation (2.1), the divergence of moisture transport can be computed directly or indirectly, i.e., either by evaluation of the left or right-hand side of equation (2.4), with similar disadvantages and advantages. The difference of the equations for TEDIV and LEDIV yields an equation for the divergence of dry-static energy transport (DSEDIV).

After determining divergences of total energy and latent heat transports, transports themselves can be obtained using the spectral method (Mayer, 2010). First, the inverse Laplacian is applied on the respective divergence field. The zonal and meridional derivatives of the obtained potential field then represent the zonal and meridional divergent energy transports, respectively.

2.2 Mass budget in ERA-Interim

As outlined in Mayer and Haimberger (2012), a mass flux adjustment is necessary for both the direct and indirect evaluation methods. Here we illustrate this issue and begin the excursion with the vertically integrated mass budget of the atmosphere:

$$\frac{1}{g} \int_0^{p_s} (\nabla \cdot v_2) \, dp = -\frac{1}{g} \frac{\partial}{\partial t} p_s - E - P. \tag{2.5}$$

The vertically integrated mass flux divergence (precisely: vertically integrated divergence of horizontal mass transport) equals the sum of vertically integrated mass ($=\frac{p_s}{g}$) tendency and the freshwater flux. Other fluxes of trace constituents (e.g., carbon fluxes) can be neglected in this context.

Obtaining the four terms of equation (2.5) from ERA-Interim is not straight-forward because the four fields are not available consistently either as instantaneous or accumulated fields. Instead, $\langle \nabla \cdot v_2 \rangle$ is available as six-hourly analyzed instantaneous fields (valid for analysis time ± 3 hours) and $\frac{1}{g} \frac{\partial}{\partial t} p_s$ is consistently available as three-hourly analyzed fields, but E and P are only available as six-hourly forecasts but not as analyzed fields. Thus, it would be inconsistent to check the closure of equation (2.5) in ERA-Interim with the available mix of analyzed and forecast field. However, it is possible to estimate the freshwater flux indirectly from vertically integrated six-hourly moisture tendencies (unfortunately, no three-hourly moisture tendencies
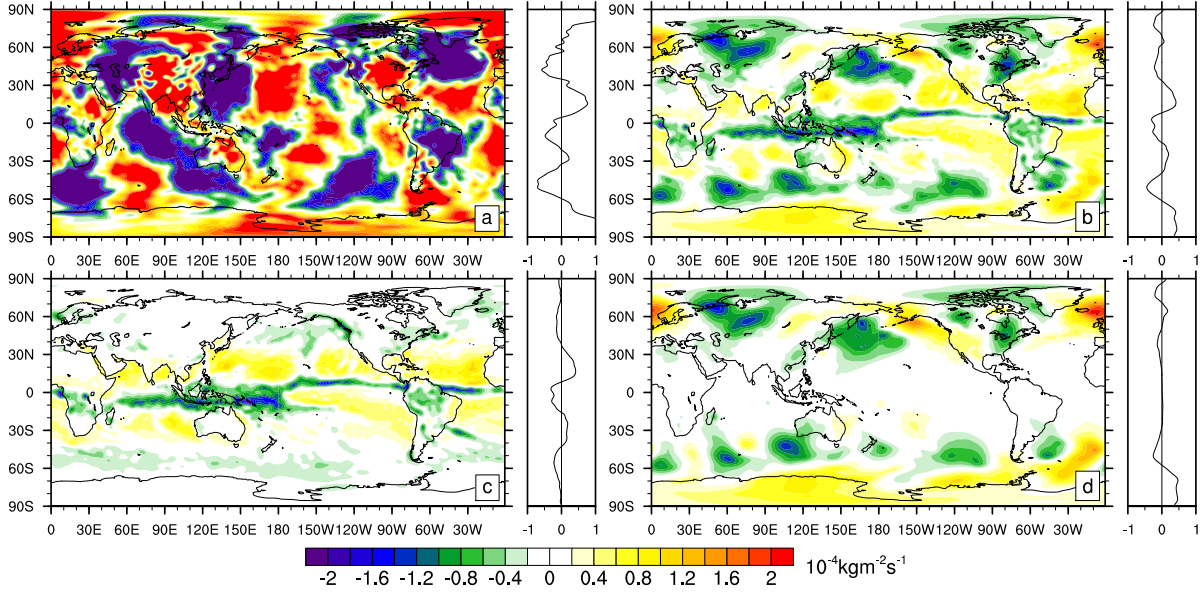
Figure 2: Vertical integral of monthly mean horizontal mass flux divergence for January 1990 (a) from six-hourly wind analyses (b) estimated indirectly from the contributions of (c) freshwater flux and (d) analyzed mass tendencies from ERA-Interim.

are available from ERA-Interim) and the divergence of vertically integrated six-hourly analyzed moisture transport [following Fasullo and Trenberth 2008a, see also equation (2.4)]. This is still not perfectly consistent, as accumulated fields of $\langle \nabla \cdot v_2 \rangle$ and $\langle \nabla \cdot (v_2 q) \rangle$ would actually be required, but these are not stored at ECMWF.

Fields representing the left and right-hand side of equation (2.5) are plotted in Fig. 2a and b, respectively. Fig. 2a shows vertically integrated mass flux divergence from six-hourly analyzed ERA-Interim fields. The field shown in Fig. 2b represents the sum of local mass tendencies and freshwater flux (estimated indirectly as described above). Fig. 2b shows realistic features, e.g., a strong signature of the Hadley circulation in the tropics (divergence in the subtropics, convergence co-located with the Inter-Tropical Convergence Zone) and convergence and divergence patterns associated with mid-latitude weather systems. In contrast, Fig. 2a, representing the instantaneous divergence of vertically integrated horizontal mass transport in ERA-Interim, looks quite noisy and lacks these structures and hence obviously does not represent the observed divergent atmospheric circulation very well. Additionally, Figs. 2c and d show the respective contributions from freshwater flux (dominating in the tropics) and surface pressure tendencies (dominating in the extratropics).

Decomposition of $\langle \nabla \cdot F_A \rangle$ reveals that the mass budget is relevant for the evaluation of this field because $\langle \nabla \cdot v_2 \rangle$ is implicitly included in this term:
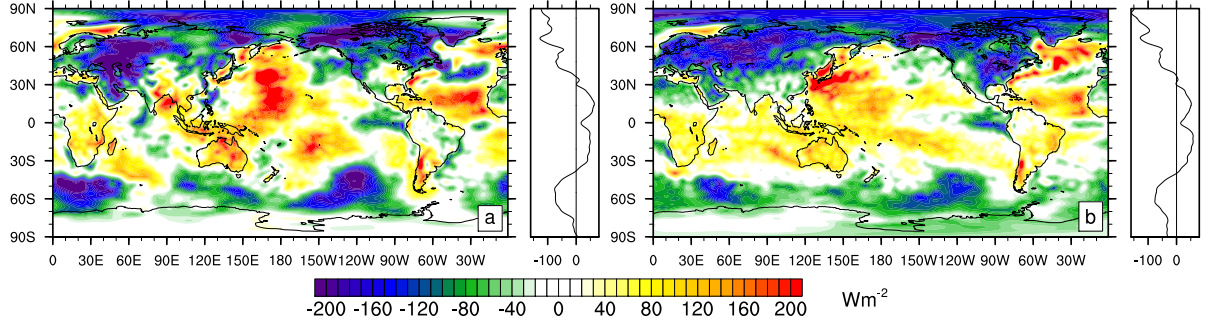
Figure 3: Direct estimate of monthly mean divergence of vertically integrated total energy transport for January 1990 from six-hourly analyzed (a) unadjusted and (b) mass-adjusted fields from ERA-Interim.

$$\langle \nabla \cdot F_A \rangle = \langle \nabla \cdot [(h+k)v_2] \rangle = \langle v_2 \cdot \nabla (h+k) \rangle + \langle (h+k)(\nabla \cdot v_2) \rangle \approx \langle v_2 \cdot \nabla (h+k) \rangle + (\hat{h} + \hat{k}) \langle \nabla \cdot v_2 \rangle. \tag{2.6}$$

Here, h denotes moist static energy and the caret denotes the vertical averaging operator (using vertically averaged h and k introduces only small errors because moist static energy varies only weakly with altitude). Hence, when computing $\langle \nabla \cdot F_A \rangle$ with the direct method, the erroneous structures of the mass flux divergence will affect the results. To reduce resulting errors in computed energy transports, we introduce a correction term, which estimates the error in the instantaneous mass divergence field from the difference of the right and left-hand side of equation (2.5). This difference is then multiplied by the local energy content of the atmospheric column, as suggested by the last term of equation (2.6), which yields the equation for the mass-adjusted (*adj*) directly (*dir*) estimated divergence of atmospheric energy transport, as presented in Mayer and Haimberger (2012):

$$\langle \nabla \cdot F_A \rangle_{dir}^{adj} = \langle \nabla \cdot F_A \rangle_{dir} - (\hat{h} + \hat{k})(\langle M_{DIV} \rangle + P + E + \frac{1}{g}\frac{\partial}{\partial t}p_s), \tag{2.7}$$

Note that here $\langle M_{DIV} \rangle$ means the vertically integrated instantaneous mass flux divergence with its erroneous patterns shown in Fig. 2a not to be confused with the "true" divergence field $\langle \nabla \cdot v_2 \rangle$ from equation (2.5). The other terms P, E, and $\frac{1}{g}\frac{\partial}{\partial t}p_s$ are obtained as described above. Note also the different sign of E in equation (2.7) compared to equation (3) in Mayer and Haimberger (2012), where E is defined positive upward. The result of this adjustment of the directly estimated $\langle \nabla \cdot F_A \rangle$ is presented in Fig. 3b. The unadjusted field (Fig. 3a) clearly shows patterns of the instantaneous mass divergence (Fig. 2a) which are removed in the adjusted estimate (Fig. 3b).

Systematically wrong surface pressure forecasts are another issue of the ERA-Interim mass budget. This can be seen from comparison of monthly averaged 12-hourly surface pressure
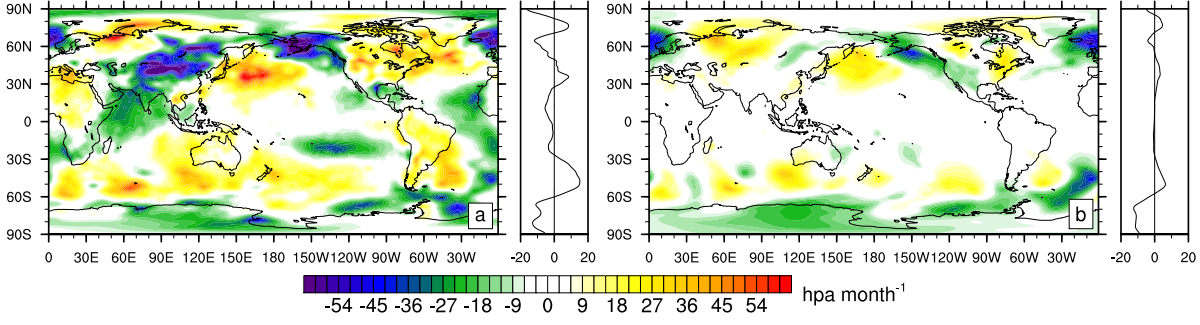
Figure 4: Monthly mean surface pressure tendencies for January 1990 (a) from twelve-hourly forecasts and (b) analysis from ERA-Interim.

tendency forecasts (i.e., the average of 62 forecasts in case of January) and the analyzed surface pressure tendency, shown in Fig. 4. Surface pressure forecasts are biased in the tropics as well as in the extratropics. This issue affects results from the indirect evaluation method, because budget closure requires the use of forecasts also for the energy tendency. We decompose the energy tendency term to explicitly show how the surface pressure tendency enters this term:

$$\frac{1}{g}\frac{\partial}{\partial t}\int\limits_{0}^{p_s(t)} e\,dp = \frac{1}{g}\int\limits_{0}^{p_s(t)}\frac{\partial e}{\partial t}\,dp + \frac{\overline{e(p_s)}}{g}\frac{\partial p_s}{\partial t}. \tag{2.8}$$

The overbar denotes a time average, in this case the 12-hour window covered by the forecast time. The error of the pressure forecast is determined straight-forward from the difference of forecasted (*fc*) and analyzed pressure tendencies (denoted by the delta operator). This yields the equation for the mass-adjusted forecasted energy tendency:

$$\frac{\partial\langle e\rangle}{\partial t}\Big._{fc}^{adj} = \frac{\partial\langle e\rangle}{\partial t}\Big._{fc} - \frac{\overline{\langle e(p)\rangle}_{fc}}{\overline{p}_s}\Delta(\frac{\partial p_s}{\partial t})_{fc}. \tag{2.9}$$

This equation is inserted into the right-hand side of equation (2.3) when computing $\langle\nabla\cdot F_A\rangle$ indirectly, as proposed by Mayer and Haimberger (2012). The mass-adjusted (*adj*) equation for the indirectly (*ind*) estimated divergence of total energy transport reads as follows:

$$\langle\nabla\cdot F_A\rangle_{ind}^{adj} = -\frac{\partial\langle e\rangle}{\partial t}\Big._{fc}^{adj} - F_S + Rad_{TOA}. \tag{2.10}$$

A comparison of unadjusted and mass-adjusted indirect estimate is presented in Fig. 5. The impact of the mass-adjustment on the indirect estimate is smaller than on the direct estimate (Fig. 3). However, visible differences exist, e.g., in the Kuroshio region or central Russia.

We also note that the mass-adjustment not only impacts climatological mean fields, but the adjustment terms exhibit also considerable temporal variability, i.e., the adjustment is also relevant for investigation of energy budget variability (see Fig. 4.41 in Mayer 2010).
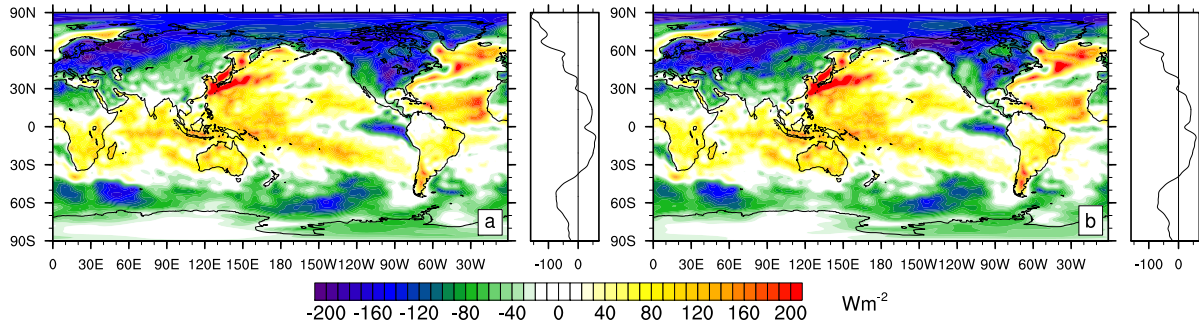
Figure 5: Indirect estimate of monthly mean divergence of vertically integrated total energy transport for January 1990 with (a) unadjusted and (b) mass-adjusted energy tendency from ERA-Interim.

2.3 The vertically integrated energy budget of the ocean

The divergence of vertically integrated heat (precisely: enthalpy) transport out of an oceanic column [DIVFO, left term of equation (2.11)] is balanced by the local tendency of ocean heat content [OHCT, first term on the right-hand side of equation (2.11)] and net surface flux F_S and can be written as:

$$\int\limits_{ssh}^{bottom} \nabla \cdot [c_{water}(T,S)\rho(T,S)\theta(z)v_2(z)]dz = -\frac{\partial}{\partial t} \int\limits_{ssh}^{bottom} c_{water}(T,S)\rho(T,S)\theta(z)dz + F_S.$$

(2.11)

Here, c_{water} is the heat capacity of sea water (depending on T and salinity S), ρ is sea water density (depending only on T and S when sea water is assumed incompressible), v_2 is the horizontal ocean velocity vector, and θ is sea water potential temperature. Integration boundaries are sea surface height (ssh) above a reference sea level and the ocean bottom. Note that, in contrast to the budget equation of the atmosphere [equation (2.1)], we consider only thermal energy in the ocean. Other forms of energy and especially their variability are negligible in this context. Moreover, there are no fluxes across the lower boundary, as equation (2.11) is ideally integrated to the bottom of the ocean. Before describing the explicit computation of DIVFO, computation of OHC is considered more closely in the following section.

2.4 Ocean heat content

As variations in heat capacity are small, c_{water} can be set constant. Density variations in association with temperature and salinity variations are larger, but also neglected by many authors. Additionally, most studies neglect ssh variations and set the upper integration boundary zero. However, regional ssh is known to vary considerably on interannual timescales, e.g., in association with ENSO, which raises the question, if this is due to steric effects (volume variations due

to thermal expansion) or due to mass flux divergence, i.e., changes in bottom pressure. If ssh variations were entirely due to steric effects, neglection of both ssh and using constant density would be a consistent approach because the mass of the column could be considered constant. On the other hand, if vertically integrated mass divergence dominated ssh variations, inclusion of ssh would be required to account for the mass variations.

To investigate this question we compute two quantities: First, we integrate $\rho(T, S)$ from z=0 to the bottom, which yields ocean mass using fixed integration boundaries. Variations of this quantity represent mass variations associated with steric effects (when neglecting compression). Second, we integrate $\rho(T, S)$ from z=ssh to z=0. The sum of these two quantities yields the full ocean mass (including the effects of both mass flux divergence and steric effects). Hence, if variations of the sum are small compared to the mass variations associated with steric effects, neglection of ssh and setting density constant is a valid approximation. As we are mainly interested in OHCT, the time derivative of OHC, we will consider time derivatives of mass in the following. We first consider the eastern equatorial Pacific, a region with strong ENSO signature. Fig. 6a clearly shows that mass hardly varies compared to rates of mass change associated with steric effects. Hence, despite extensive redistribution of warm water volume (water above the thermocline) within the Pacific basin in association with ENSO, bottom pressure does not change. Large changes of thermocline depth reflect the compensating processes, i.e., divergence, below the thermocline. Fig. 6b shows the same curves, but for the tropical Pacific. Here the picture is less clear. There appear to be steric effects in association with ENSO, e.g., in 1997/98, but total mass changes seem to be on the same order. However, it is hard distinguish steric changes from mass changes and Balmaseda et al. (2012) found that ECMWF's Ocean Reanalysis System 4 (ORAS4, Balmaseda et al. 2012) overestimates trends in ocean bottom pressure when compared to data from Gravity Recovery And Climate Experiment (GRACE). Given these results, we find it a reasonable approximation to choose constant density and therefore neglect ssh variations for all considered regions.

The equation of OHC consequently simplifies to

$$OHC = c_{water}\rho_0 \int\limits_0^{bottom} \theta(z)dz, \qquad (2.12)$$

with $c_{water} = 3990 Jkg^{-1}K^{-1}$ and $\rho_0 = 1026 kgm^{-3}$. As usually no snap shots of ocean temperature are available, the monthly tendency of ocean heat content (OHCT) is computed from centered differences of monthly mean OHC fields.

Tests showed that anomaly signals in ocean temperature decrease with depth. Additionally, noise in the ocean datasets increases disproportionately compared to the signal below depths of 300m (Mayer et al., 2014). At the same time the agreement between different ocean datasets decreases with depth, which is a result of decreasing number of observations with increasing
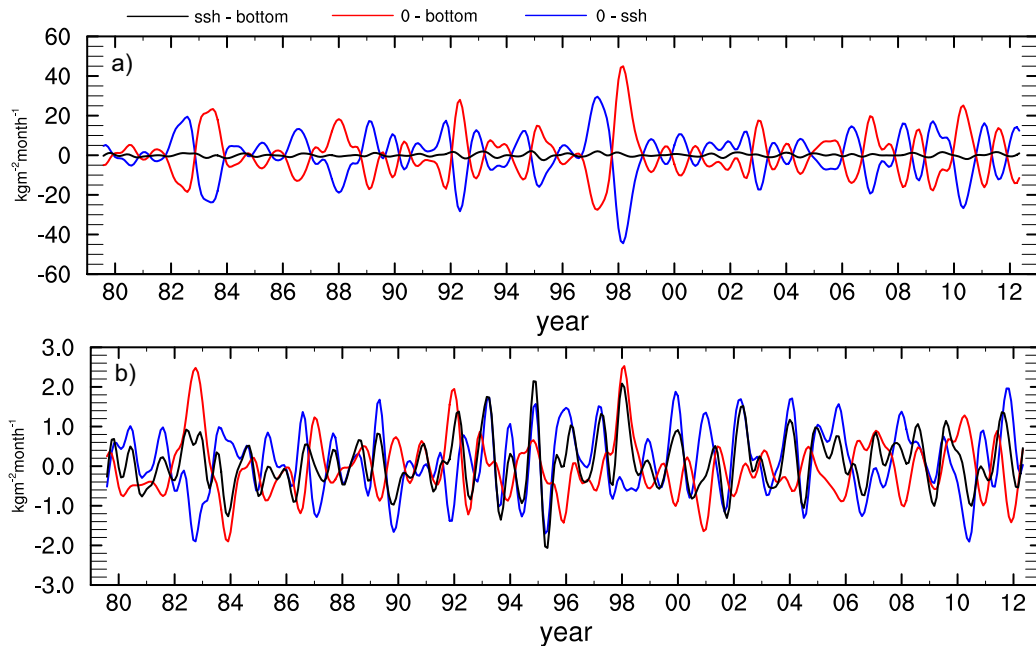
Figure 6: Ocean mass integrated from ssh to the ocean bottom (black curve), representing the sum of integration from a fixed zero level to the ocean bottom (red curve) and integration from ssh to the zero level (blue curve) averaged over (a) the eastern equatorial Pacific (5S-5N, 155W-70W) and (b) over the full tropical Pacific (30S-30N, 90E-70W).

depth. Hence, the choice of the upper integration bound for OHC and its tendency is a compromise between physical consistency (integration to the bottom would be perfectly consistent) and data quality. After testing several values for the upper integration bound, we chose a depth of 300m (see also Mayer et al. 2014) instead of integration to the bottom. This choice has implication for the indirect evaluation of DIVFO as will be discussed in the next section.

2.5   Divergence of ocean heat transport

Using the vertical integration operator $\langle\rangle$, which for the ocean, in contrast to the atmosphere, is defined in z-coordinates [see equation (2.12)], the divergence of ocean heat transport (F_O) can be written more shortly:

$$\langle\nabla \cdot F_O\rangle = -OHCT + F_S, \tag{2.13}$$

see also Fig. 1 for illustration. Similarly to the evaluation of $\langle\nabla \cdot F_A\rangle$, DIVFO can be computed either directly, i.e., by evaluation of the left-hand side of equation (2.13), or indirectly, i.e., by evaluation of the right-hand side of equation (2.13).

Computing $\langle\nabla \cdot F_O\rangle$ requires (besides θ) ocean velocity. This field is not available from ocean datasets based on in-situ data only such as Hadley EN3 (Ingleby and Huddleston 2007), which is employed (besides other datasets) in Mayer et al. (2014). Ocean reanalyses involving
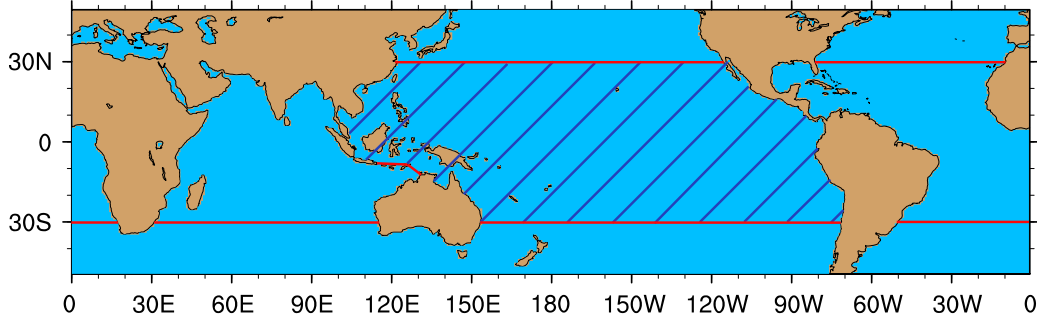
15

Figure 7: Cross sections (red lines) bounding the three tropical (30N-30S) ocean basins considered in Mayer et al. (2014).

an ocean model for assimilation such as ORAS4 provide at least monthly mean ocean velocity fields.

Tests showed that computation of fields of DIVFO from ORAS4 ocean temperature and velocity fields yields quite noisy results, probably due to the coarse time resolution. The focus of Mayer et al. (2014) is on ocean heat transports out of the tropical ocean basins rather than fields of DIVFO. For example, the ocean heat export from the tropical Pacific equals DIVFO area-integrated over the tropical Pacific region (hatched area in Fig. 7). Thus, this ocean heat export can be estimated alternatively from the sum of zonally integrated $\langle F_O \rangle$ across the boundaries of the tropical Pacific, i.e., the sum of $\langle F_O \rangle$ across the Pacific cross-sections at 30N and 30S and the ocean heat transport through the Indonesian Throughflow (ITF, see Fig. 7 for illustration). This approach yields much better results compared to area-integration of directly estimated DIVFO and is therefore employed in Mayer et al. (2014).

Computing DIVFO indirectly from OHCT and F_S is more problematic than indirect evaluation of $\langle \nabla \cdot F_A \rangle$ (described in section 2.1).

First, F_S needs to be specified. ERA-Interim surface flux forecasts are known to be biased (Berrisford et al., 2011). This is less problematic for indirect evaluation of $\langle \nabla \cdot F_A \rangle$ because forecasted atmospheric energy tendencies at least partly compensate these biases (Mayer and Haimberger, 2012). This is not the case for the ocean. It is also possible to estimate F_S indirectly from Rad_{TOA}, directly estimated $\langle \nabla \cdot F_A \rangle$ and analyzed atmospheric energy tendency (see, e.g., Trenberth and Fasullo 2008). This approach accumulates uncertainties from all atmospheric fields, but tests have shown that this estimate is more homogeneous in time than model forecasts of F_S and also the global mean is closer to zero.

Second, OHCT is required to be integrated over the full ocean depth in order to be consistent. Employing OHCT integrated only over the upper 300m of the ocean, as suggested in section 2.4 to reduce noise in the results, introduces another term to the equation for DIVFO, namely the energy flux across the depth of 300m (F_{300}). Equation (2.13) consequently changes to

$$\langle \nabla \cdot F_O \rangle_{300} = -OHCT_{300} + F_S - F_{300}. \tag{2.14}$$

Equation (2.14) is an equation for DIVFO in the upper 300m of the ocean rather than the full depth ocean. The energy flux across a depth of 300m is not available from any of the employed ocean datasets. In any case, F_{300} is very hard to quantify precisely. Assuming the mean and especially the variability of F_{300} to be small, it can be set zero. Then the indirect estimate of DIVFO includes accumulated uncertainties from OHCT and all atmospheric fields (when F_S is computed indirectly), plus, implicitly, the deviations of F_{300} from zero.

If multiple atmospheric and oceanic datasets are available, different indirect estimates of DIVFO can be obtained from all possible combinations of these datasets. Large differences among the different DIVFO estimates imply that uncertainties in the indirect estimate of DIVFO are too large to detect any true anomaly signals on a basin-integrated scale (see Fig. S2a in Mayer et al. 2014). Integrating OHCT to greater depths, which would certainly be desirable in terms of physical consistency, yields even greater uncertainties (see Fig. S2b in Mayer et al. 2014).

Hence, area-integrated DIVFO is computed directly from full-depth transports from ORAS4 zonally integrated across the cross-sections bounding the respective basin because uncertainties from the indirect estimate are too large.

3 Evaluation of poleward atmospheric energy transports from ECMWF reanalysis data

This study presents results of the evaluation of poleward atmospheric energy transports as evaluated mainly from ERA-I. The article describes the mean and interannual variability of zonally integrated transports and also some aspects of physical consistency of ERA-I, covering the period available at that time (1989-2010).

My contributions to this work were interpretation of the results (equal share with Leo Haimberger, who also suggested the basic layout of this study) and accomplishment of all computations. In the course of this work I also improved the method for the mass-adjustment compared to the method implemented earlier at the department (freshwater flux had not been included in the estimation of the erroneous mass divergence before). Moreover, I prepared all visualizations required for this publication and wrote the paper.

Mayer, M., and Haimberger, L., 2012: *Poleward atmospheric energy transports and their variability as evaluated from ECMWF reanalysis data.* Journal of Climate, 25, 734–752.

◉Poleward Atmospheric Energy Transports and Their Variability as Evaluated from ECMWF Reanalysis Data

MICHAEL MAYER AND LEOPOLD HAIMBERGER

Department of Meteorology and Geophysics, University of Vienna, Vienna, Austria

ABSTRACT

The vertically integrated global energy budget is evaluated with a direct and an indirect method (both corrected for mass inconsistencies of the forecast model), mainly using the European Centre for Medium-Range Weather Forecasts (ECMWF) Re-Analysis Interim (ERA-Interim) data. A new estimate for the net poleward total energy transport is given. Comparison to satellite-derived radiation data proves that ERA-Interim is better suited for investigation of interannual variations of the global energy budget than available satellite data since these either cover a relatively short period of time or are too inhomogeneous in time. While much improved compared to the 40-yr ECMWF Re-Analysis (ERA-40), regionally averaged energy budgets of ERA-Interim show that strong anomalies of forecasted vertical fluxes tend to be partly compensated by unrealistically large forecasted energy storage rates. Discrepancies between observed and forecasted monthly mean tendencies can be taken as rough measure for the uncertainties involved in the ERA-Interim energy budget. El Niño–Southern Oscillation (ENSO) is shown to have large impact on regional energy budgets, but strong compensation occurs between the western and eastern Pacific, leading to only small net variations of the total poleward energy transports (similar magnitude as the uncertainty of the computations). However, Hovmöller longitude–time plots of tropical energy exports show relatively strong slowly eastward-moving poleward transport anomalies in connection with ENSO. Verification of these findings using independent estimates still needs to be done.

1. Introduction

Horizontal energy transports within the atmosphere and ocean have to balance the differential radiative heating by the sun. Especially from the late 1970s onward, when global satellite measurements became available, numerous scientific papers estimated the total poleward energy transport and its partition between the atmospheric and oceanic domain using different datasets (e.g., Carissimo et al. 1985; Zhang and Rossow 1997; Fasullo and Trenberth 2008b, hereafter FT08b) but the bandwidth of the different estimates is considerable. Stone (2008) states that there is no definite estimate of this fundamental quantity to test climate model output with as uncertainties in the datasets still are too large. Additionally, results strongly depend on

the evaluation method. FT08b constructed uncertainty estimates of the poleward energy transports by comparing results from different combinations of input datasets.

An even more demanding problem is the investigation of interannual variations of the energy budgets as it requires both high accuracy and temporal homogeneity of all used datasets. Certainly, satellite datasets provide the most accurate values [e.g., for radiation at the top of the atmosphere (TOA)], but available datasets are either relatively short or not sufficiently homogeneous in time as will be shown in this work. In terms of temporal homogeneity, the most recent reanalyses seem preferable, although the observational system is permanently changing and so are its error characteristics (Haimberger 2006). At least reanalyses use a state-of-the-art data assimilation system that is not changed during the complete data period and, in the case of ERA-Interim, adaptive bias correction algorithms effectively take care of changing biases in assimilated satellite radiances (Dee and Uppala 2009). Another issue, already described in Trenberth (1991), is the mass budget in analysis and also reanalysis products. The time-averaged divergent mass transports (leading to local surface pressure tendencies)

Corresponding author address: Michael Mayer, Department of Meteorology and Geophysics, University of Vienna, UZA II, Althanstr. 14, 1090 Vienna, Austria.
E-mail: mima@univie.ac.at

do not vanish locally, which consequently affects the energy budget. Probably because of these difficulties, studies concerning the variability of the energy budgets are relatively rare (e.g., Zhang et al. 2007; Trenberth et al. 2002b).

Zhang et al. (2007), using the International Satellite Cloud Climatology Project Flux product (ISCCP-FD) for radiation at the TOA, investigated variations of poleward energy transports of the combined atmosphere–ocean system but did not find the available surface flux datasets sufficiently reliable to estimate the atmospheric transport variability separately. Trenberth et al. (2002b) used various satellite and reanalysis datasets, mainly to study the correlation of tropical atmospheric energy budgets with El Niño–Southern Oscillation (ENSO) and found a strong correlation between the divergence of horizontal atmospheric energy transport and ENSO indices.

This work mainly employs the European Centre for Medium-Range Weather Forecasts (ECMWF) Re-Analysis Interim (ERA-Interim) data. We give new estimates of average poleward energy transports within the atmosphere, evaluated with two different approaches. Physical consistency and accuracy of the datasets is assessed by checking the degree of fulfillment of global constraints of the energy budget and comparison with satellite-derived radiative data. Whereas Chiodo and Haimberger (2010) mainly investigated the variability and trends of surface fluxes and precipitation in ERA-Interim, this work concentrates on the interannual variability of the energy budget, especially energy exports from the tropics, and tries to separate true climate signals from spurious shifts introduced by changes of the observation system. Correlation between ENSO and the total energy export, as well as correlation between ENSO and the moist static energy export from the tropics to higher latitudes is investigated in some detail. Additionally, longitude-dependent anomalies of energy exports are considered, which reveal some interesting new structures.

All used datasets are described in section 2 and methods are described in section 3. Results are presented in section 4. Summary and conclusions are given in section 5.

2. Data

The 40-yr ECMWF Re-Analysis (ERA-40) was the second major reanalysis of the ECMWF and covers a period of 45 years from September 1957 to August 2002 (Uppala et al. 2005). The assimilating model operated with a horizontal resolution of T159 ($\Delta x \simeq 125$ km) on 60 vertical levels (Simmons and Burridge 1981) with a hybrid vertical coordinate reaching up to 0.1 hPa and used an improved 6-hourly three-dimensional variational data assimilation (3D-Var) analysis cycle. ERA-40 has been used as benchmark in many budget calculations up to

date (e.g., Trenberth and Fasullo 2010). Nevertheless, according to Uppala et al. (2005), horizontally spreading positive moisture increments in ERA-40 systematically led to far too high precipitation rates over tropical oceans and consequently unrealistically strong latent heat release in these regions. This problem also affects the accuracy of calculated moisture budgets as the excessive precipitation is balanced by unrealistically negative average total column water vapor tendencies in the tropics.

ERA-Interim was released in 2007 and has been constantly updated since then. For this study data have been available for the period 1989–2009. This reanalysis has a horizontal resolution at T255 ($\Delta x \simeq 80$ km) on 60 vertical hybrid model levels. Important improvements compared to ERA-40 are a 12-h four-dimensional variational data assimilation (4D-Var) and the increased horizontal resolution (Dee et al. 2011, and references therein). Biases of satellite measurements are treated by the variational bias correction (VarBC; Dee and Uppala 2009), and homogenized radiosonde temperature data (Haimberger 2007) have been used. The problems with tropical precipitation in ERA-40 were largely solved by a new humidity analysis, improved model physics, direct assimilation of the Special Sensor Microwave Imager (SSM/I), and partly High Resolution Infrared Radiation Sounder (HIRS) radiances, VarBC, and 4D-Var (Dee et al. 2011). There is still slightly more precipitation than evaporation in the global mean, but the hydrological cycle is much better balanced than in ERA-40. Both ERA-40 and ERA-Interim analysis fields are available at 6-hourly resolution. This study uses ERA-Interim as main dataset because of its superiority in terms of physical consistency. ERA-40 is used for reasons of intercomparison only.

ISCCP-FD is a dataset including radiative fluxes at TOA and the surface from radiative transfer model calculations (initialized with satellite data), available from 1983 to 2007 (see Zhang et al. 2004 for details). We use monthly means on a regular $2.5° \times 2.5°$ latitude–longitude grid in order to compare ISCCP-FD and ERA-Interim in terms of absolute differences and homogeneity in time.

TOA flux data from the satellite-based Clouds and the Earth's Radiant Energy System (CERES) have been used as reference too. We use the CERES energy balanced and filled (EBAF) version, ranging from March 2000 to February 2010, on a $1.0° \times 1.0°$ latitude–longitude grid (see Loeb et al. 2009 for details). This dataset is tuned to the currently best estimate of the global mean imbalance at TOA (+0.85 W m^{-2}; Hansen et al. 2005).

3. Methods

The basis for climate budget diagnostics is the vertically integrated budget equation for the total energy content of an atmospheric column:

$$\frac{1}{g}\frac{\partial}{\partial t}\int_{0}^{p_s}(c_p T + \Phi_s + Lq + k)\,dp$$
$$+ \frac{1}{g}\int_{0}^{p_s}[\mathbf{V}\cdot(c_p T + \Phi + Lq + k)\mathbf{v}_2]\,dp$$
$$+ F_S - \mathrm{Rad}_{\mathrm{TOA}} = 0, \qquad (1)$$

where g denotes the gravitational acceleration; p is pressure (the subscript s means surface); c_p is the specific heat at constant pressure; T is temperature; Φ is geopotential; L is the phase transition energy for evaporation; q is specific humidity; k is specific kinetic energy; $\mathbf{v}_2$ is the horizontal wind; F_S is the net energy balance at the surface (positive downward), consisting of latent heat flux LH, sensible heat flux SH, and net radiation Rad_S; and $\mathrm{Rad}_{\mathrm{TOA}}$ is the net radiative balance at TOA (positive downward). Note that the first term on the lhs is the vertically integrated total energy tendency, whereas the second term denotes the vertically integrated divergence of moist static plus kinetic energy. We can rewrite Eq. (1) in a shorter form:

$$\langle \mathbf{V}\cdot\mathbf{F}_A \rangle = -\frac{\partial\langle e\rangle}{\partial t} - F_S + \mathrm{Rad}_{\mathrm{TOA}}, \qquad (2)$$

where $\mathbf{F}_A$ denotes the atmospheric flux of total energy and e the total specific atmospheric energy and we have introduced the vertical integration operator $\langle\cdot\rangle$. Considering the zonal average of the total atmospheric energy transport, consisting of one purely divergent and one purely rotational part, the rotational part vanishes. Thus, net meridional energy transports can be obtained from the vertically integrated divergence of horizontal energy transport [second term in Eq. (1)] alone. In the following, we describe two different methods to calculate $\langle \mathbf{V}\cdot\mathbf{F}_A \rangle$.

a. Direct method

The direct method calculates $\langle \mathbf{V}\cdot\mathbf{F}_A \rangle$ from the fields of u, v, q, and T provided by the reanalysis dataset with 6-hourly resolution. Haimberger et al. (2001) showed that budget calculations using fields with a 6-hourly time resolution can lead to substantial systematic errors in the order of up to 20%. This problem arises because instantaneous fields are extrapolated to 6 h. Trenberth (1991) found that mass consistency is a crucial criterion for obtaining meaningful results. Chiodo and Haimberger (2010) showed that problems with mass consistency still exist in state-of-the-art reanalysis products such as ERA-Interim. They proposed a correction method dealing with spurious divergent mass fluxes, which we use in this work in a slightly modified way and get the following expression for the corrected (superscript c) directly estimated (subscript dir) divergence of energy transport:

$$\langle \mathbf{V}\cdot\mathbf{F}_A \rangle^c_{\mathrm{dir}} = \langle \mathbf{V}\cdot\mathbf{F}_A \rangle_{\mathrm{dir}} - (\hat{h} + \hat{k})(\langle M_{\mathrm{DIV}}\rangle$$
$$+ P - E + M_{\mathrm{TEND}}), \qquad (3)$$

which consists of the vertically integrated divergence of energy transport computed directly from analyzed fields (first term on the rhs) and the mass flux correction term (second term on the rhs). The first part of the correction term consists of $\hat{h}$ and $\hat{k}$, the vertically averaged moist static and kinetic energy, respectively. We know from the vertically integrated continuity equation for moist air that precipitation, evaporation, and the local mass tendency have to be balanced by the horizontal divergence of mass flux. To which degree this requirement is satisfied is estimated in the second part of the correction term. It compares the instantaneous vertically integrated divergence of mass flux from the model, $\langle M_{\mathrm{DIV}}\rangle$ (stored at ECMWF), which is implicitly used for computing $\langle \mathbf{V}\cdot\mathbf{F}_A \rangle_{\mathrm{dir}}$, with the sum of precipitation P minus evaporation E [following Fasullo and Trenberth (2008a), $P - E$ is indirectly estimated from the divergence of horizontal moisture transport and analyzed moisture tendency] and the analyzed mass tendency, M_{TEND}, which is calculated with finite differences from the analyzed pressure field 6 h ahead and 6 h before analysis time. Thus, the mass flux correction term represents the spurious divergence of energy transport resulting from imbalances of the mass budget and is subtracted from $\langle \mathbf{V}\cdot\mathbf{F}_A \rangle_{\mathrm{dir}}$.

b. Indirect method

The indirect method calculates $\langle \mathbf{V}\cdot\mathbf{F}_A \rangle$ as a residual of the rhs in Eq. (2). The fluxes F_S and $\mathrm{Rad}_{\mathrm{TOA}}$ are taken from 12-hourly forecasts of the ERA-Interim model. Since F_S and $\mathrm{Rad}_{\mathrm{TOA}}$ are accumulated quantities and the tendency term can be calculated exactly with finite differences, the temporal resolution is much better than for the direct method. Vertical integrals of the tendency term are calculated with model level data with full vertical resolution. Note that we calculate the energy tendency from model forecasts to be consistent with the forecast fluxes. In this respect our method is different from Porter et al. (2010) who use analyzed energy tendencies.

However, mass consistency is a remaining problem arising in the energy tendency term. Again, we follow Chiodo and Haimberger (2010) for the correction of the forecasted (subscript fc) energy tendency:

$$\frac{\partial\langle e\rangle^c}{\partial t_{\mathrm{fc}}} = \frac{\partial\langle e\rangle}{\partial t_{\mathrm{fc}}} - \frac{\overline{\langle e(p)\rangle}_{\mathrm{fc}}}{\overline{p}_s}\Delta\left(\frac{\partial p_s}{\partial t_{\mathrm{fc}}}\right). \qquad (4)$$

The correction term in Eq. (4) (second term on the rhs) consists of the time-averaged (average of forecast for $t = +12$ h and analysis at t = 0 h) vertical integral of the total

energy, $\overline{\langle e(p)\rangle}_{fc}$, and the time-averaged surface pressure $\overline{p}_s$. The surface pressure forecast error $\Delta(\partial p_s/\partial t)_{fc}$ is computed as the difference of forecasted and analyzed surface pressure tendency over 12 h. Thus, the corrected indirectly estimated (subscript ind) divergence of horizontal energy transport reads as follows:

$$\langle \mathbf{\nabla} \cdot \mathbf{F}_A \rangle^c_{\text{ind}} = -\frac{\partial \langle e \rangle^c}{\partial t_{\text{fc}}} - F_S + \text{Rad}_{\text{TOA}}. \qquad (5)$$

Analogously, the divergence of horizontal moisture transport can be obtained by computing either the lhs (direct method) or rhs (indirect method) of the vertically integrated moisture budget equation:

$$\langle \mathbf{\nabla} \cdot q\mathbf{v}_2 \rangle = P - E - \frac{\partial w}{\partial t}, \qquad (6)$$

where $\langle \mathbf{\nabla} \cdot q\mathbf{v}_2 \rangle$ denotes the divergence of horizontal moisture transport and $\partial w/\partial t$ is the tendency of total column water vapor. The correction for both methods is of the same structure as for $\langle \mathbf{\nabla} \cdot \mathbf{F}_A \rangle$.

As soon as $\langle \mathbf{\nabla} \cdot \mathbf{F}_A \rangle$ and $\langle \mathbf{\nabla} \cdot q\mathbf{v}_2 \rangle$ are available (computed either from the direct or the indirect method), one can calculate the divergent flux fields through inversion of the Laplacian and subsequent derivation of the potential field. We use the spectral method for this purpose, since the fields from ECMWF are available already at full resolution (T255, N128 Gaussian grid) and since the computations in spectral space are exact.

4. Results

a. Annual mean results

The methods described in the previous section yield four estimates of the horizontal energy transport and its divergence (direct and indirect estimate, with and without mass flux correction, respectively). First, when determining the "best" estimate, meaning most consistent in a physical sense, we show the superiority of the mass flux–corrected energy transports. Mass is constant in both hemispheres and considering the maximum content of total atmospheric energy to be found near the equator (only valid for the annual mean), it follows that the net meridional energy transport (shown in Fig. 1) should be small at the equator (in the zonal average). Approximating the vertically integrated divergence of mass flux with the surface pressure tendency forecasts and integrating over one hemisphere, we get a cross-equatorial mass flux of nearly -81 kg m^{-1} s^{-1} (southward) for the ERA-Interim period, which is clearly unrealistic. Using analyzed pressure tendencies reduces this mass flux to nearly zero (<0.1 kg m^{-1} s^{-1}). The mass flux correction reduces the indirect estimate of energy transport from -1.6 to -0.8 PW and the direct estimate
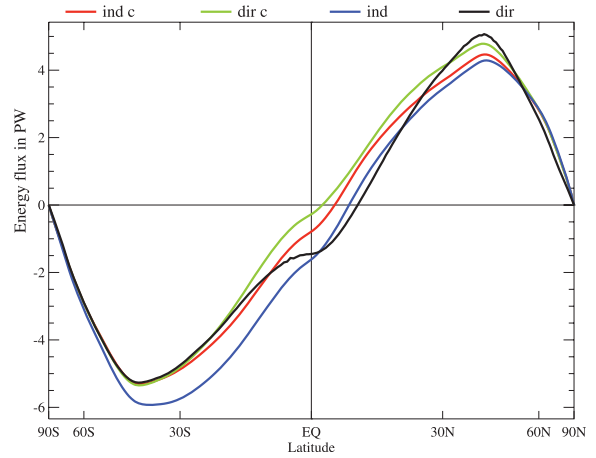

FIG. 1. Zonally integrated meridional profiles of northward total energy transport from ERA-Interim (1989–2009), inferred with corrected (ind c) indirect (ind) and corrected (dir c) direct (dir) methods.

from -1.5 to -0.3 PW at the equator. The directly estimated cross-equatorial energy fluxes (CEF; not given in FT08b) appear to be more realistic since they are closer to zero. The temporal variance of the CEF is halved by the mass flux correction in both the direct and indirect estimate.

Our mass-corrected results for meridional peak energy transports from ERA-Interim and ERA-40 are compared to the estimates from FT08b, who used CERES for TOA radiation in combination with different reanalyses and ocean datasets in Table 1 (note that 2σ uncertainty means two standard deviations of the yearly average peak energy transports in our case, whereas FT08b obtained the standard deviations from different combinations of different input datasets).

Direct estimates from ERA-Interim and ERA-40 are quite similar and show good agreement with each other. In contrast, indirectly estimated peak transports from ERA-40 exceed those from ERA-Interim by 0.4 PW in both hemispheres because the strong negative moisture tendencies in the tropics seen from ERA-40 affect the indirectly estimated $\langle \mathbf{\nabla} \cdot \mathbf{F}_A \rangle$ in the tropics [see Eq. (2)].

TABLE 1. Comparison of different atmospheric peak transport estimates (PW) in the Northern (NH) and Southern (SH) Hemisphere as well as cross-equatorial energy fluxes (CEF) (PW) with 2σ uncertainty from ERA-Interim (1989–2009), ERA-40 (1989–2000), and FT08b.

	SH	NH	CEF
EI ind c	-5.3 ± 0.2	4.5 ± 0.1	-0.8 ± 0.2
EI dir c	-5.4 ± 0.2	4.8 ± 0.1	-0.3 ± 0.2
E40 ind c	-5.7 ± 0.3	4.9 ± 0.3	-0.9 ± 0.2
E40 dir c	-5.2 ± 0.3	4.9 ± 0.2	-0.2 ± 0.2
FT08b	-4.9 ± 0.2	5.1 ± 0.5	—

It is interesting to see that both directly and indirectly estimated peak transports tend to be larger than those from FT08b in the Southern Hemisphere and smaller than those from FT08b in the Northern Hemisphere. Only the confidence intervals of the indirect estimate from ERA-Interim data and the direct estimate from ERA-40 data overlap with the uncertainty bounds of FT08b.

Comparison of the fields of $\langle \mathbf{\nabla} \cdot \mathbf{F}_A \rangle^c_{\mathrm{ind}}$ and $\langle \mathbf{\nabla} \cdot \mathbf{F}_A \rangle^c_{\mathrm{dir}}$ (Fig. 2) shows the noisiness of the direct estimate. The RMS value of this estimate is 21% higher and the extreme values are about 4 times larger than those seen from the indirect estimate. Maximum noise can be found over high topography, mainly due to numerical artifacts stemming from the spectral representation of the horizontal fields and the time extrapolation of instantaneous fields. Note that no spatial filtering has been applied to any divergence estimate. Filtering helps but errors also project to longer wavelengths and these are not removed. However, divergent transports, shown as $10° \times 10°$ averages in Fig. 2, are quite similar, which implies that the noise from the direct estimate does not affect the spatially averaged transports too much. The strongest large-scale differences between the estimates are stronger northward energy export from the Indo-Pacific warm pool and stronger convergence of energy transport over the northern continents in the direct estimate.

To get an impression of the model dependence of the different methods, we computed the RMS averages of the ERA-Interim minus ERA-40 monthly mean $\langle \mathbf{\nabla} \cdot \mathbf{F}_A \rangle$ estimates from the different methods for the overlapping period 1989–2000 (Fig. 3). The result is quite clear. The direct estimate shows large zonal mean RMS differences with a global average value at 235.4 W m^{-2}, which is reduced to 56.8 W m^{-2} by the mass flux correction. In contrast, the indirect estimate exhibits relatively small RMS differences with only 27.5 W m^{-2} on global average (mass corrected). The spatial distribution (not shown) shows the largest RMS differences (extreme values higher than 1000 W m^{-2}) of the direct estimate over high topography, which can already be expected when considering the bottom panel in Fig. 2. These extreme values may stem from the different model topographies of the two reanalyses leading to numerical artifacts (local extreme values) located at not the exact same positions. However, even over the oceans where these effects do not exist, the RMS differences nowhere drop below 40 W m^{-2}. The corrected indirect estimate shows low RMS values everywhere, showing little differences between land and sea. Only the deep tropics show relatively large zonal averages up to 42.3 W m^{-2} stemming from the problems with the moisture budget in ERA-40 (strong negative moisture tendencies also affect the indirectly estimated $\langle \mathbf{\nabla} \cdot \mathbf{F}_A \rangle$). From this point of view, the direct method appears to be more model

dependent than the indirect method and seems to be not very reliable when considering relatively small regions.

b. Physical consistency of ERA-Interim

According to Hansen et al. (2005), the net imbalance at TOA mainly leads to a warming of the oceans. Thus, the atmospheric energy tendency should be positive, but close to zero globally and locally in the long-term mean. Consequently, Eq. (2) reduces to

$$\langle \mathbf{\nabla} \cdot \mathbf{F}_A \rangle = \mathrm{Rad}_{\mathrm{TOA}} - F_S. \tag{7}$$

The same is valid for the local and global moisture tendency. Over land, F_S exhibits a rather small yearly cycle and therefore has to vanish locally on longer time scales. Over the oceanic domain its mean should be consistent with the global mean radiative forcing (on the order of 1 W m^{-2}). Hence, computing $\mathrm{Rad}_{\mathrm{TOA}} - \langle \mathbf{\nabla} \cdot \mathbf{F}_A \rangle$ and averaging either globally or over a single domain gives the (erroneous) mean surface flux. For the indirect estimate $\langle \mathbf{\nabla} \cdot \mathbf{F}_A \rangle^c_{\mathrm{ind}}$, this equation in fact computes the balance between energy tendency and surface fluxes [cf. Eq. (2)] and gives -0.3 W m^{-2} for the global domain, whereas inserting $\langle \mathbf{\nabla} \cdot \mathbf{F}_A \rangle^c_{\mathrm{dir}}$ yields -1.0 W m^{-2}. As ERA-Interim (correctly) computes nearly vanishing surface fluxes over land (-0.1 W m^{-2}) but globally fairly uniform negative energy tendency forecasts (-7.0 W m^{-2} globally, -7.3 W m^{-2} over land), the requirement is well satisfied only on the global domain by the indirect estimate, whereas $\langle \mathbf{\nabla} \cdot \mathbf{F}_A \rangle^c_{\mathrm{dir}}$ performs better on the single domains.

The representation of the hydrological cycle in ERA-Interim shows strong improvements in respect to ERA-40. The global long-term mean of 12-hourly moisture tendency forecasts in ERA-40 is -14.5 kg m^{-2} month^{-1} (-14.0 W m^{-2}), with the lowest values in the tropics. In ERA-Interim, these deficient negative tendencies are reduced to nearly zero (-0.1 W m^{-2}). Thus, the excessive tropical precipitation in ERA-40 mentioned in section 2 has successfully been reduced by the improvements in the data assimilation system. However, the mean moisture forecast of ERA-Interim is quite noisy and regionally (e.g., eastern equatorial Pacific) relatively strong tendencies remain.

For a more comprehensive review of atmospheric conservation properties in ERA-Interim see Berrisford et al. (2011).

c. Comparison with satellite data

Net radiation at TOA is biased in ERA-Interim as it produces a mean net energy loss of 1.2 W m^{-2} on average (1989–2009). Trenberth and Fasullo (2010) found the bias of TOA radiation in reanalyses (such as ERA-40) as well as the models from the Third Coupled Model
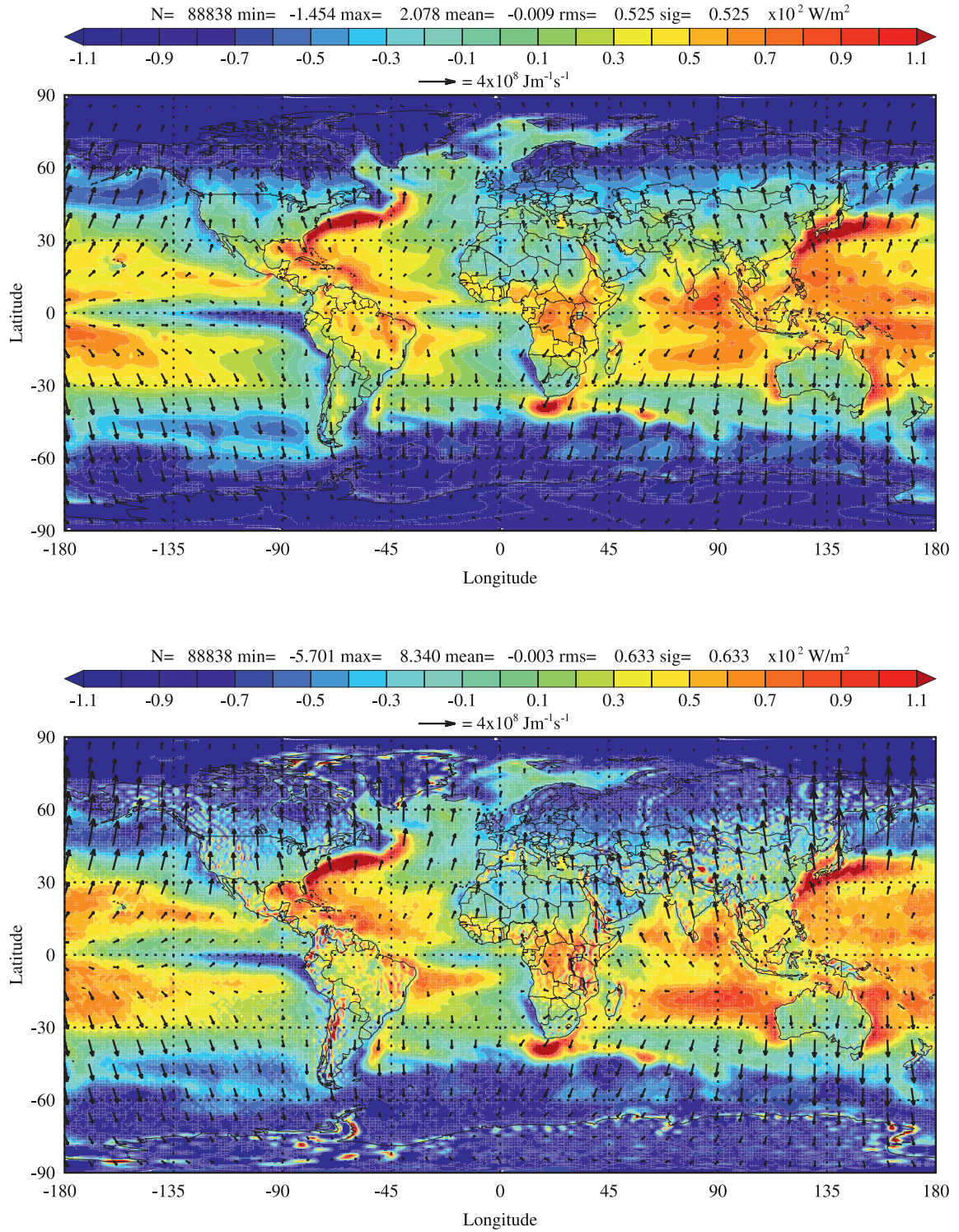
FIG. 2. Energy transport and its divergence from (top) corrected indirect (ind c) and (bottom) direct (dir c) method (ERA-Interim climatology 1989–2009). Note higher noise level of direct method near high topography and 21% higher standard deviation.
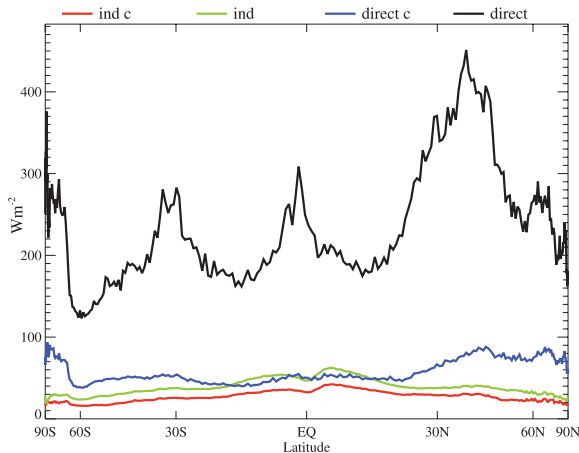
JOURNAL OF CLIMATE

FIG. 3. Differences between ERA-Interim and ERA-40 estimates of the divergence of total energy transport. Fields first were RMS-averaged in time (1989–2000) and then zonally averaged.

Intercomparison Project (CMIP3; see Meehl et al. 2007 for details) to be not uniformly distributed, with generally negative biases in the tropics and positive biases in the extratropics (with an additional yearly cycle). ERA-Interim exhibits similar deficiencies when comparing net TOA radiation with CERES and ISCCP-FD data for the overlapping 2001–07 period (top two panels in Fig. 4). The largest negative deviations can be found over equatorial landmasses, whereas tropical oceans show uniform, but weaker, negative differences. Positive differences are found over warm (e.g., Gulf Stream) *and* cool (e.g., Humboldt stream) ocean currents, the Sahara and the extratropics. The bottom panel in Fig. 4 shows ISCCP-FD (cf. CERES) having a mainly negative bias over land and a positive bias over oceans, but in general the biases are smaller than in ERA-Interim. This picture also reveals a noticeable quasi-rectangular area of positive differences between about 60°S and 60°N eastward of about 45°W, which could be an artifact of CERES or ISCCP-FD. RMS differences between ERA-Interim and the satellite data are about 11 W m^{-2}, whereas ISCCP-FD and CERES differ by only 6 W m^{-2}.

Converting the Rad_{TOA} difference between ERA-Interim and CERES to a difference in total poleward energy transport (atmosphere + ocean), we find ERA-Interim producing too weak peak poleward energy fluxes by 0.7 PW (5.8 PW vs 5.1 PW) in the Northern and 0.4 PW (−5.8 PW versus −5.4 PW) in the Southern Hemisphere. The largest difference in total poleward energy transport can be found around 18°N (CERES 4.8 PW, ERA-Interim 3.9 PW). The peaks of poleward total energy transports (atmosphere + ocean) from the ERA-40 climatology (1989–2000) at Rad_{TOA} are too weak by

0.8 PW (5.8 PW vs 5.0 PW) on the Northern and 0.5 PW (−5.8 PW vs −5.3 PW) in the Southern Hemisphere. The maximum difference can be found around 15°N (CERES 4.5 PW, ERA-40 3.2 PW). So we find the radiation at TOA improved when comparing ERA-Interim to ERA-40 but it still exhibits deficiencies.

As ISCCP-FD overlaps with nearly the complete ERA-Interim period, we can additionally compare the two datasets in terms of temporal homogeneity. The strong shift toward negative Rad_{TOA} anomalies in ISCCP-FD (Fig. 5, right panel) in late 2001 stems from changes in the observational analysis procedure altering outgoing longwave radiation (OLR; Zhang et al. 2006). The impact of the Mount Pinatubo eruption in June 1991 is likely to be overestimated in ISCCP-FD with the largest monthly anomalies reaching less than −8 W m^{-2} (averaged between 40°N and 40°S) right after the eruption, whereas Minnis et al. (1993) give only −4.3 W m^{-2} (ERBS data) for the same region. Direct comparison shows the much better homogeneity in time of ERA-Interim (Fig. 5, left panel), but there can also be found two (comparatively weak) shifts in 1992 because of the availability of new SSM/I clear-sky radiances from the Defense Meteorological Satellite Program (DMSP) F10 instrument (Chiodo and Haimberger 2010) and in 2003 due to the introduction of the Atmospheric Infrared Sounder (AIRS) on the Earth Observing Satellite (EOS) *Aqua* in 2003. The Mount Pinatubo signal is extremely weak in ERA-Interim, as the forecast model does not account for changes of aerosol concentrations in the lower stratosphere (Dee and Uppala 2009). Both datasets show signals from the different ENSO states in tropical Rad_{TOA} anomalies, but with differing amplitudes (e.g., early 1998).

Considering the Hovmöller plots for Rad_S in Fig. 6, the inhomogeneities of ISCCP-FD become even more obvious. The spurious shift in late 2001 is enhanced at the surface as between 1998 and 2001 strong positive anomalies can be found. As a result, ISCCP-FD shows global mean monthly vertical radiative flux divergence anomalies between more than +8 W m^{-2} (2000–01) and less than −8 W m^{-2} (1994), which is clearly unrealistic and 4 times larger than the extreme values found in ERA-Interim. The southward shift of the ITCZ during an El Niño event is also reflected in a surface radiation anomaly with a dipole structure, as can be seen from both panels in Fig. 6 in 1997/98. Both datasets show a dipole with similar strength, which demonstrates the much better signal-to-noise ratio of ERA-Interim. The signal from the weaker El Niño event in early 1992 can still be seen in ERA-Interim, but is covered in ISCCP-FD.

Hovmöller plots for Rad_{TOA} from ERA-Interim and CERES for the overlapping period show the good agreement between the two datasets (Fig. 7). Both datasets

Rad$_{TOA}$ EI minus CERES mean 2001-2007

N= 10368 min= -6.086 max=   5.143 mean=   -0.246 rms=   1.086 sig=   1.058   x10^1 W/m^2

Rad$_{TOA}$ EI minus ISCCP mean 2001-2007

N= 10368 min= -5.385 max=   5.581 mean=   -0.104 rms=   1.125 sig=   1.121   x10^1 W/m^2

Rad$_{TOA}$ CERES minus ISCCP mean 2001-2007

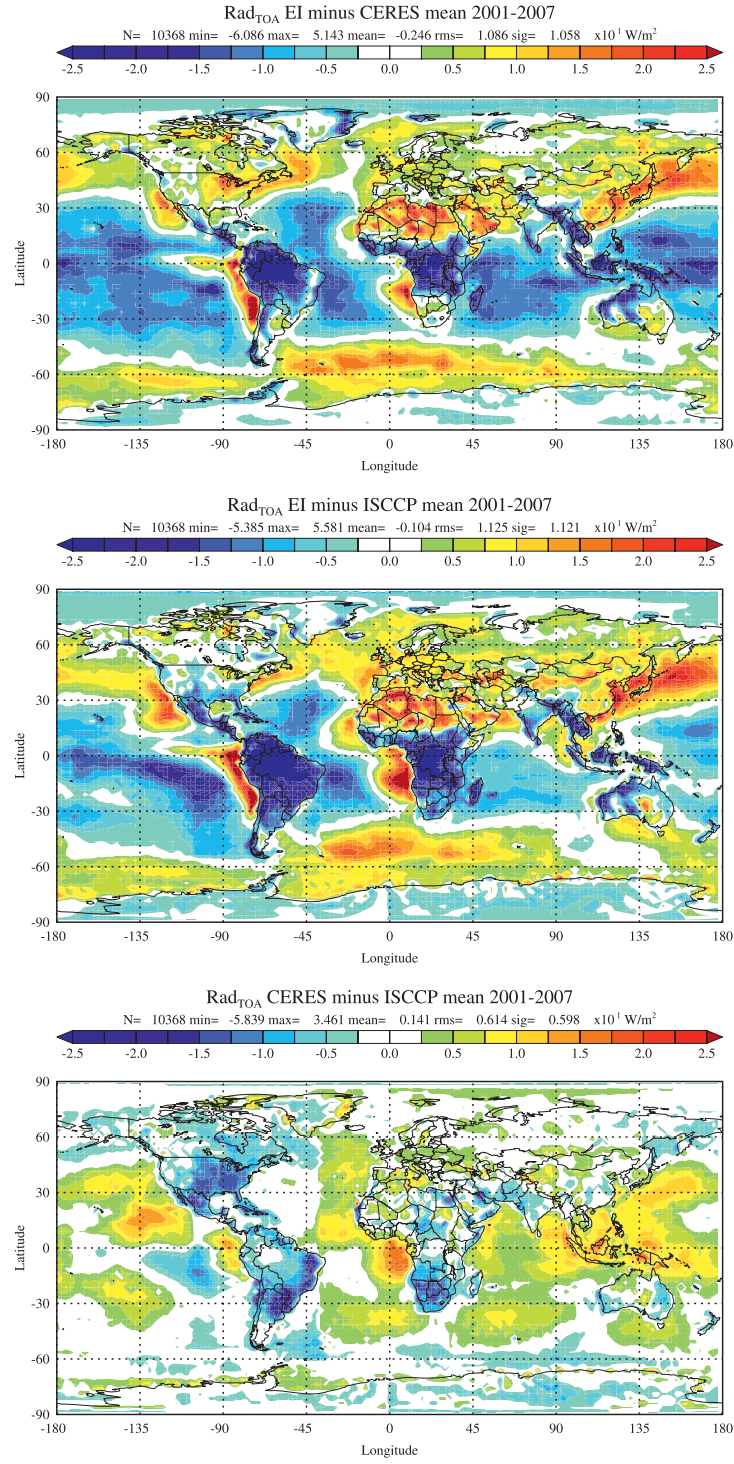N= 10368 min= -5.839 max=   3.461 mean=   0.141 rms=   0.614 sig=   0.598   x10^1 W/m^2

FIG. 4. Mean difference in Rad$_{TOA}$: (top) ERA-Interim minus CERES, (middle) ERA-Interim minus ISCCP-FD, and (bottom) CERES minus ISCCP-FD for the period 2001–07.
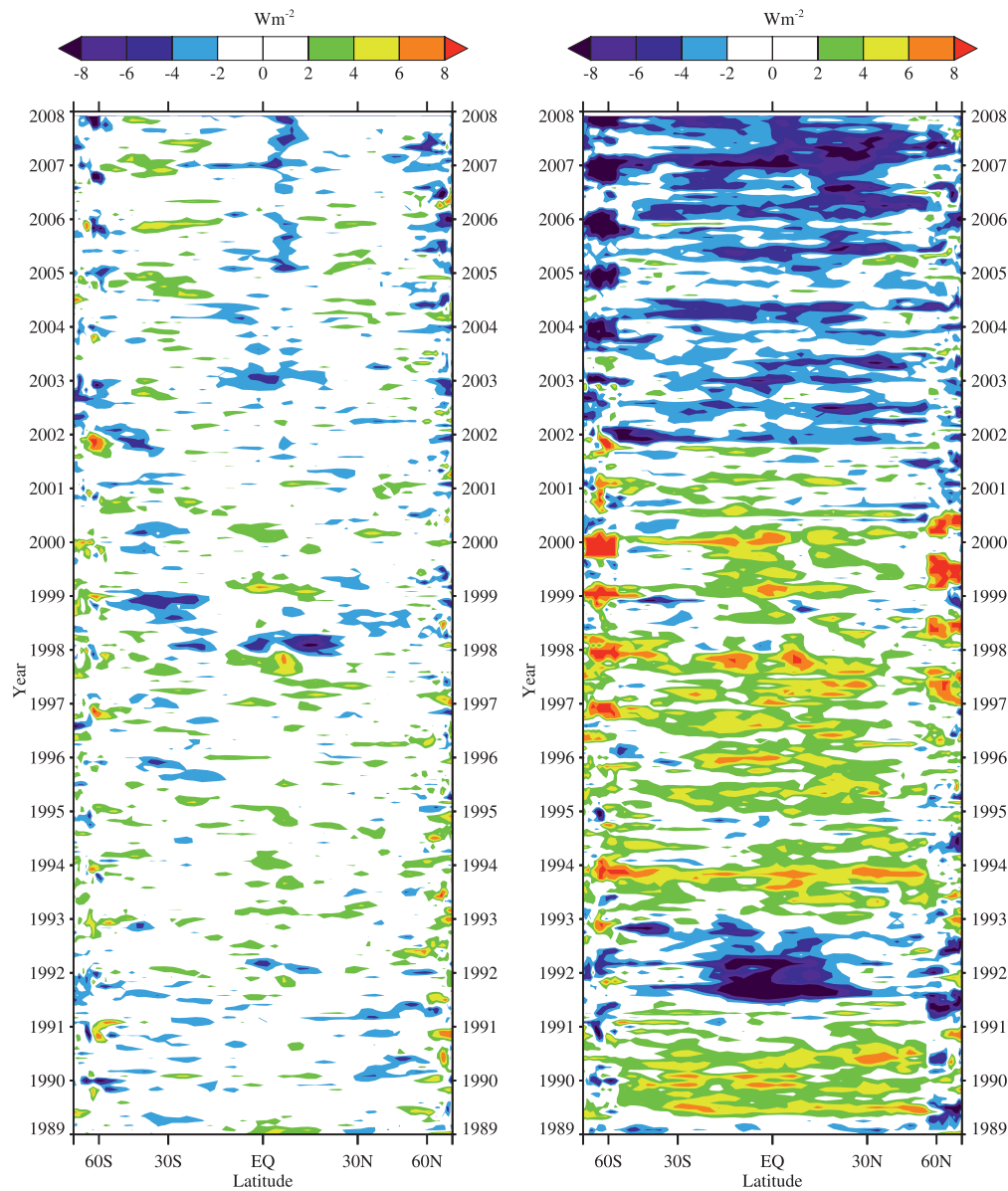
27

FIG. 5. Zonal mean monthly anomalies of Rad_{TOA} from (left) ERA-Interim and (right) ISCCP-FD 1989–2007.

show similar ENSO-related anomalies (e.g., in 2003 or 2006), and other large-scale anomalies like the negative anomalies in 2001–02 and early 2004 in the Southern Hemisphere. The positive anomalies following the strong 2007–08 La Niña event seem to be missing in ERA-Interim. In fact, ERA-Interim shows a positive anomaly of the same magnitude as CERES when using a shorter climatology of the late 2000s (not shown). Hence, this anomaly of Rad_{TOA} in 2007–08 exists in the ERA-Interim as well, but it is covered by another shift toward generally lower Rad_{TOA} values around 2006.

We conclude that ERA-Interim, despite its deficiencies in absolute net radiation at the TOA, appears to be much more suitable than ISCCP-FD for the investigation of interannual variations of the energy budgets. ERA-Interim and CERES show very good agreement on location, magnitude, and timing of anomalies, but CERES seems to be superior in terms of temporal homogeneity.

d. Interannual variations

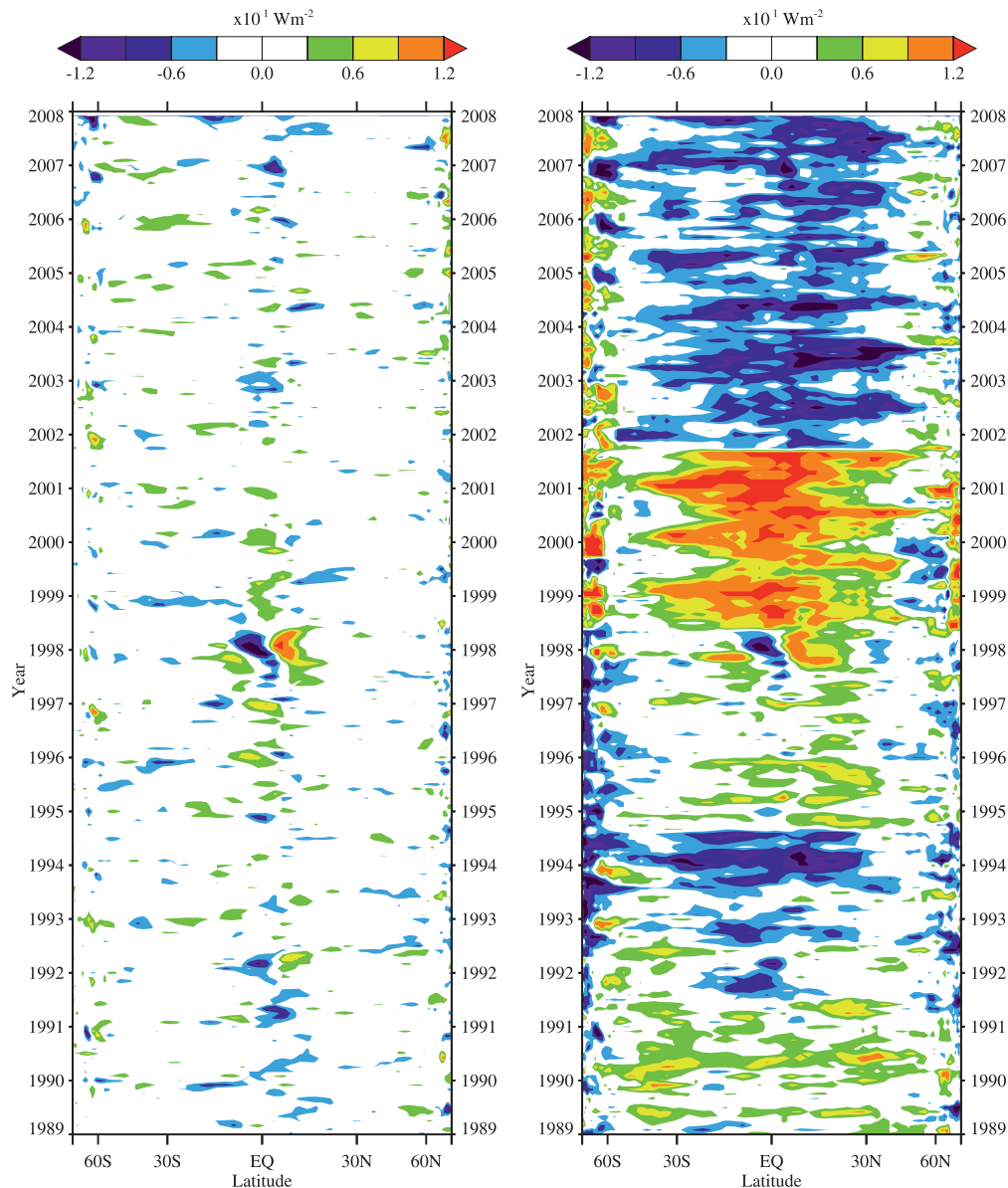Investigation of interannual variations of the global energy budget requires high physical consistency and

MAYER AND HAIMBERGER

FIG. 6. Zonal mean monthly anomalies of Rad_S from (left) ERA-Interim and (right) ISCCP-FD 1989–2007.

temporal homogeneity of the reanalysis product used. First of all, we have a look at the interannual variation of energy transports out of the tropics, bounded by 30°N and 30°S (Fig. 8). The corrected estimates show good agreement with each other, with a correlation coefficient of 0.85 for the running means and 0.99 when considering the monthly anomalies. The maximum anomalies are about ±0.3 PW, which is less than 4% of the 1989–2009 average exports. It is also worth mentioning that the adverse effect of erroneous divergent mass transports on the uncorrected estimates shows strong variations in time.

Differences between corrected and uncorrected energy export anomalies reach up to 0.8 PW, which corresponds to tropical mass export anomalies of up to 45 kg m^{-1} s^{-1}. Thus, mass flux correction not only improves the accuracy of the calculated fluxes, but also enhances temporal homogeneity. Hence, from now on, we exclusively consider mass-corrected results.

Two questions arise when considering Fig. 8. First, how much of the shown variability is real? To address this problem, we computed anomalies of analysis increments of the tendency of the vertically integrated total energy
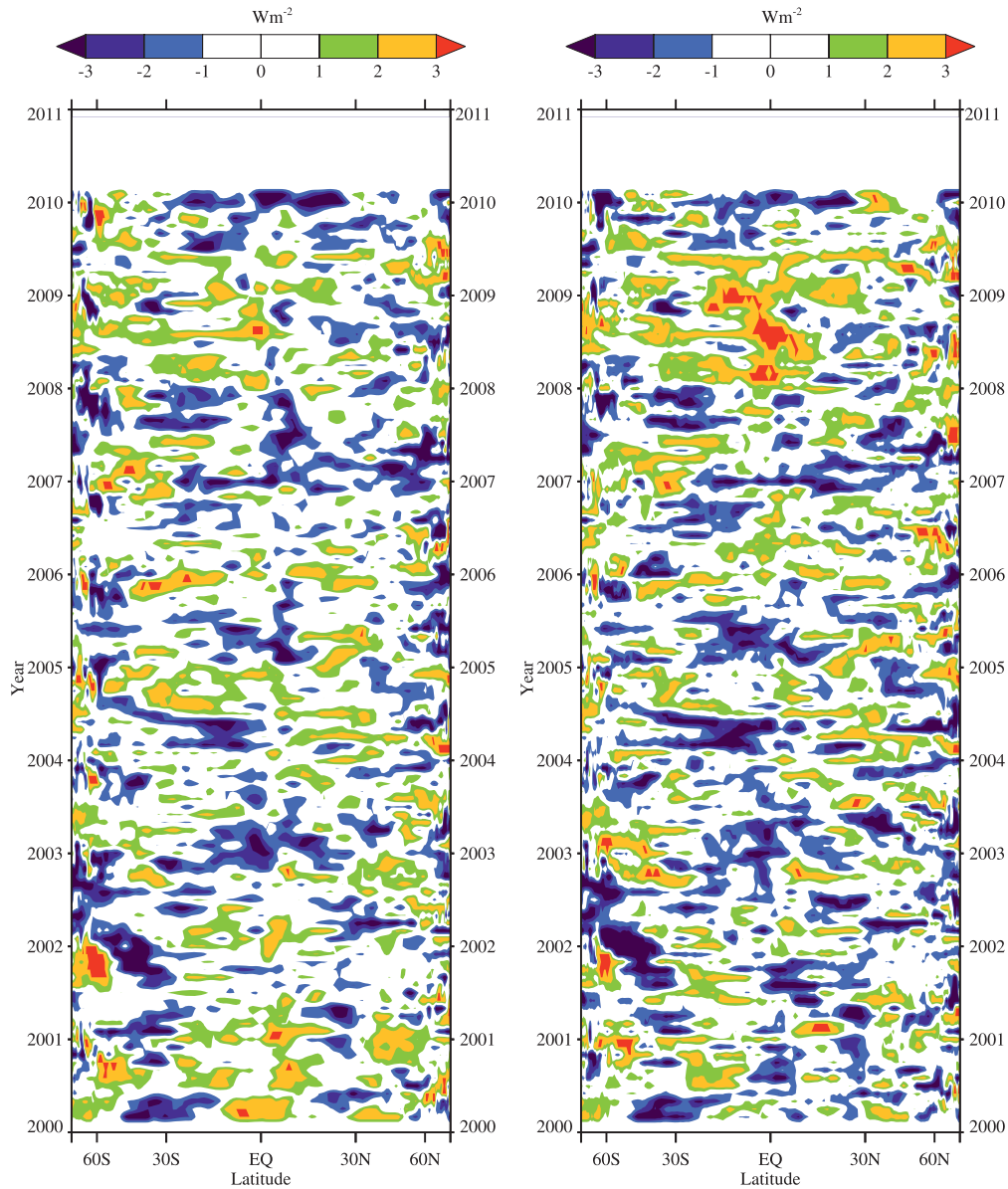
FIG. 7. Zonal mean monthly anomalies of Rad$_{TOA}$ from (left) ERA-Interim and (right) CERES 2000/03–2010/02.

content (defined as analyzed minus forecasted energy content, shown in Fig. 9). Analysis increments are a sensitive indicator for changes in the balance between the climate of the model and the analysis. A change of analysis increments may either stem from a change in the model physics (which can be excluded for ERA-Interim), a real change in the circulation, or a change in the observing system. The two shifts in 1992 and in 2003 (described in section 4c) can also be detected in the analysis increments. The effect of the 1992 shift from negative to rather neutral Rad$_{TOA}$ anomalies in the

extratropics (see Fig. 5, left panel) explains the (consequently spurious) drop of tropical energy exports shown in Fig. 8 quite well.

Two further shifts can be found in the analysis increments. They coincide with the introduction of the Advanced Microwave Sounding Unit-A (AMSU-A) on *NOAA-15* in 1998 and the increasing availability of GPS radio occultation data, especially after the launch of the Constellation Observing System for Meteorology, Ionosphere, and Climate (COSMIC) program in 2006 (see Poli et al. 2010). We conclude that the shift back to generally
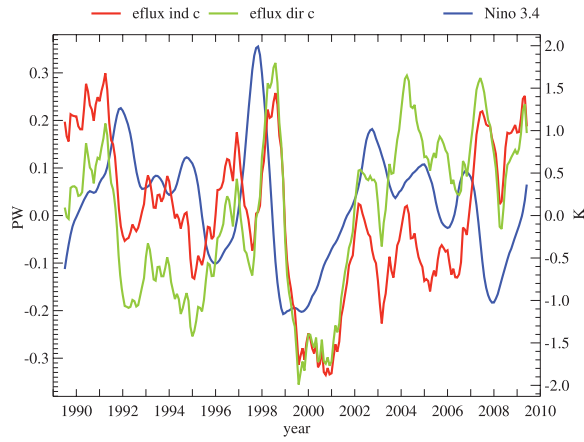
FIG. 8. The 12-months running mean of tropical energy export (30°N–30°S) anomalies (mass-corrected indirect and direct estimate from ERA-Interim) and 12-months running mean of Niño-3.4 (5°N–5°S, 170°–120°W) SST anomaly index.

stronger exports from 2006 onward is also artificial. The positive transport anomaly in 1998 followed by a negative anomaly around 2000 are likely real signals as the analysis increments seem to be quite constant during that time.

After assessment of the temporal homogeneity, we investigate our second question: how strong is the modulation of the energy export by ENSO? Therefore, we took a closer look at the correlation between the Niño-3.4 sea surface temperature (SST) anomaly index (5°N–5°S, 170°–120°W, shown in Fig. 8) and different area averages of the divergence of total and moist energy transport. The top panel in Fig. 10 shows lagged correlations between Niño-3.4 and $\langle \nabla \cdot \mathbf{F}_A \rangle$, averaged over the eastern Pacific (30°N–30°S, 170°–120°W) as well as over the tropics as a whole (30°N–30°S, 180°W–180°E). The eastern Pacific average of $\langle \nabla \cdot \mathbf{F}_A \rangle$ shows maximum correlation with Niño-3.4 (0.86 and 0.85 for indirect and direct estimate, respectively) at a 1-month lag. The correlation between total tropical energy export and Niño-3.4 is generally weaker and shows one peak at positive lags (maximum correlation for indirect estimate 0.29 at a 9-month lag and for direct estimate 0.28 at an 8-month lag) and one even weaker peak around a -12-month lag. The area of positive correlations is relatively broad, which reflects the impression from Fig. 8 that ENSO and total energy export show some common behavior, but the timing of the export anomalies is varying. It is likely that the aforementioned inhomogeneities in time damp this correlation. This is most obvious before 1992 where energy exports and Niño-3.4 appear to be anti-correlated.

The bottom panel of Fig. 10 shows the correlation between the divergence of moisture transport and Niño-3.4
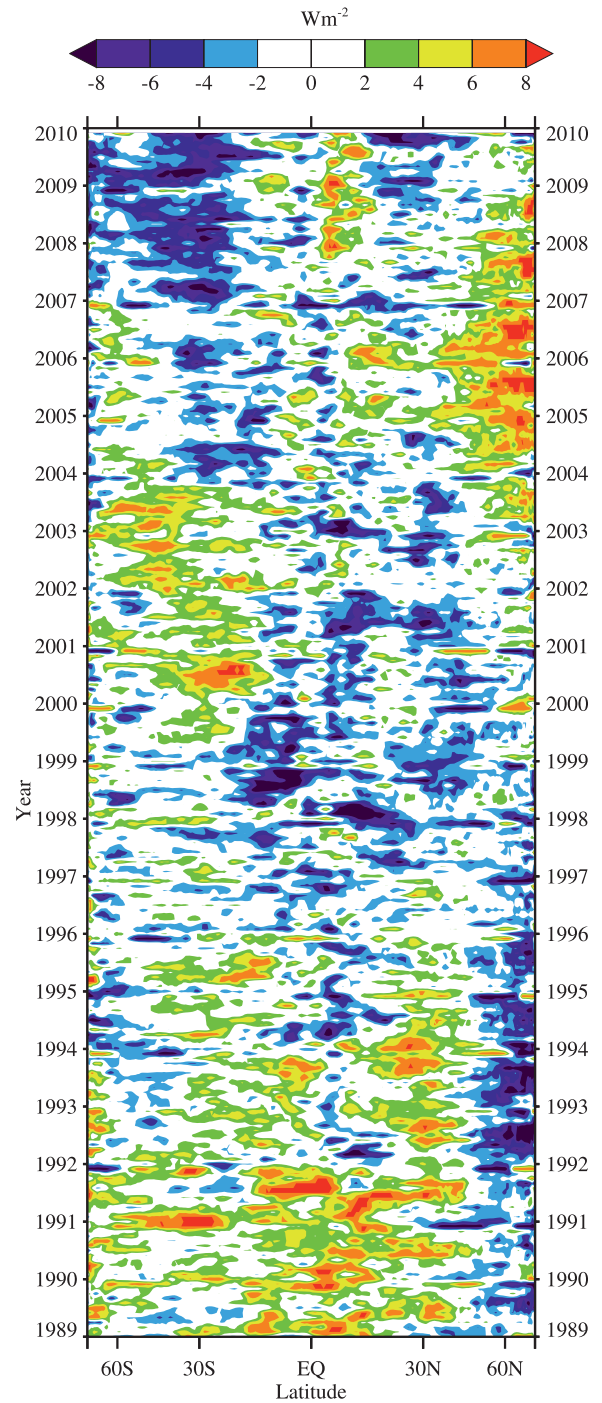

FIG. 9. Zonal mean analysis increments of total energy content forecasts ($\langle \partial e / \partial t \rangle_{\text{ana}} - \langle \partial e / \partial t \rangle^c_{\text{fc}}$) from ERA-Interim.
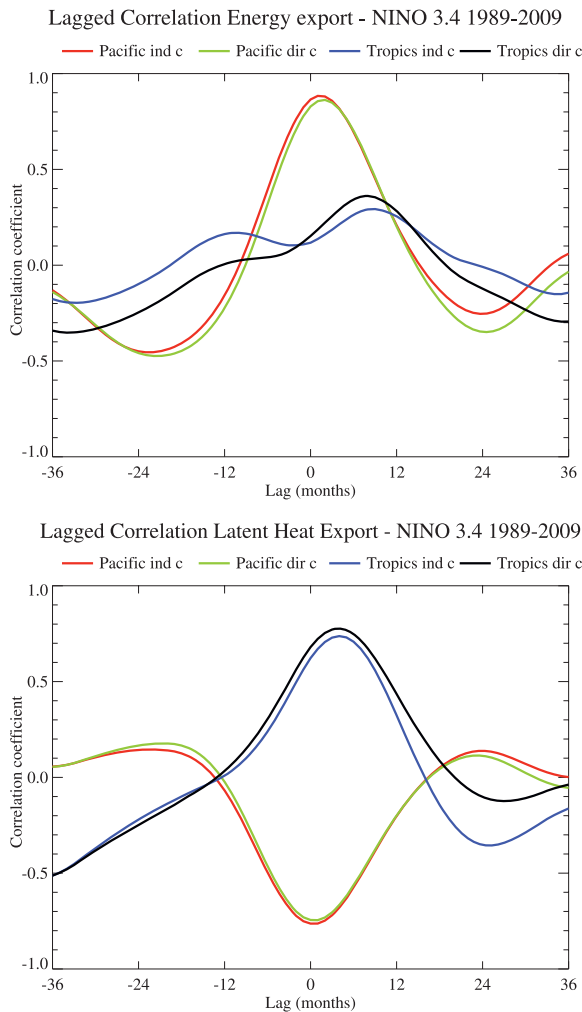
Lagged Correlation Energy export - NINO 3.4 1989-2009

Lagged Correlation Latent Heat Export - NINO 3.4 1989-2009

FIG. 10. (top) Lagged correlation between the eastern tropical Pacific average (30°N–30°S, 170°–120°W, red and green curve) as well as the total tropical average (30°N–30°S, 180°W–180°E, blue and black curve) of $\langle \mathbf{\nabla} \cdot \mathbf{F}_A \rangle$ with the Niño-3.4 index. (bottom) As in (top), but for the divergence of moisture transport.

for the same regions as in the top panel. There obviously exists a strong anticorrelation (-0.84 for the indirect and -0.82 for the direct estimate at a 1-month lag) between the divergence of moisture transport over the eastern Pacific and Niño-3.4. This is clear, as during an El Niño event anomalously strong convection occurs over this region, which is coupled with stronger-than-normal convergence of moisture transport.

In contrast to the zonal mean total energy export, the tropical moisture export (180°W–180°E) shows a relatively strong positive correlation with Niño-3.4 (0.74 for indirect and 0.78 for direct estimate at a 4-month lag).

When averaged over 30°N–30°S, the enhanced divergence of moisture transport over the western tropical Pacific during El Niño outweighs the weakening divergence of moisture transport over the eastern tropical Pacific, leading to positive anomalies of tropical moisture export in total (180°W–180°E).

Anomalies of $\langle \mathbf{\nabla} \cdot \mathbf{F}_A \rangle$ occurring during the 1997/98 El Niño impressively show the strong compensation between eastern and western Pacific anomalies. During the peak phase of the event (according to Niño-3.4 late 1997), as expected, strong positive divergence anomalies prevail over the eastern tropical Pacific (east of the date line), whereas the opposite occurs in the western tropical Pacific (west of the date line; Fig. 11). The divergent energy transports across 30°N and 30°S are 15%–20% stronger (weaker) than normal in the Western (Eastern) Hemisphere at this time. In sum, more energy than normal is exported from the tropical Pacific region (110°E–80°W, see also the top-right plot in Fig. 12), but the export anomaly for the entire tropics (180°W–180°E) at the peak of the 1997/98 El Niño is slightly negative (less than 2% below average). Thus, even very strong large-scale anomalies tend to be compensated for in the zonal mean leading to a very weakly varying total poleward energy transport. The largest peak for tropical energy exports is achieved during the phase shift of ENSO. Around October 1998, when Niño-3.4 is already indicating La Niña conditions, the energy export from the Indo-Pacific warm pool is anomalously strong, outweighing spreading negative anomalies over the eastern Pacific (not shown). Longer time series are needed to see if this behavior is typical for strong ENSO events.

It is difficult to estimate the accuracy of the peak magnitude of the transport anomalies. The left panel in the first row of Fig. 12 shows anomalies of the vertical flux divergence (defined as $F_S - \text{Rad}_{\text{TOA}}$) over the tropical Pacific and its decomposition into different components. Concentrating on the El Niño event in 1997/98 and the subsequent La Niña event, we find the turbulent surface fluxes being the main modulating factor of the vertical flux divergence anomalies. Rad_{TOA} and Rad_S show a response to the varying cloud conditions, but their contribution to the vertical flux divergence anomalies is relatively small. Deficiencies of ERA-Interim become evident when considering the panel to the right, which shows anomalies of forecasted energy tendencies, analyzed energy tendencies as well as $\langle \mathbf{\nabla} \cdot \mathbf{F}_A \rangle^c_{\text{ind}}$ and $\langle \mathbf{\nabla} \cdot \mathbf{F}_A \rangle^c_{\text{dir}}$ over the tropical Pacific. Apparently, analysis increments are not constant in time in that region. A large part of turbulent surface flux anomalies into the atmosphere (the ocean) is converted to positive (negative) forecasted energy tendencies (the correlation coefficient between LH + SH and forecasted energy tendencies is -0.76), which is not realistic as can
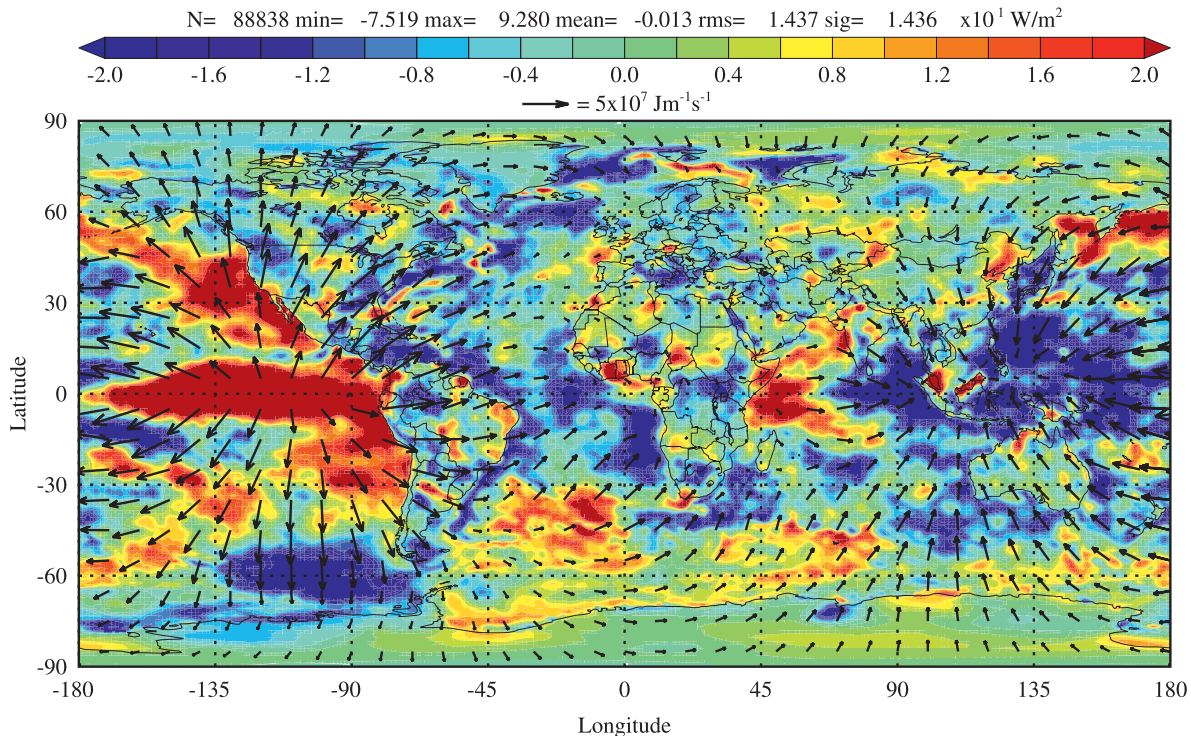
FIG. 11. Anomalous horizontal energy transport and its divergence (with respect to the 1989–2009 climatology), 12-months average, centered at November 1997.

be seen from regional storage analysis increments. These anomalies of analysis increments are regional and can hardly be seen on the zonal average (see also Fig. 9). Thus, vertical flux anomalies are compensated rather by the storage rate than by $\langle \mathbf{V} \cdot \mathbf{F}_A \rangle$. Chiodo and Haimberger (2010) have shown the magnitude of LH+SH anomalies to be in good quantitative agreement with the ECHAM5–Atmospheric Model Intercomparison Project (AMIP; prescribed SSTs) results. This agreement is not very compelling as both models may use similar bulk parameterizations for the surface fluxes. Thus, the reliability of ERA-Interim surface fluxes is still questionable. Comparison of Rad_{TOA} and Rad_S between ERA-Interim and ISCCP-FD (Figs. 5 and 6) shows radiation anomalies of similar magnitude during the 1997/98 El Niño. Altogether, the observed strong anomalies of the analysis increments indicate that the model does not react physically consistently to the SST forcing, but it is difficult to estimate the resulting impact on $\langle \mathbf{V} \cdot \mathbf{F}_A \rangle$. Considering anomalies of analysis increments as kind of error estimate, the noise (anomalies of analysis increments) is in the order of the signal (anomalies of $\langle \mathbf{V} \cdot \mathbf{F}_A \rangle$), even for the strong event in 1997/98.

The middle and the bottom row in Fig. 12 show analogous plots, but partitioned for western and eastern Pacific. The signal-to-noise-ratio appears much better for the separate regions, indicating that strong signals are well captured by the reanalysis. In total, we find a positive anomaly for $\langle \mathbf{V} \cdot \mathbf{F}_A \rangle$ of about 2 W m^{-2} when averaging over the entire tropical Pacific region. This confirms the assumption that this region acts as a heat source for the extratropics during El Niño. However, as stated above, the contrary behavior of other tropical regions (mainly the Atlantic) more than compensates for this positive anomaly (during the peak of El Niño).

The direct estimates generally show the same peak anomaly, which again points out the similarity of the two calculation methods in terms of model dependency. From Fig. 12 we can also see temporal inhomogeneity of the vertical fluxes as all flux components become weaker in the early 2000s. During that time, analysis increments and also their variability decrease.

An interesting point of view arises from a longitude–time Hovmöller plot of tropical energy exports (Fig. 13). It clearly shows the modulation of energy exports from the Pacific region by ENSO. Positive anomalies over the eastern Pacific can be found for every maximum of the Niño-3.4 index (1992, 1995, 1997, 2003, 2005, and 2007), but, as stated above, obviously not every ENSO-correlated maximum over this region leads to a signal in the zonally
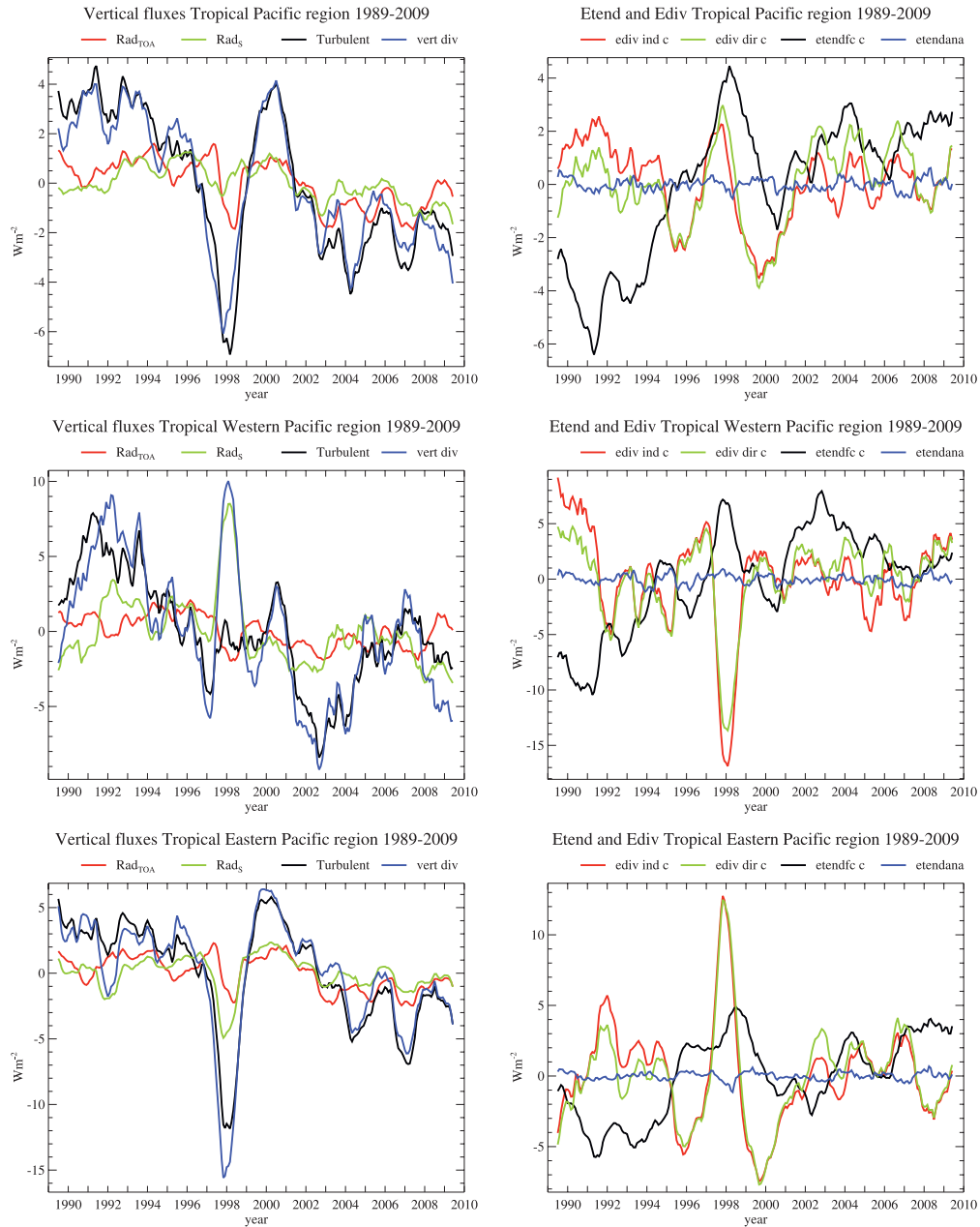
FIG. 12. (left) Anomalies of Rad_{TOA}, LH + SH, Rad_S and vertical flux divergence. (right) Anomalies of $\langle \partial e/\partial t \rangle^c_{fc}$, $\langle \partial e/\partial t \rangle^c_{ana}$, $\langle \mathbf{V} \cdot \mathbf{F}_A \rangle^c_{ind}$, and $\langle \mathbf{V} \cdot \mathbf{F}_A \rangle^c_{dir}$. (top) Averages over the tropical Pacific region (30°N–30°S, 110°E–80°W). (middle) Averages over the tropical western Pacific region (30°N–30°S, 110°E–170°W). (bottom) Averages over the tropical eastern Pacific region (30°N–30°S, 170°–80°W).

integrated curve (Fig. 8). On the one hand, the behavior of the western Pacific region is important as it tends to damp the eastern Pacific anomaly (e.g., in 1997/98). On the other hand, the non-Pacific tropical regions are sometimes deciding for the sign of the total export anomaly.

Analogous longitude–time Hovmöller plots showing the contribution from turbulent surface flux and radiative flux divergence anomalies to the longitude-dependent energy exports (not shown) suggest the turbulent fluxes to be the dominating driver.

FIG. 13. Longitude–time Hovmöller plot of tropical energy export (30°N–30°S) anomalies from ERA-Interim (corrected indirect estimate).

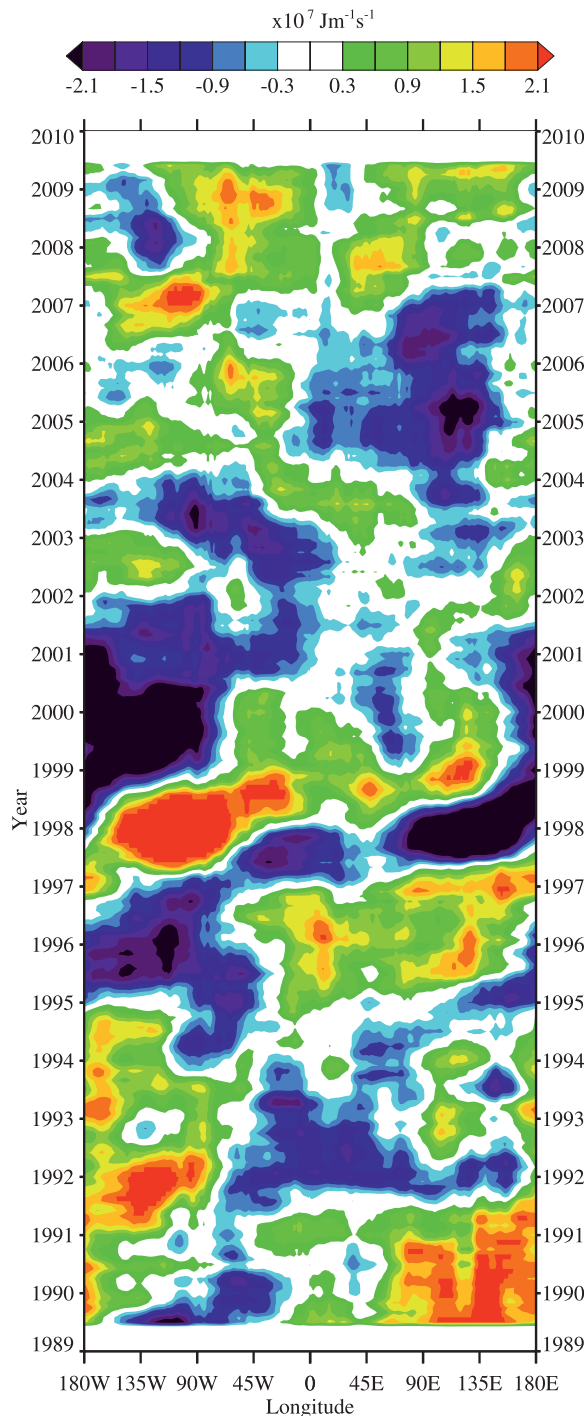An eastward-moving positive export anomaly starting in 1996 around 0° peaks over the eastern Pacific during the 1997/98 El Niño, can be traced as far as 140°E in 1999 (1.5 times around the globe), and looks quite coherent. Trenberth et al. (2002a), who also investigated the correlation between the Niño-3.4 index and $\langle \mathbf{V} \cdot \mathbf{F}_A \rangle$, found a signal of positive anomalies $\langle \mathbf{V} \cdot \mathbf{F}_A \rangle$ generally moving from the western to the eastern Pacific during El Niño events, which we can confirm with our results. The eastward-moving anomaly pattern between 1996 and 1999 requires further investigation as it appears to be linked to the positive Pacific anomalies in 1997/98.

An even more conspicuous and so far novel signal in Fig. 13 are the relatively slowly eastward-propagating negative (starting at 180°W around 2000 and arriving at 180°E around 2007) and positive (starting at 180°W in 2004/05 and reaching 180°E in 2009/10) export anomalies. They appear to be triggered by El Niño and La Niña events, respectively. Certainly, the signals are not very strong and have yet to be confirmed to be real. We note that Peterson and White (1998) found sea level pressure anomalies linked to ENSO propagating eastward with a phase speed comparable to the just described anomalies (5–7 yr). Nevertheless, it is necessary to investigate the reproducibility of these patterns with other datasets.

It is worth mentioning that all shown results concerning interannual variability are qualitatively the same when varying the latitudinal averaging interval (e.g., 20°N–20°S instead of 30°N–30°S).

5. Discussion and conclusions

The vertically integrated global energy budget has been evaluated, mainly using ERA-Interim reanalysis data. A direct and an indirect approach, both corrected for erroneous divergent mass fluxes in the forecast model, have been compared. The results for the zonally averaged divergent energy transports are quite similar and in good agreement with the results of FT08b. The only outlier is the indirect estimate from ERA-40 data, probably due to the unbalanced moisture budget. Additionally, the average CEF from the direct estimate are closer to zero, which appears to be more realistic. On a more regional scale, the indirect method leads to much smoother patterns of $\langle \mathbf{V} \cdot \mathbf{F}_A \rangle$ than the direct method, which suffers from its relatively coarse time resolution and numerical artifacts over high topography. Trenberth et al. (2001), also using a direct calculation method, reduced the noise by employing a tapered filter. Comparison to results obtained from ERA-40 with the same methods disproves the assumption that the indirect method is more model dependent. In fact, the noise of the direct estimate leads to relatively large differences between the ERA-40 and

ERA-Interim results, whereas the indirect estimate benefits from the higher time resolution.

However, computation of $\langle \mathbf{V} \cdot \mathbf{F}_A \rangle$ at the time resolution of the forecast model and archiving the 6-hourly time averages at ECMWF or other centers would significantly decrease the noise in the directly estimated fields. Possibly, applying this method during the production of a future reanalysis would render the indirect method unnecessary for energy budget evaluations.

Although ERA-Interim shows much better physical consistency than ERA-40, it still has shortcomings, which affect the energy budgets. Radiation at TOA is not balanced, leading to a global net energy loss of 1.2 W m^{-2}. Comparison to CERES and ISCCP-FD shows that the net energy input is generally too weak in the tropics and the net energy loss is underestimated in the extratropics. Thus, using Rad$_{\text{TOA}}$ alone for the computation of the total poleward energy transports (atmosphere + ocean) leads to an underestimation of this quantity by up to 0.9 PW. In the indirect estimate of $\langle \mathbf{V} \cdot \mathbf{F}_A \rangle$, it is absolutely necessary to consistently use forecasted energy tendencies [and no analyzed tendencies, see Eq. (2)] as they compensate the flawed meridional structure of Rad$_{\text{TOA}}$ to some extent.

Latitude–time Hovmöller plots of Rad$_{\text{TOA}}$ and Rad$_S$ from ISCCP-FD and ERA-Interim show the superiority of ERA-Interim in terms of homogeneity in time. Compared to ERA-Interim, ISCCP-FD data is not suitable for investigation of interannual variations of the energy budget but the data are being reprocessed (K. E. Trenberth 2011, personal communication), which will certainly lead to an improvement. Latitude–time Hovmöller plots of Rad$_{\text{TOA}}$ from CERES and ERA-Interim show generally very good agreement in terms of timing and location of anomalies. The comparison to CERES also shows that some apparently missing anomalies in ERA-Interim are likely masked by small inhomogeneities. When considering anomalies of a certain period, a possibility to get more homogeneous anomaly time series would be to determine break points and to compute separate climatologies before and after the shift.

Surface fluxes in ERA-Interim are not well balanced over the oceans [+6.8 W m^{-2} on average, a realistic value would be <1 W m^{-2} (Hansen et al. 2005)], whereas F_S over land is relatively good (−0.1 W m^{-2} on average). Moreover, the accuracy of surface flux anomalies (especially in connection with ENSO) is difficult to verify. There do not exist any longtime purely in situ measured turbulent surface flux datasets over large oceanic regions, which could be used as completely reanalysis-independent reference dataset, but one can use climate model output. Indeed, these fields are computed from parameterizations similar to those implemented in the ERA-Interim forecast model. However, Chiodo and

Haimberger (2010) found quite good quantitative agreement between anomalous surface fluxes from ECHAM5–AMIP and ERA-Interim, which is at least some encouragement to trust the reanalyzed fields.

Correlation analysis shows ENSO to be the dominating factor of interannual variations of the moist, dry and total energy budget over the tropical Pacific. Total tropical energy export (180°W–180°E) shows a quite weak peak correlation coefficient of 0.29 at a 9-month lag. The correlation curve (Fig. 10 on the left) being relatively broad and flat indicates that a connection to ENSO exists but each El Niño–La Niña event has its own signature and course. After that, we concentrated on variations of the single fields contributing to the energy budget over the tropical Pacific during the strong 1997/98 event. Hardly surprising, turbulent heat flux anomalies dominate the vertical flux divergence during the El Niño, with anomalous strong fluxes out of the ocean (6 W m^{-2} stronger on average over 30°N–30°S, 110°E–80°W). Whereas Rad$_{\text{TOA}}$ and Rad$_S$ show comparatively weak anomalies during that time, the forecasted total energy tendency (with the main contribution from the moisture tendency) shows a positive anomaly compensating for large parts of the turbulent flux anomaly. Comparison with regional analysis increments proves the regional forecast tendency anomalies to be erroneous. As precipitation does not affect the total energy budget [see Eq. (1)] directly, either $\langle \mathbf{V} \cdot \mathbf{F}_A \rangle$ is too weak or evaporation is too strong during the first 12-h forecast. Direct and indirect estimates of $\langle \mathbf{V} \cdot \mathbf{F}_A \rangle$ show anomalies of equal magnitude in 1997/98 and thus are model dependent to the same degree. However, an undeniable advantage of the indirect method is the possibility to investigate the impact of the forcing fields on $\langle \mathbf{V} \cdot \mathbf{F}_A \rangle$ in a more consistent way (the divergence and forcing fields are 12-h forecasts), whereas the direct estimate is evaluated from analyzed fields but the forcing fields are not available as analyses.

When splitting the tropical Pacific into eastern and western part, one can see that ERA-Interim has difficulties in representing the relatively dry conditions over the western Pacific (110°E–170°W, middle row in Fig. 12) during an El Niño event. Because of the reversal of the Walker circulation during El Niño, relatively weak cloud coverage prevails over that region, leading to a strong negative precipitation and a positive Rad$_S$ anomaly (more solar radiation arrives at the surface) whereas the turbulent fluxes show no mentionable anomalies. In sum, this results in a positive anomaly of the vertical flux divergence (+10 W m^{-2} in early 1998, see left panel in the middle row in Fig. 12). At the same time, the forecasted total energy tendency (again with the main contribution from the moisture tendency) also shows a positive anomaly. Thus, without any contribution

36

from anomalous turbulent fluxes, forecasted moisture tendencies show a positive anomaly. The reason must be the anomalously low forecasted precipitation. It is likely that the ERA-Interim analyses over the western Pacific were generally too dry compared to the ERA-Interim model climate during 1997/98, leading to a moistening (and thus positive moisture tendency forecasts) of the atmosphere during the first 12-h forecast segment.

Longitude–time Hovmöller plots of tropical energy exports (Fig. 13) exhibit an interesting new perspective on the interannual variations of the tropical energy budget. The Pacific region generally shows the strongest anomalies. Each peak of the Niño-3.4 index coincides with a dipole of positive (negative) export anomalies over the eastern (western) Pacific. This dipole often leads to no net anomaly over the Pacific, which is an additional reason for the relatively weak correlation between ENSO and the total energy exports.

Interesting eastward anomaly patterns caught our attention as they seem to appear to have some correlation with ENSO. Especially between 1996 and 1999, a positive anomaly can be tracked propagating around the globe about 1.5 times. A generally eastward-moving anomaly from the western to the eastern Pacific during El Niño events is documented in Trenberth et al. (2002b), but not to such a large extent. Analogous longitude–time Hovmöller plots of the single contributing fields suggest turbulent surface flux anomalies to have the largest impact on the described longitude-dependent anomalies. However, uncertainties in the fields exist and a next step will be to check the reproducibility of these patterns with other reanalyses or climate model runs with prescribed SSTs.

REFERENCES

Berrisford, P., P. Kållberg, S. Kobayashi, D. Dee, S. Uppala, A. J. Simmons, and P. Poli, 2011: Atmospheric conservation properties in ERA-Interim. *Quart. J. Roy. Meteor. Soc.*, **137,** 1381–1399.

Carissimo, B. C., A. H. Oort, and T. H. Vonder Haar, 1985: Estimating the meridional energy transports in the atmosphere and ocean. *J. Phys. Oceanogr.*, **15,** 82–91.

Chiodo, G., and L. Haimberger, 2010: Interannual changes in mass consistent energy budgets from ERA-Interim and satellite data. *J. Geophys. Res.*, **115,** D02112, doi:10.1029/2009JD012049.

Dee, D. P., and S. Uppala, 2009: Variational bias correction of satellite radiance data in the ERA-Interim reanalysis. *Quart. J. Roy. Meteor. Soc.*, **135,** 1830–1841.

——, and Coauthors, 2011: The ERA-interim reanalysis: Configuration and performance of the data assimilation system. *Quart. J. Roy. Meteor. Soc.*, **137,** 553–597.

Fasullo, J. T., and K. E. Trenberth, 2008a: The annual cycle of the energy budget. Part I: Global mean and land–ocean exchanges. *J. Climate*, **21,** 2297–2312.

——, and ——, 2008b: The annual cycle of the energy budget. Part II: Meridional structures and poleward transports. *J. Climate*, **21,** 2313–2325.

Haimberger, L., 2006: Towards temporally homogeneous evaluations of the observed global atmospheric circulation. Habilitation thesis, University of Vienna, Vienna, Austria, 75 pp.

——, 2007: Homogenization of radiosonde temperature time series using innovation statistics. *J. Climate*, **20,** 1377–1403.

——, B. Ahrens, F. Hamelbeck, and M. Hantel, 2001: Impact of time sampling on atmospheric energy budget residuals. *Meteor. Atmos. Phys.*, **77,** 167–184.

Hansen, J., and Coauthors, 2005: Earth's energy imbalance: Confirmation and implications. *Science*, **308,** 1431–1435.

Loeb, N. G., B. A. Wielicki, D. R. Doelling, G. L. Smith, D. F. Keyes, S. Kato, N. Manalo-Smith, and T. Wong, 2009: Toward optimal closure of the earth's top-of-atmosphere radiation budget. *J. Climate*, **22,** 748–766.

Meehl, G. A., C. Covey, T. Delworth, M. Latif, B. McAvaney, J. F. B. Mitchell, R. J. Stouffer, and K. E. Taylor, 2007: The WCRP CMIP3 multimodel dataset. *Bull. Amer. Meteor. Soc.*, **88,** 1383–1394.

Minnis, P., E. F. Harrison, L. L. Stowe, G. G. Gibson, F. M. Denn, D. R. Doelling, and W. L. Smith, 1993: Radiative climate forcing by the Mount Pinatubo eruption. *Science,* **259,** 1411–1415.

Peterson, R. G., and W. B. White, 1998: Slow oceanic teleconnections linking the Antarctic circumpolar wave with tropical El Niño–Southern Oscillation. *J. Geophys. Res.,* **103,** 24 573–24 583.

Poli, P., S. B. Healy, and D. P. Dee, 2010: Assimilation of global positioning system radio occultation data in the ECMWF ERA-Interim reanalysis. *Quart. J. Roy. Meteor. Soc.,* **136,** 1972–1990.

Porter, D. F., J. J. Cassano, M. C. Serreze, and D. N. Kindig, 2010: New estimate of the large-scale arctic atmospheric energy budget. *J. Geophys. Res.,* **115,** D08108, doi:10.1029/2009JD012653.

Simmons, A. J., and D. M. Burridge, 1981: An energy and angular-momentum conserving vertical finite-difference scheme and hybrid vertical coordinates. *Mon. Wea. Rev.,* **109,** 758–766.

Stone, P. H., 2008: The atmospheric general circulation: Some unresolved issues. *Dyn. Atmos. Oceans,* **44,** 244–250.

Trenberth, K. E., 1991: Climate diagnostics from global analyses: Conservation of mass in ECMWF analyses. *J. Climate,* **4,** 707–722.

——, and J. T. Fasullo, 2010: Simulation of present-day and twenty-first-century energy budgets of the Southern Oceans. *J. Climate,* **23,** 440–454.

——, J. M. Caron, and D. P. Stepaniak, 2001: The atmospheric energy budget and implications for surface fluxes and ocean heat transports. *Climate Dyn.,* **17,** 259–276.

——, ——, ——, and S. Worley, 2002a: Evolution of El Niño–Southern Oscillation and global atmospheric surface temperatures. *J. Geophys. Res.,* **107,** 4065, doi:10.1029/2000JD000298.

——, D. P. Stepaniak, and J. M. Caron, 2002b: Interannual variations in the atmospheric heat budget. *J. Geophys. Res.,* **107,** 4066, doi:10.1029/2000JD000297.

Uppala, S. M., and Coauthors, 2005: The ERA-40 Re-Analysis. *Quart. J. Roy. Meteor. Soc.,* **131,** 2961–3012.

Zhang, Y., and W. B. Rossow, 1997: Estimating meridional transports by the atmospheric and oceanic general circulations using boundary fluxes. *J. Climate,* **10,** 2358–2373.

——, ——, A. A. Lacis, V. Oinas, and M. I. Mishchenko, 2004: Calculation of radiative fluxes from the surface to top of the atmosphere based on ISCCP and other global data sets: Refinements of the radiative transfer model and the input data. *J. Geophys. Res.,* **109,** D19105, doi:10.1029/2003JD004457.

——, ——, and P. W. Stackhouse Jr., 2006: Comparison of different global information sources used in surface radiative flux calculation: Radiative properties of the near-surface atmosphere. *J. Geophys. Res.,* **111,** D13106, doi:10.1029/2005JD006873.

——, ——, ——, A. Romanou, and B. A. Wielicki, 2007: Decadal variations of global energy and ocean heat budget and meridional energy transports inferred from recent global data sets. *J. Geophys. Res.,* **112,** D22101, doi:10.1029/2007JD008435.

4   Zonal structure of tropical atmospheric energy budgets and their response to ENSO

This article presents results from the investigation of the variability of atmospheric energy budgets in the tropics. Their response to ENSO is investigated using cross-correlation, composite and EOF analysis.

My contributions to this work were large parts of the design of the study, interpretation of the results (equal share with the co-authors) and accomplishment of all computations. Employing data from Modern Era-Retrospective Analysis for Research and Application (MERRA, Rienecker et al. 2011) required to develop a method for the mass-adjustment (described in the supplementary material of this publication) which did not exist prior to this publication. Moreover, I prepared all visualizations required for this publication and wrote the paper.

Mayer, M., Trenberth, K. E., Haimberger, L., and Fasullo, J. T., 2013: *The Response of Tropical Atmospheric Energy Budgets to ENSO.* Journal of Climate, 26, 4710–4724.

ᐁThe Response of Tropical Atmospheric Energy Budgets to ENSO*

MICHAEL MAYER

Department of Meteorology and Geophysics, University of Vienna, Vienna, Austria

KEVIN E. TRENBERTH

National Center for Atmospheric Research,** Boulder, Colorado

LEOPOLD HAIMBERGER

Department of Meteorology and Geophysics, University of Vienna, Vienna, Austria

JOHN T. FASULLO

National Center for Atmospheric Research,** Boulder, Colorado

(Manuscript received 18 September 2012, in final form 19 December 2012)

ABSTRACT

The variability of zonally resolved tropical energy budgets in association with El Niño–Southern Oscillation (ENSO) is investigated. The most recent global atmospheric reanalyses from 1979 to 2011 are employed with removal of apparent discontinuities to obtain best possible temporal homogeneity. The growing length of record allows a more robust analysis of characteristic patterns of variability with cross-correlation, composite, and EOF methods. A quadrupole anomaly pattern is found in the vertically integrated energy divergence associated with ENSO, with centers over the Indian Ocean, the Indo-Pacific warm pool, the eastern equatorial Pacific, and the Atlantic. The smooth transition, particularly of the main maxima of latent and dry static energy divergence, from the western to the eastern Pacific is found to require at least two EOFs to be adequately described. The canonical El Niño pattern (EOF-1) and a transition pattern (EOF-2; referred to as El Niño Modoki by some authors) form remarkably coherent ENSO-related anomaly structures of the tropical energy budget not only over the Pacific but throughout the tropics. As latent and dry static energy divergences show strong mutual cancellation, variability of total energy divergence is smaller and more tightly coupled to local sea surface temperature (SST) anomalies and is mainly related to the ocean heat discharge and recharge during ENSO peak phases. The complexity of the structures throughout the tropics and their evolution during ENSO events along with their interactions with the annual cycle have often not been adequately accounted for; in particular, the El Niño Modoki mode is but part of the overall evolutionary patterns.

Corresponding author address: Michael Mayer, Department of Meteorology and Geophysics, University of Vienna, UZA II, Althanstr. 14, 1090 Vienna, Austria.
E-mail: mima@univie.ac.at

1. Introduction

The global atmospheric energy budget provides a fundamental basis for understanding and investigating the processes shaping the earth's climate system. Many scientific publications during recent decades have dealt with the quantification of the long-term mean vertical and horizontal energy fluxes within and over the boundaries of the atmosphere (e.g., Lorenz 1967; Peixoto and Oort 1992; Hantel et al. 2005; Trenberth et al. 2009). Recent estimates of the mean annual cycle of various atmospheric flux quantities in a globally and a zonally

averaged framework, obtained from a variety of datasets and including an uncertainty assessment, are given in Fasullo and Trenberth (2008a,b).

Reanalyses, representing reprocessed gridded datasets of the three-dimensional atmospheric state covering a relatively long period of time, provide the possibility for estimating not only the climatological mean values but also the variability of budget terms such as radiative and turbulent fluxes as well as the divergence of energy transports (see, e.g., Trenberth and Stepaniak 2003a; Mayer and Haimberger 2012, hereafter MH12).

A major problem when exploring time variability with these datasets is their still imperfect temporal homogeneity, which is a consequence of the continually changing observing system (see, e.g., Chiodo and Haimberger 2010; Trenberth et al. 2011; MH12). For instance, in a zonally averaged framework, interannual variability of poleward total energy transports from reanalyses is relatively small (4% of the climatological mean value; see MH12) and difficult to distinguish from spurious discontinuities in the data. Hence, the influence of El Niño–Southern Oscillation (ENSO) on zonal mean tropical energy export is still hard to detect with current reanalyses, although it is well known that tropical energy budgets are strongly affected by ENSO (see, e.g., Trenberth et al. 2002a,b). Another consequence is the inability to properly analyze trends. However, MH12 found that the signal-to-noise ratio in computed energy budgets is much better when considering regional budgets separately (e.g., the eastern tropical Pacific region) rather than in a zonally averaged framework because strong east–west compensation of budget anomalies occurs in the tropics and reduces the magnitude of the signal.

The evolution of surface temperature, precipitation, outgoing longwave radiation, vertically integrated diabatic heating and divergence of atmospheric energy transports, and ocean heat content in the Pacific were documented using correlation and regression analysis for a limited period (1979–98) by Trenberth et al. (2002b) for contemporary relationships and with regard to the evolution using leads and lags in Trenberth et al. (2002a). They found a substantial diabatic component to the discharge and recharge of the ocean heat content during ENSO but most of the delayed warming outside of the tropical Pacific comes from persistent changes in atmospheric circulation forced from the tropical Pacific. A major part of the ocean heat loss to the atmosphere is through evaporation and is realized in the atmosphere as latent heating in precipitation, which drives teleconnections. In the tropical Pacific during large El Niño events, the anomalous divergence of the atmospheric total energy transports exceeds 50 W m^{-2} over broad regions for several months. The divergence of total energy

therefore includes a strong latent energy component that in turn supplies the dry static energy (DSE) component so that there is considerable compensation between these two portions (Trenberth and Stepaniak 2003a). Here we build on those conclusions and use another 14 yr of data to check for robustness of the conclusions.

It is a common approach to describe evolution of ENSO in terms of dependence of time and longitude of different fields. Many authors have shown longitude–time sections of fields such as sea surface temperature (SST), zonal wind stress, outgoing longwave radiation (OLR), or thermocline depth anomalies (see, e.g., Zebiak and Cane 1987; McPhaden 1999; Meinen and McPhaden 2000; Okumura and Deser 2010). MH12 first presented longitude–time variations of tropical total energy export across 30°N and 30°S for the period 1989–2010 and found some intriguingly coherent longitude–time anomaly patterns related to ENSO, which we further investigate in this study.

Herein, we focus on the zonal structure and variability of the vertically integrated divergence of total atmospheric energy (TEDIV), latent heat as derived from the vertically integrated moisture divergence (LEDIV), and dry static plus kinetic energy transports (DSEDIV) in the tropical strip (defined as the region between 20°N and 20°S). The variability of these divergences is of great interest, as it represents the integrated atmospheric response to the phases of the coupled ocean–atmosphere system, associated with varying surface fluxes and changes in atmospheric circulation (Trenberth et al. 2002a). For instance, variations of tropical moisture convergence inform us about regional strengthening/weakening of the Hadley circulation (Trenberth and Stepaniak 2003b). While previous studies (those cited herein and others) have delved into some aspects, new datasets have improved quality and resolution, as well as provided a much longer record. An understanding of this variability is motivated further by recent climate extremes, which while demonstrating a clear connection to ENSO are also likely to be influenced by a changing climate (see, e.g., Trenberth and Fasullo 2012).

After examining the climatological mean annual cycle and standard deviation of the zonally resolved energy divergence fields from 1979 to 2009 or to 2011, we investigate their interannual variations. For this purpose, we employ the three most recent third-generation reanalysis products European Centre for Medium-Range Weather Forecast (ECMWF) Interim Re-Analysis (ERA-I; Dee et al. 2011), Modern Era-Retrospective Analysis for Research and Application (MERRA; Rienecker et al. 2011), and National Centers for Environmental Prediction (NCEP) Climate Forecast System Reanalysis (CFSR; Saha et al. 2010). ERA-I and MERRA both are continually updated on a monthly basis and CFSR is available for 1979–2010. The period

contains several strong ENSO events, which dominate the low-frequency variability of the divergence fields. In the subsequent sections we explore this variability employing cross-correlation, composite, and EOF analysis. This will lead to a description of the ENSO cycle in terms of atmospheric energy budgets. In the discussion, we reconcile these findings within existing ENSO theories.

2. Data and methods

The input data for this study are vertical radiative and turbulent fluxes as well as vertical integrals of horizontal energy transports and their divergence from three third-generation reanalyses and a global precipitation dataset for comparison with the reanalyses fields.

ERA-I, the most recent reanalysis product of the ECMWF, was released in 2007 and has been constantly updated since then. In this study, data from 1979 to 2011 are used. This reanalysis has a horizontal resolution at T255 ($\Delta x \simeq 80$ km) on 60 vertical hybrid model levels and employs a 12-h four-dimensional variational data assimilation system.

CFSR, a product of the NCEP, is the first reanalysis employing a coupled atmosphere–ocean–land surface–sea ice model for data assimilation. The atmospheric model has a horizontal resolution at T382 ($\Delta x \simeq 50$ km) with 64 vertical levels and a three-dimensional variational data assimilation (3D-Var) system. Data used in this study cover the period 1979–2009.

MERRA is produced by the National Aeronautics and Space Administration (NASA) Global Modeling and Assimilation Office (GMAO). It employs the Goddard Earth Observing System atmospheric model and data assimilation system (GEOS-DAS) version 5, which exhibits a ½° latitude and ⅔° longitude horizontal resolution on 72 vertical levels. For data assimilation, the Incremental Analysis Update (IAU) method is employed. This study employs MERRA data covering 1979–2011.

In addition to the fields from reanalyses, precipitation fields from the Global Precipitation Climatology Project (GPCP) version 2.2 (for details, see Huffman et al. 2009) are employed.

The vertically integrated divergence of total energy transport TEDIV [$=\langle \mathbf{V} \cdot F_A \rangle$ in Eq. (1)] has to be balanced by the net radiation at the top of the atmosphere $\mathrm{Rad_{TOA}}$, the net surface fluxes $F_S = \mathrm{LH} + \mathrm{SH} + \mathrm{Rad}_S$ (where LH denotes latent heat flux, SH denotes sensible heat flux, and Rad_S denotes the net radiation at the surface; all vertical fluxes are taken to be positive downward), and the vertically integrated tendency of atmospheric total energy $\partial \langle e \rangle / \partial t$, which gives

$$\langle \mathbf{V} \cdot F_A \rangle = -\frac{\partial \langle e \rangle}{\partial t} - F_S + \mathrm{Rad_{TOA}}. \qquad (1)$$

The vertically integrated divergence of moisture transport [$=\langle \mathbf{V} \cdot q v_2 \rangle$ in Eq. (2), with specific humidity q and horizontal wind v_2] is balanced by evaporation E, precipitation P, and the tendency of total column water vapor $\partial \langle q \rangle / \partial t$. It can be written as

$$\langle \mathbf{V} \cdot q v_2 \rangle = -\frac{\partial \langle q \rangle}{\partial t} - P - E. \qquad (2)$$

Multiplication of Eq. (2) by the phase transition energy of vaporization L converts it to an equation for the divergence of latent heat transport (LEDIV) with units of watts per meter squared (29 W m^{-2} correspond to 1 mm day^{-1}). Physical constraints such as close to zero $\mathrm{Rad_{TOA}}$ and F_S or balanced $-P - E$ on the long-term global average are generally not satisfied in reanalyses, which is reflected in nonzero analysis increments [see Trenberth et al. (2011) and MH12 for a discussion of these issues].

The divergence terms in Eqs. (1) and (2) can be computed by either calculating the left (direct method) or right (indirect method) side of the equations, respectively. The direct estimate is calculated from analyzed fields of the atmospheric state variables, whereas the indirect estimate is obtained from 12-hourly forecasts of vertical fluxes and the energy tendency. The difference TEDIV − LEDIV yields

$$\mathrm{DSEDIV} = -\frac{\partial \langle \mathrm{DSE} \rangle}{\partial t} + \mathrm{LP} - \mathrm{SH} - \mathrm{Rad}_S + \mathrm{Rad_{TOA}}. \qquad (3)$$

Both the direct and the indirect method require a correction for mass inconsistencies in the forecast model in order to obtain meaningful results (see MH12 for a more detailed description of the methods). ERA-I results shown in this paper are exclusively obtained from the direct method. Energy divergences (also mass corrected) from CFSR were computed at the Climate Analysis Section (CAS) at the National Center for Atmospheric Research (NCAR) and obtained from the Climate Data Guide (https://climatedataguide.ucar.edu/). MERRA data used in this study have been provided by the GMAO at NASA Goddard Space Flight Center through the NASA Goddard Earth Sciences (GES) Data and Information Services Center (DISC) online archive. TEDIV and LEDIV from MERRA were calculated as proposed by Cullather and Bosilovich (2012). Additionally, we corrected MERRA energy divergences for mass inconsistencies in the same way as MH12 described for ERA-I (see also the supplemental material for a description of MERRA fields employed for mass correction).

Although large efforts are put into providing reanalysis data with best possible temporal homogeneity by using a fixed data assimilation system over the whole

period covered and by employing variational bias correction (Dee and Uppala 2009), shifts of several watts per meter squared can still be found in the calculated energy budgets (see, e.g., MH12; Trenberth et al. 2011), stemming from shifts in the observing system. These in-homogeneities complicate the interpretation of anomalies when using one climatology over the whole data period. To reduce the effect of these shifts, we calculate split cli-matologies: that is, we use different climatologies before and after a major detected discontinuity. The ERA-I moisture budget shows several discontinuities related to changes in the Special Sensor Microwave Imager (SSM/I) data stream, while moisture budgets in MERRA and CFSR are more affected by Television and Infrared Observation Satellite (TIROS) Operational Vertical Sounder (TOVS)/Advanced TOVS (ATOVS) transitions in 1998 and 2001 (see Trenberth et al. 2011). Splitting the climatology results in the removal of artifacts but at the expense of possible reduction of true climate variability. As a compromise, we employ three split climatologies for all diagnostics in this study, 1979–91, 1992–2002, and 2003–11 for ERA-I data and 1979–98, 1999–2002 and 2003–present for MERRA and CFSR, in order to remove the two most influential discontinuities from each dataset (please see the supplemental material for a comparison showing the impact of this method). The method does not seem to have adverse effects and is clearly beneficial both in terms of eliminating spurious changes and in reconciling the results among the reanalyses.

3. Results

a. Climatology and variability in the tropical strip

The annual cycle of energy divergences (more precisely, divergences of vertically integrated horizontal energy transports) in a zonally averaged framework have been presented elsewhere for an earlier period (e.g., Trenberth and Stepaniak 2003a; Trenberth and Smith 2008; Fasullo and Trenberth 2008b). However, to set the stage for the following sections, here we present the zonally resolved annual cycle of the fields of TEDIV, LEDIV, and DSEDIV and the respective annual cycle of standard deviations.

Tropical (20°N–20°S) average energy divergences show pronounced zonal structures with an imposed an-nual cycle. The total energy divergence TEDIV is gen-erally positive all the year round except for the eastern Pacific (Fig. 1a). During boreal winter [December–February (DJF)], energy export to the Northern Hemi-sphere (NH) is strongest over the Indo-Pacific warm pool and the Atlantic, with values exceeding 70 W m^{-2}. In austral winter [June–August (JJA)], highest TEDIV values (also around 70 W m^{-2}) are found over the Indian Ocean, indicating this area as main region of energy

export into the Southern Hemisphere (SH). Variability of TEDIV is relatively weak with standard deviations up to 20 W m^{-2} at most (Fig. 1d). Zonal mean TEDIV has a weak annual cycle, with values around 41 W m^{-2} in January decreasing to 35 W m^{-2} in August (plots of tropical average zonal mean annual cycles of the energy divergences as wells as their zonally averaged standard deviation are presented in the supplemental material).

Tropical latent energy divergence (Fig. 1b) features three major regions of convergence: (i) the Indo-Pacific warm pool with its high SSTs, strong convective ac-tivity, moist low-level inflow, and dry outflow aloft peaking in JJA with the Indian and Southeast Asian monsoon, and the landmasses of (ii) South America and (iii) Africa, where P exceeds E and thus negative LEDIV has to balance the water budgets. Regions of latent en-ergy convergence extend farther to the east between November and March as the South Pacific convergence zone (SPCZ) is more pronounced at this time of the year, while latent energy convergence is more concentrated during the monsoon season. Regions of moisture di-vergence occur in the Pacific east of the date line and in the Atlantic where evaporation from the subtropical oceans exceeds precipitation related to the intertropical convergence zone (ITCZ). The LEDIV peak over the Indian Ocean in JJA is related to strong moisture trans-port to the monsoon regions. Zonal mean LEDIV varies between −8 W m^{-2} in November and +5 W m^{-2} in June. These low values indicate that, on the zonal aver-age, almost all latent heat contained in atmospheric water vapor evaporated between 20°N and 20°S is used for driving the Hadley circulation and comparatively small amounts of moisture are exported from the trop-ical strip. Months of highest LEDIV variability (up to 50 W m^{-2} standard deviation in regions with LEDIV values around −50 W m^{-2} like the Indo-Pacific warm pool during DJF; see Fig. 1e) do not coincide with highest absolute values (JJA). This high DJF variabil-ity is related to ENSO as will be seen later. Especially high LEDIV values in JJA related to the monsoons show comparatively low variability (10–20 W m^{-2}).

When neglecting the tendency term (monthly means usually <2 W m^{-2} in the area of interest), DSEDIV equals the diabatic heating of the atmosphere [sometimes referred to as Q_1, such as in Trenberth et al. (2002b)], which in turn is dominated by latent heating and radiative cooling. Highest values (>100 W m^{-2}) are found over the Indo-Pacific warm pool (Fig. 1c), with strong con-vective precipitation and therefore low OLR values, leading to weak radiative cooling of the atmosphere. Weaker radiative cooling means stronger DSEDIV. In contrast, little precipitation and generally clear skies over large parts of the eastern tropical Pacific favor
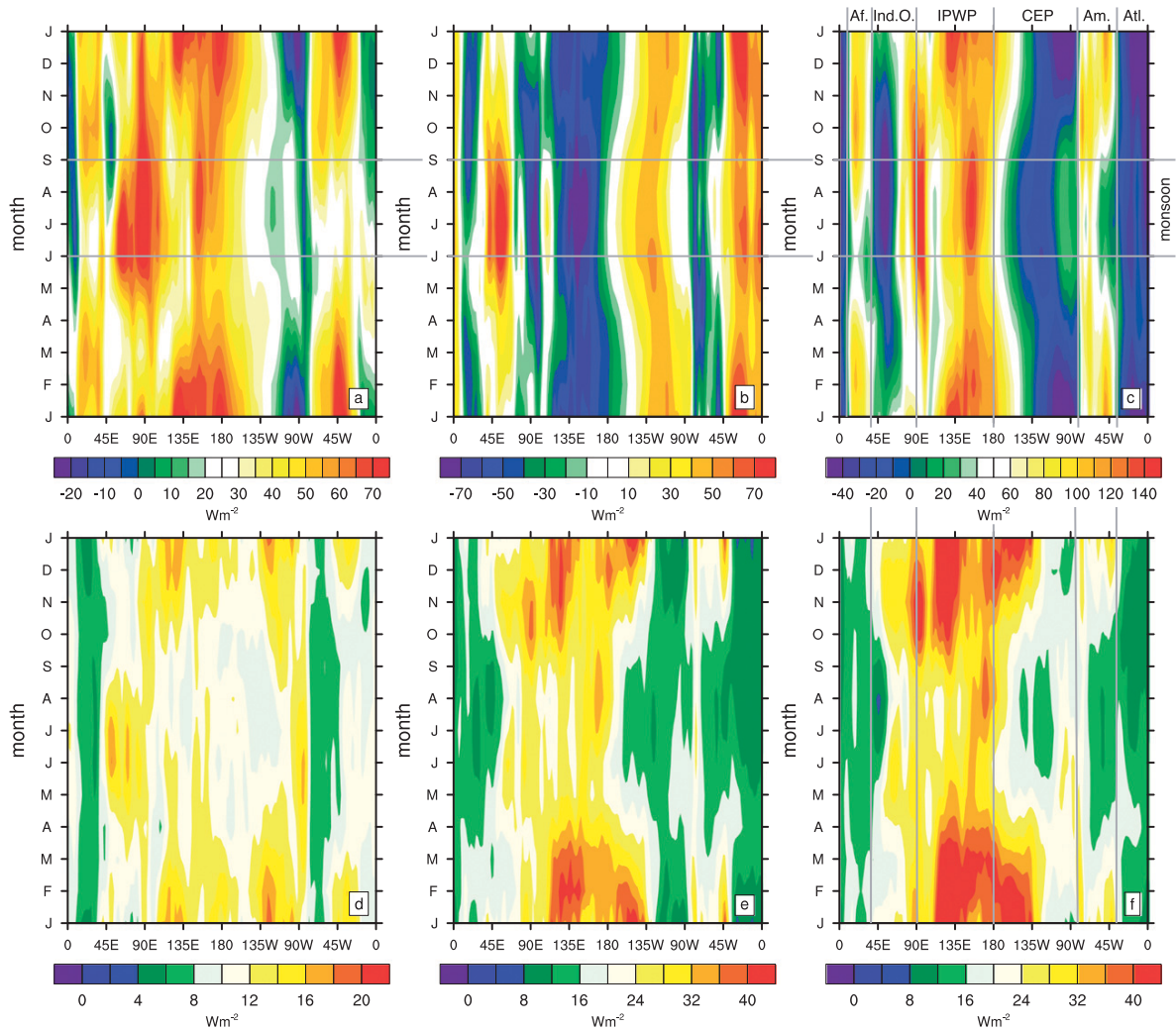
FIG. 1. Annual cycle of tropical (20°N–20°S) average monthly mean (a) TEDIV, (b) LEDIV, and (c) DSEDIV. Annual cycle of monthly standard deviation of (d) TEDIV, (e) LEDIV, and (f) DSEDIV, based on ERA-I. Regions referred to in the text are indicated by gray lines: Africa (Af.), Indian Ocean (Ind. O.), Indo-Pacific warm pool (IPWP), central–eastern Pacific (CEP), South America (Am.), and Atlantic (Atl.); Southeast Asian and Indian monsoon seasons are also indicated.

strong radiative cooling to space, balanced by convergence of dry static energy over large regions. Analogous to LEDIV, we find the broadening of positive DSEDIV values over the Indo-Pacific warm pool between November and March as well as the concentration during the monsoon season. DSEDIV standard deviation (Fig. 1f) is very similar to LEDIV standard deviation. Hence, the structure of DSEDIV variability is strongly coupled with the structure of latent heat release variability related to LEDIV variability in the tropics. Zonally averaged DSE export from the tropics varies from 46 W m^{-2} in November to 31 W m^{-2} in June and thus dominates total energy export from the tropics.

Comparison of the average annual cycle of LEDIV from the three employed reanalyses reveals considerable differences exceeding 20 W m^{-2} in some months and regions (not shown), which is on a similar order as the results of Trenberth et al. (2011), who showed differences in freshwater flux ($P + E$) between reanalyses. However, standard deviations from ERA-I and MERRA agree very well, with differences smaller than ± 5 W m^{-2}, while CFSR standard deviations differ by up to 10 W m^{-2} from the two others. Despite these rather large differences in the climatologies, we will show good agreement of the reanalyses in terms of interannual anomalies in section 3d.
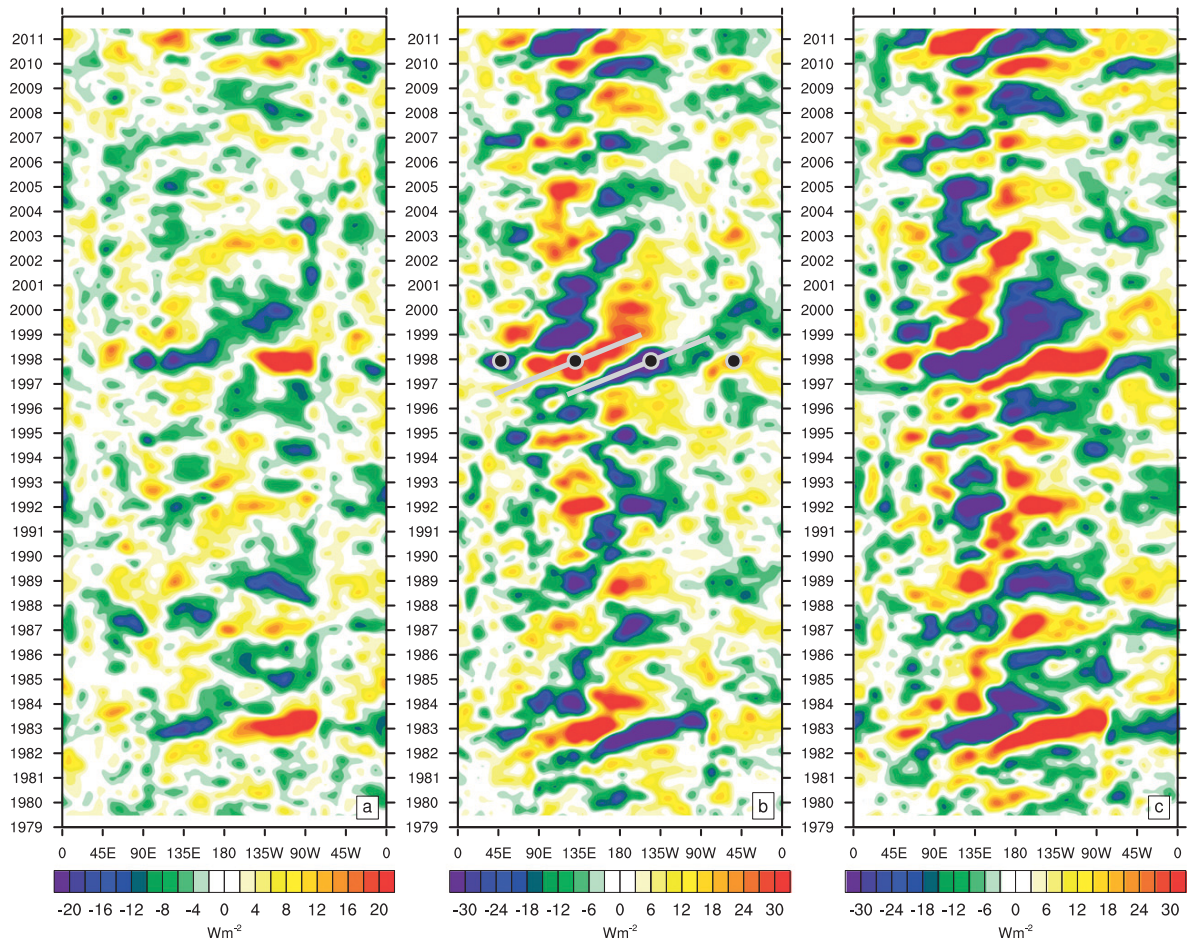
FIG. 2. Longitude–time Hovmöller plots of smoothed monthly anomalies of tropical (a) TEDIV, (b) LEDIV, and (c) DSEDIV from ERA-I. Filled circles in (b) indicate the quadrupole anomaly response to the 1997/98 El Niño event. Gray lines indicate the eastward propagation of the main anomaly maxima.

b. Longitude–time variability of the divergence fields

Longitude–time variability of TEDIV, LEDIV, and DSEDIV from ERA-I is depicted in Fig. 2. Anomalies of monthly averages are shown, averaged between 20°N and 20°S with a 2° zonal resolution. After calculation of these area averages, a 13-weight low-pass filter (weights are 1-6-19-42-71-96-106-96-71-42-19-6-1; see Trenberth et al. 2007) is applied to both zonal and time dimensions. This procedure is carried out for all fields shown in the following sections to emphasize large-scale interannual variations.

Tropical energy budgets exhibit strong anomalies with a pronounced zonal structure. TEDIV anomalies (Fig. 2a) can reach more than ± 20 W m^{-2} over large regions while LEDIV and DSEDIV anomalies can exceed ± 30 W m^{-2}. For LEDIV (Fig. 2b) and DSEDIV (Fig. 2c), a pronounced quadrupole structure can be observed

during ENSO extreme phases. During warm ENSO events (e.g., in 1982/83, 1986/87, 1991/92, 1994/95, 1997/98, 2002/03, and 2009/10), LEDIV shows negative anomalies (i.e., less divergence or more convergence) over the eastern Pacific region and to a smaller extent over the Indian Ocean, while positive LEDIV anomalies are found over the Indo-Pacific warm pool and the Atlantic. DSEDIV shows the same structures but of the opposite sign. DSEDIV anomalies are thus dominated by anomalous latent heat release stemming from precipitation related to anomalous LEDIV. The same applies for cold events (e.g., 1988/89, 1996/97, 2008/09, and 2010/11) but with the opposite sign. This anticorrelation is also apparent in a zonally averaged framework (see Fig. 9 in Trenberth and Smith 2008).

The amplitude of DSEDIV anomalies tends to exceed the amplitude of LEDIV anomalies because there is a sizeable additional contribution from anomalous
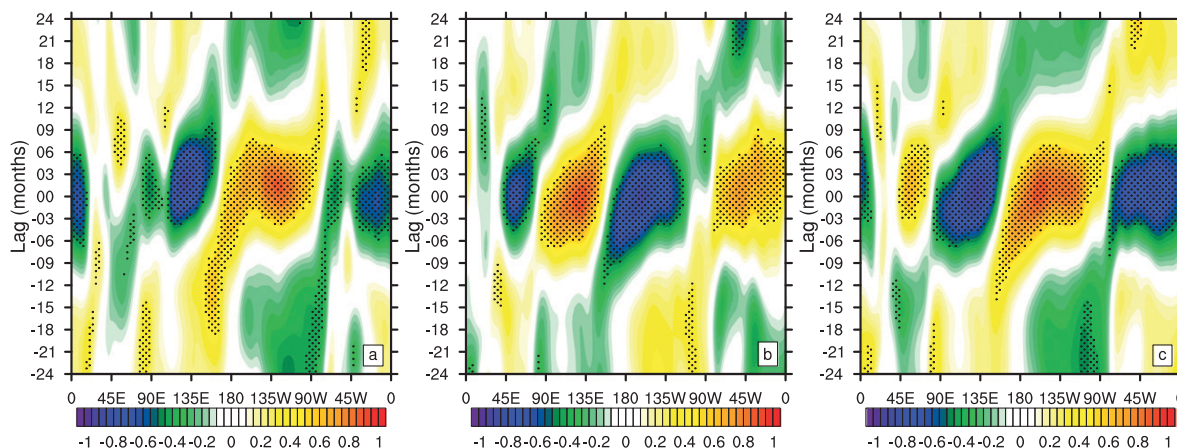
FIG. 3. Cross correlations of (a) TEDIV, (b) LEDIV, and (c) DSEDIV with Niño-3.4; stippling denotes correlations with significance >95%. Cross-correlation coefficients of all fields reach values up to ±0.9.

radiative flux convergence, which usually is in phase with LEDIV anomalies. A more detailed explanation for this will be given in section 3d.

Diabatic heating (cooling) is accompanied by rising (sinking) motion (i.e., diabatic heating drives thermally direct circulations). Hence, the observed quadrupole structure in DSEDIV and LEDIV is the signature of circulation anomalies in the vertical equatorial plane, which is one manifestation of the atmospheric bridge, discussed in detail by Alexander et al. (2004).

Total energy divergence (Fig. 2a) exhibits a structure similar to DSEDIV, but the anomalies are smaller by about 50%. Anomalies over the Indian Ocean and the Atlantic are small (usually <10 W m^{-2}). The most prominent feature is the ENSO-related dipole structure with negative (positive) values over the Indo-Pacific warm pool and positive (negative) values over the eastern equatorial Pacific during warm (cold) ENSO events (already described in MH12). As Rad$_{TOA}$ shows weak sensitivity to tropical SST (Trenberth et al. 2010) and $\partial\langle e\rangle/\partial t$ anomalies are small (analyzed tendencies <5 W m^{-2}), observed TEDIV anomalies are mainly associated with variations in F_S (radiative and turbulent fluxes). Thus, a positive TEDIV anomaly corresponds to either stronger than normal energy gain from the ocean or weaker than normal energy loss. Figure 2a shows clearly that there is always strong zonal compensation in TEDIV anomalies over the Pacific Ocean, and this is related to the Walker circulation. However, eastern Pacific TEDIV anomalies usually are not fully offset, and thus their sign determines the sign of the zonally averaged tropical Pacific TEDIV anomaly.

Another conspicuous feature, most noticeable from DSEDIV and LEDIV in Figs. 2b and 2c, is the coherent

anomaly pattern during the transitions between El Niño and La Niña, which is pervasive in the tropics. For example, in mid-1981, with weak La Niña conditions prevailing, a relatively weak quadrupole structure (as described above) is found with positive DSEDIV anomalies over and even slightly to the west of the Indo-Pacific warm pool. In the subsequent months and development of the strong 1982/83 El Niño, the DSEDIV anomalies shift eastward and reach the coast of South America, where they coincide with the peak of the event in late 1982. A similar evolution can be seen in LEDIV, with opposite sign, and in TEDIV (though much weaker). The evolution of the 1997/98 El Niño shows very similar structures. Hence, the decrease of trade winds, a fundamental feature of the El Niño onset phase (Clarke 2008), is associated with a gradually eastward shifting pattern of energy budget anomalies. These coherently propagating patterns can also be observed during the development of cold ENSO events, such as the major La Niña in 2010/11. In the subsequent sections, we will show that these transitional patterns are robust features of ENSO evolution during the studied period.

c. Cross correlations with ENSO

To see the statistical significance of the patterns found from Figs. 2a–c, we compute cross correlations of TEDIV, LEDIV, and DSEDIV with the Niño-3.4 index (SSTs averaged in 5°N–5°S, 120°–170°W) at every longitude for lags between −24 and +24 months. Cross correlation of total energy divergence with Niño-3.4 (Fig. 3a) shows the pronounced dipole structure over the tropical Pacific in phase with Niño-3.4. Over the Atlantic, additional significant anomalies of opposite sign to the eastern Pacific TEDIV anomalies occur. The strip of positive

correlations propagates eastward and achieves statistical significance near lag −18 (negative lags mean Niño-3.4 is leading) and is mainly related to the phase transition from warm to cold events, as can be seen, for instance, in Fig. 2a after the 1982/83 and 1997/98 El Niños (cooling SSTs coinciding with negative TEDIV anomalies).

The quadrupole response of LEDIV and DSEDIV to ENSO, described in section 3b, is confirmed by significant correlations at lag 0 (Figs. 3b,c), consistent with results shown in Fig. 10 of Trenberth et al. (2002a). Eastward propagation of anomalies during developing and declining ENSO events is also indicated by the cross correlations, achieving significant values near lag −12.

Finding propagating features also in TEDIV indicates that these patterns are not only a result of circulation changes leading to redistribution of latent heating and thus compensating anomalies of LEDIV and DSEDIV but also associated with net surface flux anomalies. Cross-correlation patterns at small lags of all three fields in Fig. 3 recur at larger positive and negative lags with opposite sign. This is consistent with the negative autocorrelation of Niño-3.4 at lags larger (smaller) than 10 (−10) months (the autocorrelation function of Niño-3.4 is shown in Fig. 6c, presented later).

d. Composites

As warm and cold ENSO events show asymmetry in length, spatial structure, and their evolution (e.g., Okumura and Deser 2010), it is not surprising that the propagating patterns described in section 3b are not depicted very well in cross-correlation analysis (section 3c). We considered the spatiotemporal evolution of the five strongest warm ENSO events (in terms of maximum Niño-3.4 anomalies) after 1978: namely, 1982/83, 1986/87, 1991/92, 1997/98, and 2009/10. As the 2009/10 event is not covered by our CFSR and MERRA data and thus comparison between the reanalyses is impossible, we show a composite analysis including only the three strongest warm ENSO events (1982/83, 1991/92, and 1997/98) in this section. The evolution of LEDIV for the five single El Niños as well as a five-event composite from ERA-I data is presented in the supplemental material. Prior to compositing, the anomaly fields for the single events have been centered at the month of the respective SST anomaly peaks.

Figures 4a–c show LEDIV composites from ERA-I, CFSR, and MERRA, respectively. All three reanalyses show negative LEDIV anomalies between 90° and 130°E around 15–18 months prior to the peak of the El Niños (in fact, at this time there can be seen a weak quadrupole structure as described in section 3b). This pattern then propagates eastward gradually, reaching the central and eastern Pacific at the peak of the El

Niños. At that time, the quadrupole structure shows up with anomalies exceeding ±25 W m^{-2}. During the decline of the event, the quadrupole again shifts eastward, so that, more than a year after the event peak, negative LEDIV anomalies reach the Atlantic. This coherent evolution in space and time is remarkable and much more prominent than in other fields such as SST (Fig. 4g). The three reanalyses agree quite well, but difference plots of the LEDIV composites (not shown) reveal differences of up to 10 W m^{-2} at times of largest anomalies. This is probably mainly related to varying magnitudes of analyzed moisture anomalies in the three datasets rather than their representation of circulation anomalies, as Trenberth et al. (2011) already found when comparing the climatologies of moisture transports. The qualitative agreement of longitude–time variability of total column water vapor in the three reanalyses is good, but there are considerable discrepancies in magnitude (not shown). We also investigated a possible connection between differing SST values used in the three reanalyses and differences in LEDIV anomalies. SST anomaly differences are on the order of 0.1 K over large regions, with CFSR SSTs being generally higher than those from ERA-I and MERRA prior to 1981 and after 2002. LEDIV and SST anomaly differences between the datasets are indeed significantly correlated in many regions along the equator, but correlations are much weaker and mostly insignificant when considered over the regions of our interest (20°N–20°S).

DSEDIV (Fig. 4e) shows a picture very similar to LEDIV, but of reversed sign. The magnitudes are even larger, indicating some contribution from the convergence of radiative fluxes, $\text{Rad}_S - \text{Rad}_{\text{TOA}}$ [see Eq. (3) and Fig. 4h]. This is the case because enhanced moisture flux convergence usually is accompanied by higher than normal total column water vapor and cloud coverage. The higher than normal cloud tops lead to stronger reflection of incoming solar radiation (RSR) and lower OLR. However, in sum Rad_{TOA} anomalies are small compared to Rad_S anomalies. Inspection of anomalous upwelling and downwelling shortwave and longwave fluxes at the surface from ERA-I (not shown) reveals that the largest contribution to Rad_S comes from reduced downwelling solar radiation (mainly due to increased RSR). Stronger than normal upwelling longwave radiation at the surface (due to higher SSTs) is largely offset by stronger than normal downwelling longwave radiation (due to increased moisture content in the atmosphere). In sum, these effects lead to a negative Rad_S anomaly. Hence, the result of approximately unaltered net radiation at TOA ($\text{Rad}'_{\text{TOA}} \simeq 0$) and a negative net surface radiation anomaly ($\text{Rad}'_S < 0$) is reduced divergence of radiative fluxes (i.e., reduced radiative cooling; $\text{Rad}'_S - \text{Rad}'_{\text{TOA}} < 0$) in
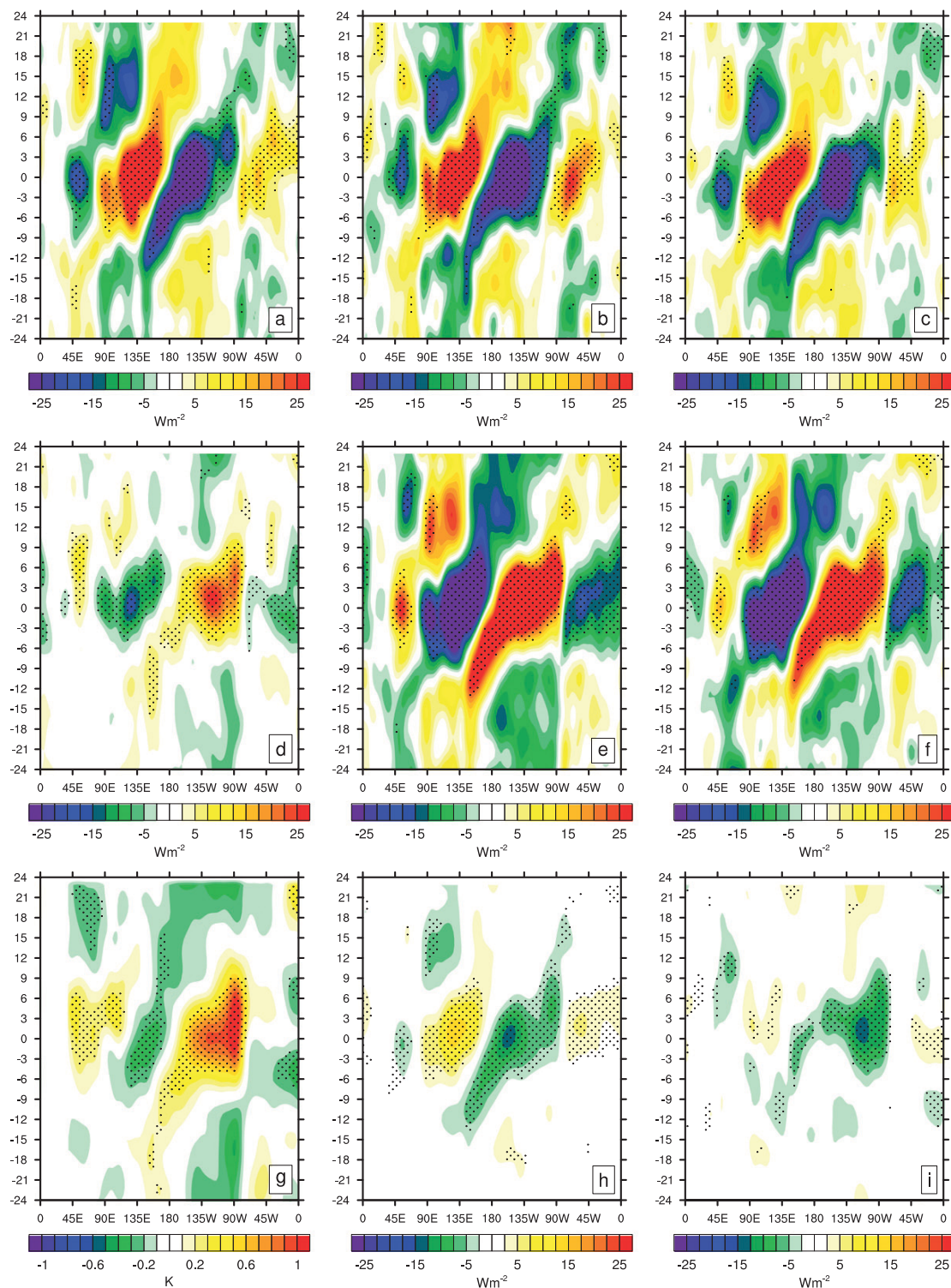
FIG. 4. Composites of anomalous tropical LEDIV from (a) ERA-I, (b) CFSR, and (c) MERRA; (d) TEDIV, (e) DSEDIV, (g) SSTs, (h) Rad$_S$ − Rad$_{TOA}$, and (i) LH from ERA-I; and (f) precipitation from GPCP, for the three strongest El Niños after 1978. Values on the *y* axis denote months before (negative values) or after (positive values) the SST peak (according to Niño-3.4); stippling denotes anomalies with significance >90%.
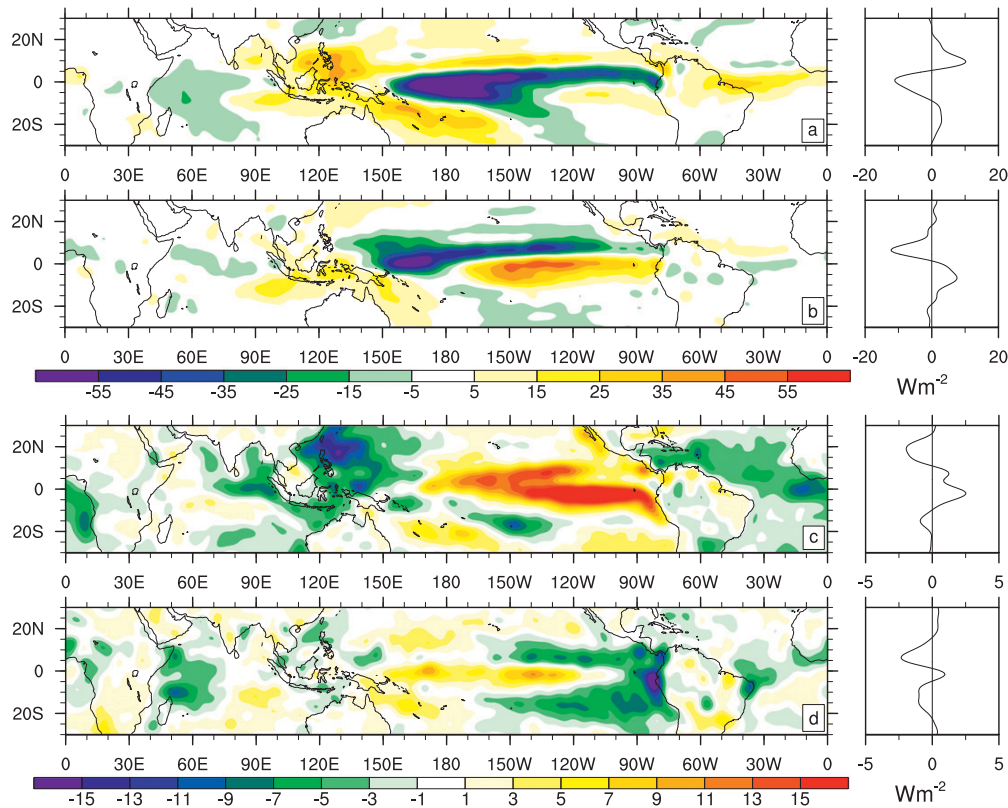
FIG. 5. (a) EOF-1 (28.1% variance explained) and (b) EOF-2 (17.5% explained) from ERA-I LEDIV; (c) EOF-1 (23.5% explained) and (d) EOF-2 (8.9% explained) from ERA-I TEDIV. Left panels show vertical integrals, right panels the respective zonal averages. All fields are multiplied by the standard deviation of the respective PCs; signs are chosen for warm ENSO events.

association with enhanced moisture flux convergence. The opposite is true for weaker than normal moisture flux convergence. While Rad_S anomalies alter the surface energy budget also during the transition period, anomalous evaporation is small more than a year from the SST peak (Fig. 4i). In agreement with Wallace and Shukla (1983) we find that by far the strongest contribution to ENSO-related precipitation anomalies stems from circulation (i.e., LEDIV) anomalies rather than evaporation anomalies. This is also confirmed by GPCP precipitation (Fig. 4f), which show structures in excellent agreement with LEDIV.

Compared to DSEDIV, TEDIV shows similar but weaker structures. Maximum anomalies reach 20 W m^{-2} over the eastern Pacific during the El Niño peaks, at times of maximum evaporation anomalies. The main difference in comparison to DSEDIV is the very weak transition pattern (anomaly < 5 W m^{-2} at 180° around −6 months) from cold to warm ENSO state. We conclude that the propagating patterns seen from LEDIV and DSEDIV during the transition phase are associated with changes of

the circulation while the signal in net surface flux and TEDIV is small at these times.

e. EOF analysis

An EOF analysis of tropical LEDIV, TEDIV, and DSEDIV is performed using a covariance matrix (fields on the full grid are first truncated at T42 and then weighted with the square root of the cosine of the latitude). We present the first two ERA-I LEDIV EOFs in Figs. 5a and 5b and the first two ERA-I TEDIV EOFs in Figs. 5c and 5d. The generally large structural differences between LEDIV and TEDIV EOFs in Figs. 5a–d are immediately apparent. They stem from the dominance of precipitation in LEDIV, while latent heat release (being just a conversion from latent to dry static energy) does not alter total energy.

The first LEDIV EOF (Fig. 5a) resembles canonical El Niño patterns, with enhanced moisture convergence along the equator from 140°E stretching to the coast of South America, surrounded by weaker than normal moisture convergence. The zonal mean (to the right of
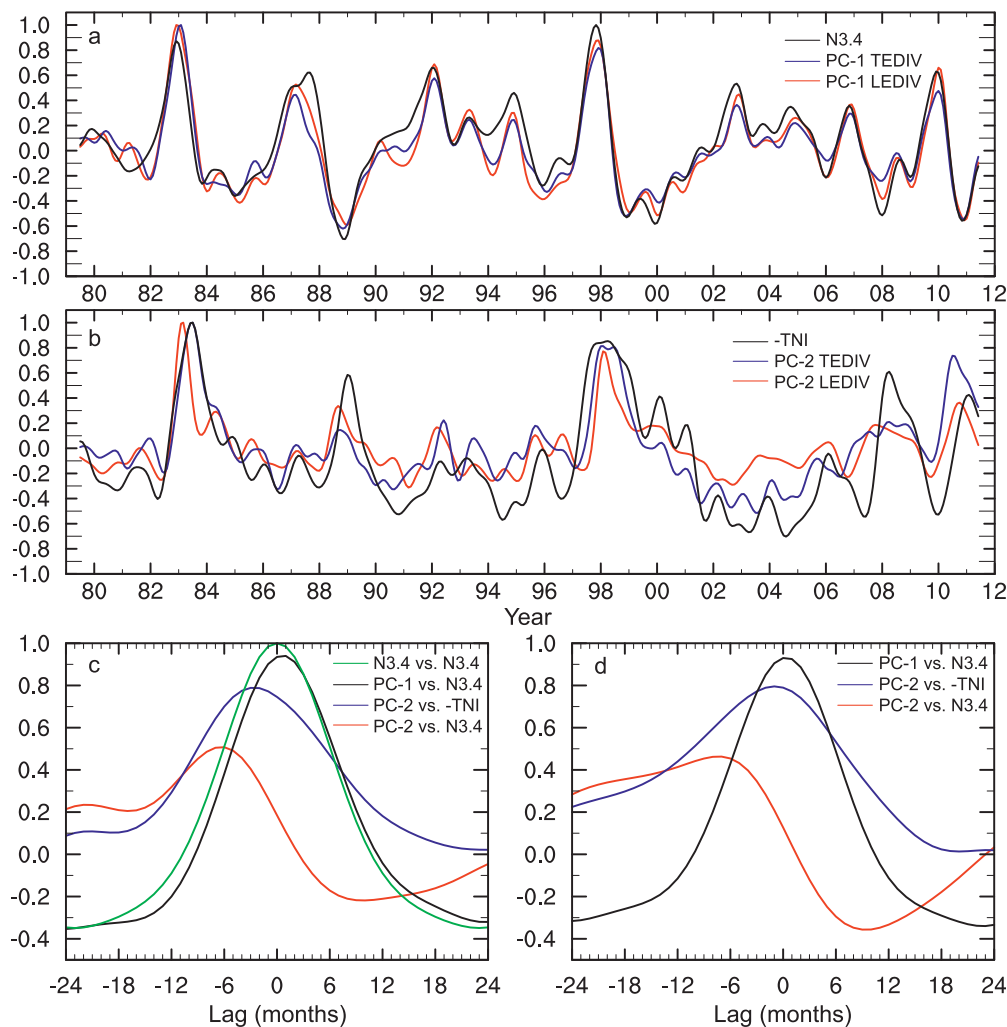
FIG. 6. Normalized (a) PC-1 of LEDIV and TEDIV as well as Niño-3.4 index, (b) PC-2 of LEDIV and TEDIV as well as −TNI and cross correlations of (c) LEDIV PCs and (d) TEDIV PCs with Niño-3.4 and −TNI (negative lag means respective PC is leading).

Fig. 5a) shows the well-known southward shift of the ITCZ and the northeast shift of the SPCZ (Clarke 2008). The quadrupole structure is also obvious, with its two major poles over the Indo-Pacific warm pool and central/eastern Pacific and its secondary poles over the Indian Ocean and Atlantic. LEDIV PC-1 and Niño-3.4 as well as their cross-correlation function are shown in Figs. 6a and 6c, respectively. PC-1 is correlated 0.95 with Niño-3.4 at lag 1 month. Hence, this mode is almost synchronized with SSTs. Coherence with ENSO is also evident for the first EOFs of DSEDIV (not shown) and TEDIV (Figs. 6a,d).

EOF-2 (Fig. 5b) of LEDIV shows an area of enhanced moisture convergence along the equator, extending farther to the west than in EOF-1. The zonal average of

EOF-2 indicates a northward shift of the ITCZ. This pattern resembles El Niño Modoki (Ashok et al. 2007) SST patterns. Indeed, PC-2 is correlated 0.78 with the Trans-Niño Index [TNI; as defined in Trenberth and Stepaniak (2001); signs have been reversed to be positive for warm El Niño Modoki state] at lag −3 months (Figs. 6b,c). Thus, EOF-2 anomaly patterns occur prior to corresponding SST anomalies. Furthermore, PC-2 shows maximum correlation with Niño-3.4 at lag −6, indicating that EOF-2 resembles the El Niño onset phase but may also arise from the required orthogonality of EOFs. EOF-2 of DSEDIV is very similar but with reversed signs (not shown). EOF analysis does reveal a pattern corresponding to El Niño Modoki for TEDIV also (EOF-2; Fig. 5d). However, the explained
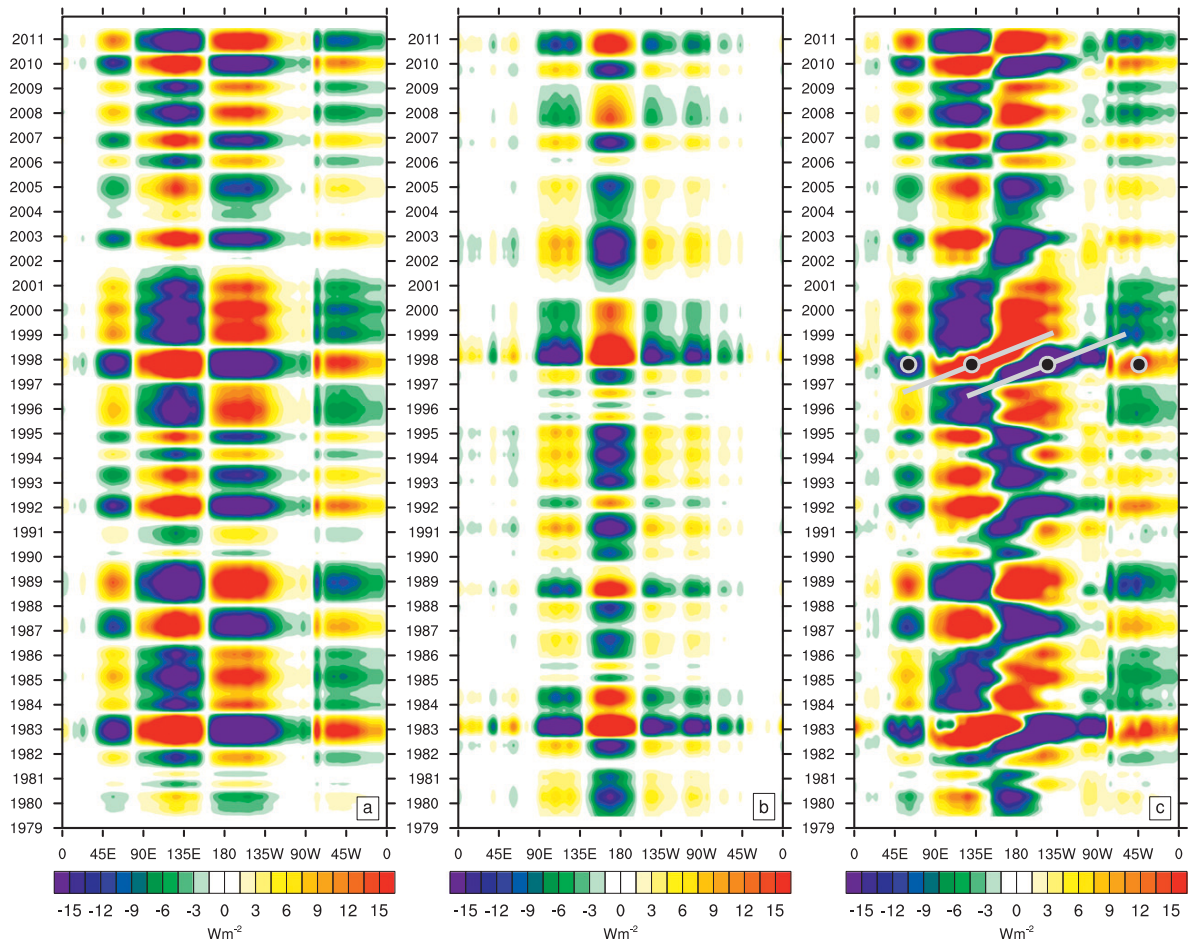
FIG. 7. Longitude–time Hovmöller plots of smoothed monthly anomalies of tropical LEDIV from ERA-I reconstructed from (a) EOF-1, (b) EOF-2, and (c) EOF-1 + EOF-2 and their respective PCs. Filled circles in (c) indicate the quadrupole anomaly response to the 1997/98 El Niño event. Gray lines indicate the eastward propagation of the main anomaly maxima.

variance of EOF-2 is less than 9%. Hence, TEDIV anomalies and consequently anomalous net energy exchanges between ocean and atmosphere are relatively weak for El Niño Modoki conditions. The lead–lag relationships with Niño-3.4 and −TNI shown in Figs. 6c and 6d are quite similar to those found by Trenberth et al. (2002b), who performed singular value decomposition (SVD) analyses of reanalyzed TEDIV and diabatic heating fields for 1979–2001.

The discussed LEDIV EOFs are significant according to North et al. (1982) at the 95% confidence level across all three reanalyses. TEDIV EOFs are significant only from ERA-I fields, while TEDIV EOF-1 and EOF-2 are not well separated in MERRA and CFSR data. We also examined cross correlations of both LEDIV and TEDIV PC-2 with the El Niño Modoki Index (as defined in Ashok et al. 2007) instead of TNI and the results were very similar.

Reconstructed LEDIV time series using EOF-1 and EOF-2, their respective PCs, and their sum are shown in Figs. 7a–c, respectively. Figure 7a resolves the quadrupole structures of tropical LEDIV anomalies with alternating signs and values exceeding ± 15 W m^{-2}. This figure also makes clear that this signature is apparent nearly throughout the whole data period with alternating sign.

Anomaly series reconstructed from EOF-2 and PC-2 (Fig. 7b) shows the tripole anomaly structure related to El Niño Modoki. The center of moisture convergence during warm El Niño Modoki conditions (e.g., in 1982) is centered slightly west of the date line. This center lies between the two anomaly centers of EOF-1 in the Pacific region (Indo-Pacific warm pool and eastern Pacific). Anomaly values related to EOF-2 are generally smaller than those related to EOF-1. Qualitatively, the warm Modoki phase appears to last longer than the cold phase.

51

The sum of the two reconstructed series is shown in Fig. 7c. It clearly resembles the coherent time-space structures already seen from Fig. 2b, with west–east transition of negative LEDIV anomalies for the strong El Niños in 1982/83, 1991/92, and 1997/98 but also west–east transition of positive anomalies related to cold ENSO events (e.g., prior to the 1999 or 2011 La Niñas). Reconstructed DSEDIV shows qualitatively the same with reversed sign (not shown). This means that we are able to reconstruct the main features of tropical energy divergence anomalies related to ENSO evolution from the first two EOFs and their respective PCs. This is in agreement with Trenberth and Smith (2006), who found for other fields such as temperature at different vertical levels that at least two EOFs are required to depict ENSO evolution.

4. Discussion and conclusions

The zonal structure and variability of the tropical energy budget has been investigated, employing data from third-generation ERA-I, MERRA, and CFSR. A distinct and robust response to ENSO can be found in the longitude–time variability of the energy divergences. LEDIV features anomalies with a pronounced quadrupole structure, with negative values over the central/eastern Pacific and the Indian Ocean and positive anomalies over the Indo-Pacific warm pool as well as the Atlantic Ocean during warm events (the opposite applies for cold events). The main driver for this atmospheric response is positive SST anomalies over the eastern Pacific, which induce stronger than normal moisture convergence (i.e., negative LEDIV anomalies) and consequently latent heating due to precipitation anomalies in this region. The rising motion associated with these anomalies leads not only to a reversal of the Walker circulation and thus anomalous descending motion over the Indo-Pacific warm pool (i.e., weaker than normal rising motion) but also a descending branch over the tropical Atlantic (see, e.g., Klein et al. 1999). Circulation anomalies are directly reflected in LEDIV. The fourth pole is related to positive SST anomalies over the Indian Ocean, usually associated with warm ENSO events (see also Klein et al. 1999), leading to negative LEDIV and positive vertical motion anomalies. DSEDIV exhibits qualitatively the same response with reversed sign, but even enhanced magnitudes of the anomalies, because LEDIV and Rad_S (positive downward) are positively correlated. This quadrupole structure is also evident in the first EOF of tropical LEDIV (Fig. 7a). The peak phase of warm events is also the time when net surface fluxes contain a significant negative anomaly, with large contribution from stronger than normal

evaporation over the central–eastern Pacific, leading to a positive TEDIV anomaly. As TOA net radiation perturbations are small, TEDIV anomalies are largely a manifestation of the ocean heat discharge phase as proposed by Jin (1997), which is maintained not only by poleward ocean heat transports but also by anomalous evaporative cooling of the ocean (see, e.g., Trenberth et al. 2002b).

However, LEDIV coupling to SST is not of the same strength everywhere. This becomes clear when considering the El Niño evolution composited over the three major warm ENSO events in 1982/83, 1991/92, and 1997/98. Around 15–18 months ahead of the respective peaks of these El Niños, LEDIV anomalies feature a quadrupole structure typical for La Niña conditions. Indeed, over the eastern tropical Pacific, leading negative SST anomalies are evident and a weak positive SST anomaly exists west of the date line (Fig. 4g). This anomaly arises from eastward advection of warm Indo-Pacific warm pool water, which extends farther in the following months, in support of the initialization of the next warm event (Sarachik and Cane 2010). However, at that time negative LEDIV anomalies (i.e., stronger than normal moisture convergence) extend to the west as far as 80°E. This cannot be explained only from the small warm SST anomaly, which is located much farther to the east. Obviously, LEDIV is more weakly coupled to local SST over the Indo-Pacific warm pool than it is over the central–eastern Pacific. LEDIV anomalies over the Indo-Pacific warm pool compensate for LEDIV anomalies over the central–eastern Pacific, which in return are strongly SST driven. In the subsequent months, the initially small warm SST anomaly slowly propagates eastward until the mature El Niño phase begins developing some 6 months before the event peak.

Zebiak and Cane (1987) found that strongest ENSO-related wind stress anomalies were around the date line, driving the eastward propagation of warm SST anomalies and also exciting the eastward propagating equatorial Kelvin waves that initialize El Niño events. These wind stress and SST anomalies are also associated with moisture divergence anomalies in that region. EOF-2 of LEDIV (Fig. 5b) depicts this transition state, with stronger than normal moisture convergence around the date line. PC-2 consistently shows strongest correlation with −TNI at lag −3 ($r = 0.8$), indicating the atmosphere's leading role during this phase. Thus, the apparent eastward propagation of negative LEDIV anomalies (and correspondingly positive DSEDIV anomalies) associated with strong El Niño events (see, e.g., Fig. 2b) is due to the seamless transition between La Niña and El Niño, during which the atmospheric circulation alternately takes a leading and a responding part. The strong 1982/83 and

52

1997/98 El Niños (and also others such as the 2009/10 event) show remarkable agreement regarding their spatiotemporal evolution, while other strong warm events evolve differently (Fig. 2), such as the 1991/92 event, which exhibits a much longer preceding central Pacific warming state. However, all ENSO events during the period covered are preceded by LEDIV and DSEDIV anomalies in the central Pacific 6–9 months prior to the respective event peaks (see also the significant cross correlations in Figs. 3b,c). Thus, energy budget anomalies related to both warm and cold events propagate from west to east. This result is distinct from (but not necessarily contradictory to) that of McPhaden and Zhang (2009), who found east-to-west propagation of La Niña SST anomalies.

The total energy picture is different. Compared to LEDIV and DSEDIV, the TEDIV response to ENSO is, in terms of magnitude, generally much weaker, mainly because latent heating from anomalous precipitation is realized as DSE and thus does not alter total energy. TEDIV anomaly series show a dipole with maxima over the Indo-Pacific warm pool and central–eastern Pacific during ENSO peak phases. Positive TEDIV anomalies (mainly driven by anomalous F_S) over the central–eastern Pacific during warm ENSO phases correspond to the discharge phase, while negative anomalies over the central/eastern Pacific indicate the recharge phase. Thus, atmospheric TEDIV is in phase with equatorial oceanic warm water volume (i.e., the water above the thermocline within 5°S–5°N) discharge (see Meinen and McPhaden 2000). As already emphasized by MH12, strong compensation occurs between central and eastern Pacific and Indo-Pacific warm pool, leading to relatively weak TEDIV (and thus F_S) anomalies on the Pacific zonal average, which can reach 10 W m^{-2} during strong warm events (corresponding to an total energy export anomaly of $\approx$0.8 PW). For the full zonal average (360°), maximum total energy export anomalies reach 3–4 W m^{-2} (corresponding to $\approx$0.6 PW).

The transition phase however, which is clearly resolved in both LEDIV and DSEDIV (and also their second EOF and respective PC), while detectible in TEDIV, exhibits marginal variance (<9% in ERA-I). Thus, in the atmosphere, this phase of ENSO is mainly a change in circulation but the signal in total energy divergence is weak. The reason for this might be the decreasing surface wind speed around the date line because of easing trade winds, damping positive evaporation anomalies stemming from already increased SSTs in that region [as also speculated by Kumar and Hu (2012)]. This could explain the comparatively weak ocean–atmosphere coupling in terms of energy exchange during this phase. Hence, central Pacific warming events (El Niño Modoki

state; e.g., in 2002 or 2007), which resemble EOF-2 of LEDIV and DSEDIV, respectively, lead to very weak alteration of the total energy budget compared to canonical El Niños. In this context, the observed spatiotemporal coherence of energy budget anomalies suggests that El Niño Modoki is part of the overall evolutionary patterns of ENSO and represents a transition state between cold and warm ENSO phases. This is seen when all months of the year are considered together, and thus the annual cycle may also play a role. Hence, the fact that El Niño Modoki is depicted by a single EOF mode should not be overinterpreted.

In conclusion, the diagnostic methods presented herein are useful for monitoring ENSO and will be invaluable in validating climate models. The observed redistribution of energy during the ENSO cycle needs to be captured by climate models in order to realistically simulate global teleconnections. For instance, a realistic simulation of the zonal structure of LEDIV in response to ENSO (which in turn is dependent on realistic SST anomaly patterns) is necessary for a reasonable depiction of observed teleconnections such as ENSO-related droughts over Australia. Cross-correlation or EOF patterns, as presented in sections 3c and 3e, could serve as benchmarks when investigating energy budgets in climate models.

Moreover, it is planned to extend the current analysis retrospectively, as new reanalyses covering the pre-satellite era become available including the Twentieth Century Reanalysis (Compo et al. 2011) and the soon to be released Japanese Reanalysis 55 and ERA-Clim pilot reanalyses. We also expect that future coupled reanalyses that include interactions with the deep ocean will help to further improve the presented diagnostics.

REFERENCES

Alexander, M. A., N. C. Lau, and J. D. Scott, 2004: Broadening the atmospheric bridge paradigm: ENSO teleconnections to the tropical west Pacific-Indian Oceans over the seasonal cycle and to the North Pacific in summer. *Earth's Climate: The Ocean–Atmosphere Interaction, Geophys. Monogr.,* Vol. 147, Amer. Geophys. Union, 85–103.

Ashok, K., S. K. Behera, S. A. Rao, H. Weng, and T. Yamagata, 2007: El Niño Modoki and its possible teleconnection. *J. Geophys. Res.,* **112,** C11007, doi:10.1029/2006JC003798.

Chiodo, G., and L. Haimberger, 2010: Interannual changes in mass consistent energy budgets from ERA-Interim and

satellite data. *J. Geophys. Res.,* **115,** D02112, doi:10.1029/2009JD012049.

Clarke, A. J., 2008: *An Introduction to the Dynamics of El Niño and the Southern Oscillation.* Academic Press, 324 pp.

Compo, G. P., and Coauthors, 2011: The Twentieth Century Reanalysis Project. *Quart. J. Roy. Meteor. Soc.,* **137,** 1–28.

Cullather, R. I., and M. G. Bosilovich, 2012: The energy budget of the polar atmosphere in MERRA. *J. Climate, 25,* 5–24.

Dee, D. P., and S. Uppala, 2009: Variational bias correction of satellite radiance data in the ERA-Interim reanalysis. *Quart. J. Roy. Meteor. Soc., 135,* 1830–1841, doi:10.1002/qj.493.

——, and Coauthors, 2011: The ERA-Interim reanalysis: Configuration and performance of the data assimilation system. *Quart. J. Roy. Meteor. Soc., 137,* 553–597, doi:10.1002/qj.828.

Fasullo, J. T., and K. E. Trenberth, 2008a: The annual cycle of the energy budget. Part I: Global mean and land–ocean exchanges. *J. Climate, 21,* 2313–2325.

——, and ——, 2008b: The annual cycle of the energy budget. Part II: Meridional structures and poleward transports. *J. Climate, 21,* 2297–2312.

Hantel, M., and Coauthors, 2005: *Observed Global Climate.* Landolt Börnstein New Series, Vol. 6, Springer, 588 pp.

Huffman, G. J., R. F. Adler, D. T. Bolvin, and G. J. Gu, 2009: Improving the global precipitation record: GPCP version 2.1. *Geophys. Res. Lett., 36,* L17808, doi:10.1029/2009GL040000.

Jin, F. F., 1997: An equatorial ocean recharge paradigm for ENSO. Part I: Conceptual model. *J. Atmos. Sci., 54,* 811–829.

Klein, S. A., B. J. Soden, and N. C. Lau, 1999: Remote sea surface temperature variations during ENSO: Evidence for a tropical atmospheric bridge. *J. Climate, 12,* 917–932.

Kumar, A., and Z. Z. Hu, 2012: Uncertainty in the ocean-atmosphere feedbacks associated with ENSO in the reanalysis products. *Climate Dyn., 39,* 575–588.

Lorenz, E., 1967: *The Nature and Theory of the General Circulation of the Atmosphere.* WMO, 161 pp.

Mayer, M., and L. Haimberger, 2012: Poleward atmospheric energy transports and their variability as evaluated from ECMWF reanalysis data. *J. Climate, 25,* 734–752.

McPhaden, M. J., 1999: Genesis and evolution of the 1997–98 El Niño. *Science, 283,* 950–954, doi:10.1126/science.283.5404.950.

——, and X. Zhang, 2009: Asymmetry in zonal phase propagation of ENSO sea surface temperature anomalies. *Geophys. Res. Lett., 36,* L13703, doi:10.1029/2009GL038774.

Meinen, C. S., and M. J. McPhaden, 2000: Observations of warm water volume changes in the equatorial Pacific and their relationship to El Niño and La Niña. *J. Climate, 13,* 3551–3559.

North, G. R., T. L. Bell, R. F. Cahalan, and F. J. Moeng, 1982: Sampling errors in the estimation of empirical orthogonal functions. *Mon. Wea. Rev., 110,* 699–706.

Okumura, Y. M., and C. Deser, 2010: Asymmetry in the duration of El Niño and La Niña. *J. Climate, 23,* 5826–5843.

Peixoto, J. P., and A. H. Oort, 1992: *Physics of Climate.* American Institute of Physics, 520 pp.

Rienecker, M. M., and Coauthors, 2011: MERRA: NASA's Modern-Era Retrospective Analysis for Research and Applications. *J. Climate, 24,* 3624–3648.

Saha, S., and Coauthors, 2010: The NCEP Climate Forecast System Reanalysis. *Bull. Amer. Meteor. Soc., 91,* 1015–1057.

Sarachik, E. S., and M. A. Cane, 2010: *The El Niño–Southern Oscillation Phenomenon.* Cambridge University Press, 384 pp.

Trenberth, K. E., and D. P. Stepaniak, 2001: Indices of El Niño evolution. *J. Climate, 14,* 1697–1701.

——, and ——, 2003a: Covariability of components of poleward atmospheric energy transports on seasonal and interannual timescales. *J. Climate, 16,* 3691–3705.

——, and ——, 2003b: Seamless poleward atmospheric energy transports and implications for the Hadley circulation. *J. Climate, 16,* 3706–3722.

——, and L. Smith, 2006: The vertical structure of temperature in the tropics: Different flavors of El Niño. *J. Climate, 19,* 4956–4973.

——, and ——, 2008: Atmospheric energy budgets in the Japanese reanalysis: Evaluation and variability. *J. Meteor. Soc. Japan, 86,* 579–592, doi:10.2151/jmsj.86.579.

——, and J. T. Fasullo, 2012: Climate extremes and climate change: The Russian heat wave and other climate extremes of 2010. *J. Geophys. Res., 117,* D17103, doi:10.1029/2012JD018020.

——, J. Caron, D. Stepaniak, and S. Worley, 2002a: Evolution of El Niño-Southern Oscillation and global atmospheric surface temperatures. *J. Geophys. Res., 107* (D8), doi:10.1029/2000JD000298.

——, D. P. Stepaniak, and J. M. Caron, 2002b: Interannual variations in the atmospheric heat budget. *J. Geophys. Res., 107* (D8), doi:10.1029/2000JD000297.

——, and Coauthors, 2007: Observations: Surface and atmospheric climate change. *Climate Change 2007: The Physical Science Basis,* S. Solomon et al., Eds., Cambridge University Press, 235–336.

——, J. T. Fasullo, and J. Kiehl, 2009: Earth's global energy budget. *Bull. Amer. Meteor. Soc., 90,* 311–323.

——, ——, C. O'Dell, and T. Wong, 2010: Relationships between tropical sea surface temperature and top-of-atmosphere radiation. *Geophys. Res. Lett., 37,* L03702, doi:10.1029/2009GL042314.

——, J. Fasullo, and J. Mackaro, 2011: Atmospheric moisture transports from ocean to land and global energy flows in reanalyses. *J. Climate, 24,* 4907–4924.

Wallace, J. M., and J. Shukla, 1983: Numerical simulation of the atmospheric response to equatorial Pacific sea surface temperature anomalies. *J. Atmos. Sci., 40,* 1613–1630.

Zebiak, S. E., and M. A. Cane, 1987: A model El Niño–Southern Oscillation. *Mon. Wea. Rev., 115,* 2262–2278.

[1]   **Supplemental Material**

[2] **The Response of Tropical Atmospheric Energy Budgets to ENSO**

[3]   MICHAEL MAYER[1]*   KEVIN E. TRENBERTH[2]

                 LEOPOLD HAIMBERGER[1]   JOHN T. FASULLO[2]

            [1]*Department of Meteorology and Geophysics, University of Vienna, Vienna, Austria*

               [2]*National Center for Atmospheric Research, Boulder, Colorado*

        Corresponding author address: Michael Mayer, Department of Meteorology and Geophysics, University

of Vienna, UZA II, Althanstr. 14, 1090 Vienna

E-mail: mima@univie.ac.at

1

a. Mass flux correction for MERRA energy divergences

5   Mass consistency is a crucial prerequisite for energy budget evaluations. The basic idea

6   behind mass flux correction is to calculate the difference between the field of instantaneous

7   vertically integrated mass flux divergence from the analyzed state ($\langle M_{DIV}\rangle$, which is implicitly

8   used for computation of energy divergences) and an indirect estimate of this field (employing

9   the analyzed mass tendency, M_{TEND}, and precipitation minus evaporation, P-E). The indirect

10   estimate represents a much smoother and more realistic estimate of the mass flux divergence.

11   This difference is then used to adjust the directly calculated energy divergence. According to

12   Mayer and Haimberger (2012), the corrected (superscript c) field of the divergence of latent

13   heat transport (LEDIV) is given by

$$\text{LEDIV}^c = \text{LEDIV} - \widehat{\text{LE}} \cdot (\langle M_{DIV}\rangle + \text{P-E} + M_{TEND}),\tag{1}$$

14   where $\widehat{\text{LE}}$ denotes the vertically averaged latent energy of the column. Using MERRA

15   fields stored at the NASA GES DISC and the phase transition energy of vaporization L, eq.

16   1 reads as follows:

$$\text{LEDIV}^c = \text{-DQVDT\_DYN} - \frac{\text{L} \cdot \text{TQV} \cdot (\text{DQVDT\_ANA+DQVDT\_PHY-DMDT\_ANA})}{\text{MASS}}.\tag{2}$$

17   Fields used in eq. 2 are monthly mean vertical integrals of water vapor tendency from

18   dynamics (DQVDT_DYN), analyzed specific humidity (TQV), analysis increments for wa-

19   ter vapor tendency (DQVDT_ANA), water vapor tendency from physics (DQVDT_PHY),

20   analysis increments for mass tendency (DMDT_ANA) and atmospheric mass (MASS). The

1

MERRA file specification document with a detailed description of all archived fields is located at http://disc.sci.gsfc.nasa.gov/mdisc/documentation. The error introduced by using monthly averages instead of fields with full time resolution in eq. 2 is negligible.

b. *Impact of splitting climatologies*

Temporal inhomogeneities existing in all employed reanalyses can mask some of the signals in the tropical strip. The effect of inhomogeneities has been reduced by splitting climatologies into three periods. Here we show the effect of splitting the background climatologies. For ERA-I, discontinuities were detected by a simple algorithm, which minimizes the RMS value of anomalous moisture analysis increments in the tropical strip by varying the temporal fragmentation of the background climatologies (the lower the RMS value, the higher the degree of temporal homogeneity of the field) for a given amount of breakpoints. For MERRA and CFSR, we use the major breakpoints detected in Trenberth et al. (2011).

Longitude-time Hovmöller plots of tropical (20°N-20°S) LEDIV anomalies from ERA-I, MERRA and CFSR are presented in Figs. 1, 2 and 3. Plots in the left column (1a, 2a, 3a) employ one background climatology, while the respective plots in the right column use three split background climatologies. Note the large artifacts, e.g. around 80°W in Fig. 1a, which are effectively removed when splitting the climatologies at the largest discontinuities.

c. *Mean annual cycle of tropical energy divergence*

The mean annual cycle of tropical average (20°N-20°S) TEDIV (a), LEDIV (b) and DSEDIV (c) as well as tropical average standard deviations of the respective fields (d) are

2

⁴¹ presented in Fig. 4. As already described in the main text, strongest total energy export

⁴² occurs in January and highest variability of tropical energy divergences occurs during DJF,

⁴³ indicating the high variability associated with ENSO.

⁴⁴ *d. Variability among composited events*

⁴⁵   In section 3d of the main text we present composites of several energy budget-relevant

⁴⁶ fields for three strong El Niño events (1982/83, 1991/92, 1997/98). In Fig. 5 LEDIV anomaly

⁴⁷ series from ERA-I are shown for the five strongest warm events (1982/83, 1986/87, 1991/92,

⁴⁸ 1997/98, 2009/10) to give an impression of the variability among these events. The 1991/92

⁴⁹ El Niño is preceded by a much longer central Pacific warming state than the other events

⁵⁰ and it is not directly succeeded by a La Niña event (which is the case for the others). Fig. 5b

⁵¹ shows the double peak of the 1986/87 event. However, the composite of the five warm events

⁵² shows the West-East propagation of ENSO-related anomalies as discussed in the main text.

⁵³ The structures at positive lags are more significant than those at negative lags, reflecting

⁵⁴ the well-known tendency of warm events to be directly succeeded by cold events.

3

REFERENCES

Mayer, M. and L. Haimberger, 2012: Poleward Atmospheric Energy Transports and Their Variability as Evaluated from ECMWF Reanalysis Data. *J. Climate*, **25 (2)**, 734–752, doi:10.1175/JCLI-D-11-00202.1.

Trenberth, K., J. Fasullo, and J. Mackaro, 2011: Atmospheric moisture transports from ocean to land and global energy flows in reanalyses. *J. Climate*, **24 (January)**, 4907–4924, doi:10.1175/2011JCLI4171.1.

4

List of Figures

5

FIG. 1. Smoothed monthly anomalies of tropical LEDIV from ERA-I, using one background climatology 1979-2011 (a), using three background climatologies 1979-1991, 1992-2002, 2003-2011 (b).

6
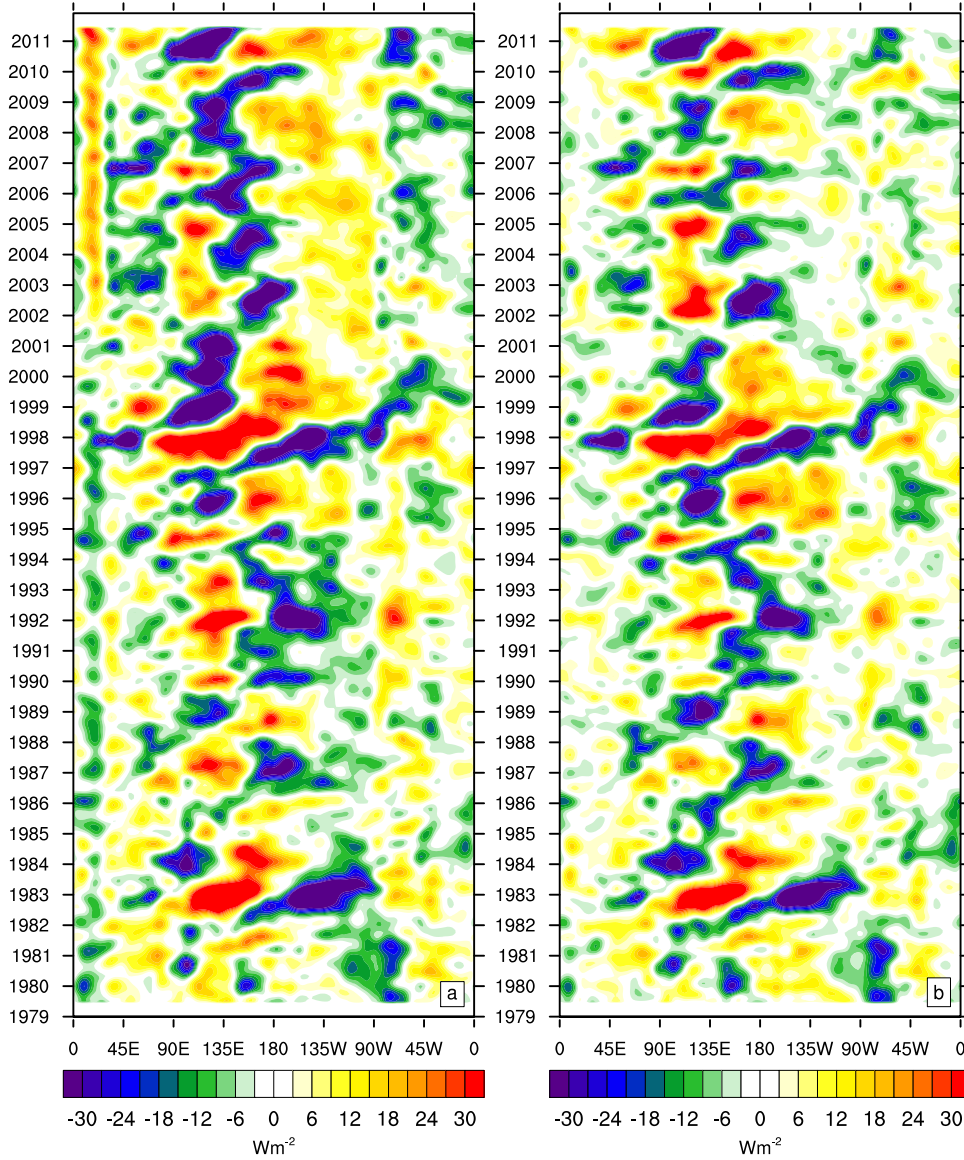
FIG. 2. Smoothed monthly anomalies of tropical LEDIV from MERRA, using one background climatology 1979-2011 (a), using three background climatologies 1979-1998, 1999-2002, 2003-2011 (b).

7
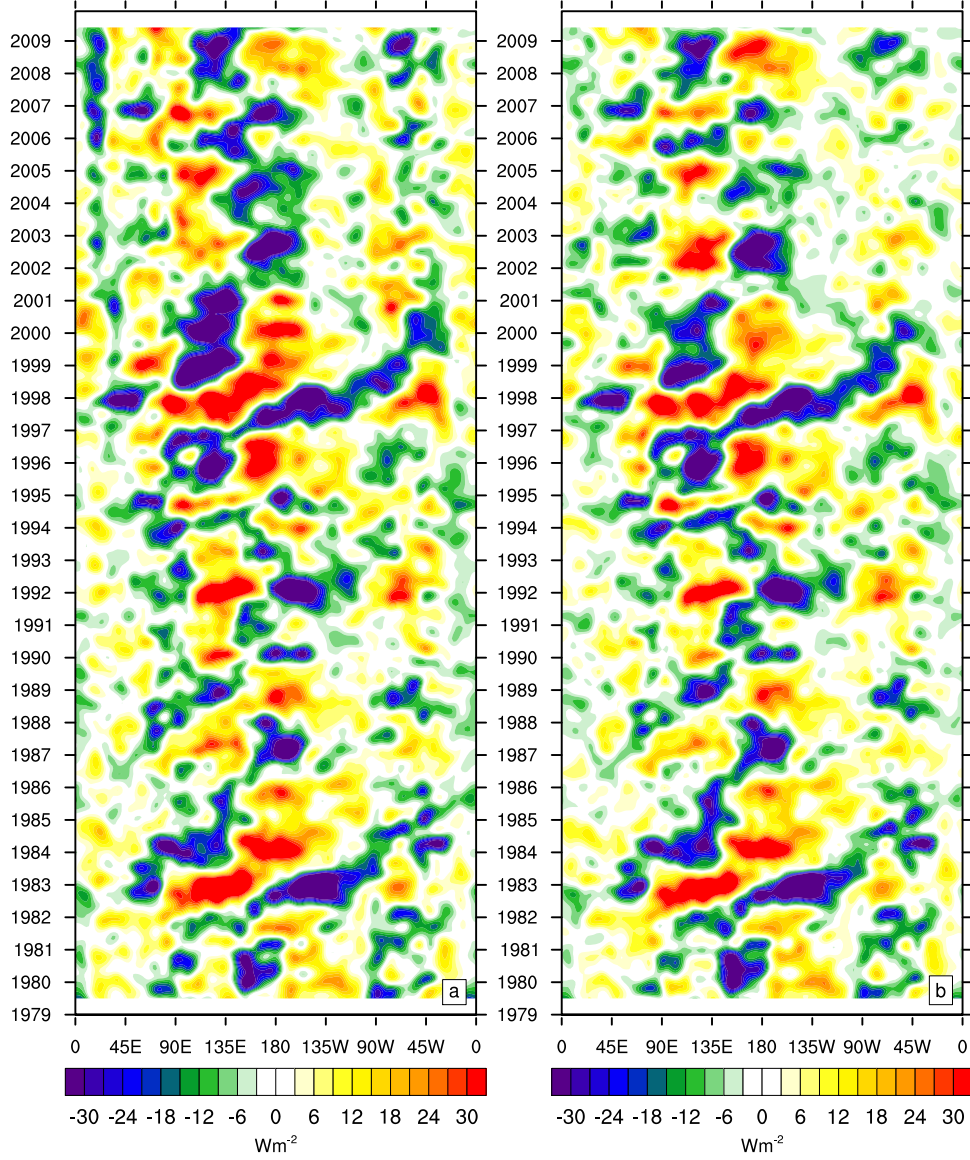
FIG. 3. Smoothed monthly anomalies of tropical LEDIV from CFSR, using one background climatology 1979-2009 (a), using three background climatologies 1979-1998, 1999-2002, 2003-2009 (b).

8
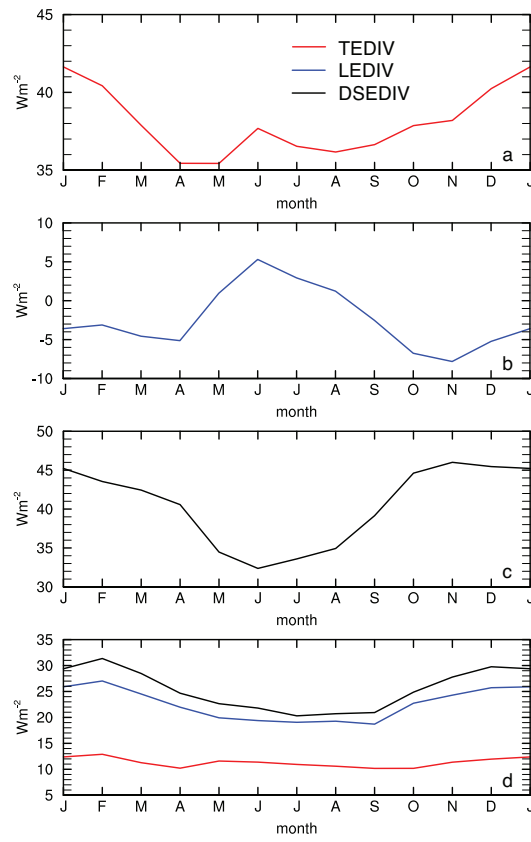
FIG. 4. Mean annual cycle of TEDIV (a), LEDIV (b), DSEDIV (c) and respective mean annual cycle of standard deviations (d) from ERA-I averaged over the tropical belt (20°N-20°S, 360°).

9
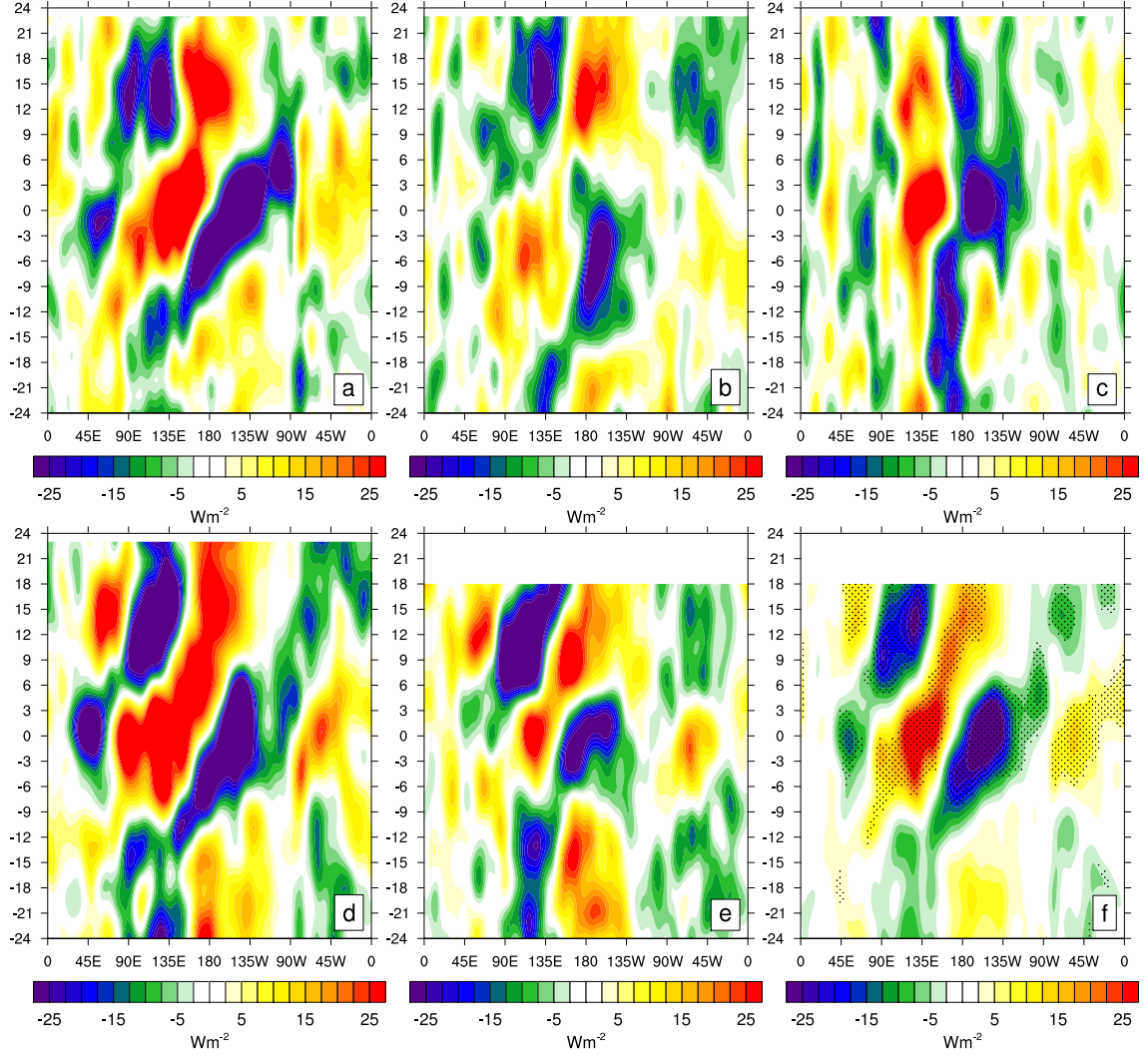
FIG. 5. As in Fig. 4a in the main text, but for single El Niño events 1982/83 (a),1986/87 (b), 1991/92 (c), 1997/98 (d) and 2009/10 (e; no ERA-I data after lag 18); a composite of all five events is presented in (f). Stippling denotes anomalies with significance >90%.

10

5   Combined evaluation of oceanic and atmospheric energy budgets

This article explores the coupled energy budget of tropical atmosphere and ocean on a basin-averaged scale. Results show a novel signature of OHC redistribution between tropical ocean basins in association with ENSO, quantitatively consistent with variability of atmospheric energy transports in the respective ocean basins.

My contributions to this work were large parts of the design of the study, interpretation of the results (equal share with the co-authors) and accomplishment of all required computations. The inclusion of the ocean energy budget to this study required development of a method to compute OHC and its tendency, which is not straight forward because of spatial and temporal variations of density and also heat capacity of sea water due to temperature and salinity variations. The employed computation method and justification of applied simplifications is described in detail in section 2.3. Moreover, I prepared all visualizations required for this publication and wrote the paper.

Mayer, M., Haimberger, L., and Balmaseda, M. A., 2014: *On the energy exchange between tropical ocean basins related to ENSO*. Journal of Climate, in press.

1   **On the energy exchange between tropical ocean basins related to ENSO**
2
3
4   Michael Mayer[1, *]
5
6   Leopold Haimberger[1]
7
8   Magdalena A. Balmaseda[2]
9
10
11   [1]Department of Meteorology and Geophysics, University of Vienna, Vienna, Austria
12   [2]European Centre for Medium-Range Weather Forecasts, Reading, United Kingdom
13
14
15
16   [*] Corresponding author address:
17   Althanstrasse 14
18   1090 Vienna
19   Austria
20   mima@univie.ac.at
21
22
23
24
25
26
27
28
29
30
31
32
33
34
35
36
37
38
39
40
41
42
43
44
45
46

1

47   **Abstract**

48   **Vast amounts of energy are exchanged between ocean, atmosphere, and space in association**

49   **with El Niño-Southern Oscillation (ENSO). This study examines energy budgets of all**

50   **tropical (30S-30N) ocean basins and the atmosphere separately using different largely**

51   **independent oceanic and atmospheric reanalyses to depict anomalous energy flows associated**

52   **with ENSO in a consistent framework.**

53   **It is found that variability of area-averaged tropical Pacific ocean heat content (OHC) to a**

54   **large extent is modulated by energy flow through the ocean surface. While redistribution of**

55   **OHC within the tropical Pacific is an integral part of ENSO dynamics, variability of ocean**

56   **heat transport out of the tropical Pacific region is found to be mostly small. Noteworthy**

57   **contributions arises from the Indonesian Throughflow (ITF), which is anti-correlated with**

58   **ENSO at a few months lag, and from anomalous oceanic poleward heat export during the La**

59   **Niñas in 1999 and 2008.**

60   **Regression analysis reveals that atmospheric energy transport and radiation at top-of-**

61   **atmosphere (Rad_{TOA}) almost perfectly balance the OHC changes and ITF variability**

62   **associated with ENSO. Only a small fraction of El Niño-related heat lost by the Pacific Ocean**

63   **through anomalous air-sea fluxes is radiated to space immediately, whereas the major part of**

64   **the energy is transported away by the atmosphere. Ample changes in tropical atmospheric**

65   **circulation lead to enhanced surface fluxes and consequently to an increase of tropical**

66   **Atlantic and Indian OHC that almost fully compensates tropical Pacific OHC loss. This**

67   **signature of energy redistribution is robust across the employed datasets for all three**

68   **tropical ocean basins and explains the small ENSO signal in global mean Rad_{TOA}.**

69

2

70   **1. Introduction**

71   The primary mode of global climate variability, El Niño-Southern Oscillation (ENSO), modulates

72   the energy budget of both the ocean and the atmosphere in various ways. Pacific OHC is

73   redistributed within the basin (e.g., Roemmich and Gilson 2011) and altered via anomalous surface

74   energy exchanges (e.g., Trenberth et al. 2002, Sun 2000, or Lengaigne et al. 2012). In the

75   atmosphere, the Pacific Hadley cell (Oort and Yienger 1996) and associated energy export from

76   this region (e.g., Trenberth et al. 2002, Mayer and Haimberger 2012, or Mayer et al. 2013)

77   strengthens (weakens) during warm (cold) ENSO events.

78   The Hadley cells over the Indo-Pacific Warm Pool and the Atlantic, linked to the eastern tropical

79   Pacific through anomalous atmospheric zonal overturning circulation (Walker cell), show opposite

80   behavior compared to the Pacific Hadley cell (Klein et al. 1999). Associated with these remote

81   circulation changes, teleconnection patterns have been identified in various meteorological fields,

82   including sea surface temperature (SST, see Klein et al. 1999 or Enfield and Mayer 1997) and

83   surface heat flux (see Lohmann and Latif 2007 or Grist et al. 2010) in the tropical Atlantic and

84   Indian Ocean basins.

85   Although changes of the ocean and atmosphere in association with ENSO are well documented

86   (studies cited herein and many others), a quantitative assessment of pathways of energy through

87   the ENSO cycle including both the atmosphere and the ocean is lacking (Trenberth and Fasullo

88   2012). The limitations of ocean data are one reason for this circumstance. While investigation of

89   atmospheric energy budget variability associated with ENSO has made substantial advances due to

90   the availability of global atmospheric reanalyses, ocean data sets for a long time have been much

91   more limited in spatial and temporal coverage [e.g. data from the TOGA (Tropical Ocean – Global

92   Atmosphere) - TAO (Tropical Atmosphere Ocean project) array], and hence most observation

3

93   based quantitative studies were focused on the equatorial Pacific (e.g., Meinen and McPhaden

94   2000, Hasegawa and Hanawa 2003, or Clarke et al. 2007).

95   The advent of new ocean reanalyses in recent years and advances in ocean data coverage due to the

96   introduction of Argo (a global array of currently more than 3500 temperature and salinity profiling

97   floats) in the 2000s should facilitate this attempt but data quality is a remaining issue. Balmaseda

98   et al. (2013) have shown that Ocean Reanalysis System 4 (ORAS4, Balmaseda et al. 2012)

99   consistently reflects the impact of major volcanic eruptions and earth's energy imbalance in global

100   accumulated OHC. However, results of Loeb et al. (2012) and Trenberth et al. (2014) suggest that

101   current ocean data sets practically fail to satisfy global constraints such as replication of anomalous

102   Rad_{TOA} measured from satellites in observed OHC variability. Uncertainty and resulting noise in

103   ocean datasets is still too large to resolve small global mean anomalies of OHC tendencies

104   (OHCT) on the order of ±1 Wm^{-2} on interannual timescales. However, Loeb et al. 2012 found

105   ENSO signals in global mean net radiation at TOA on the order of $\pm0.5Wm^{-2}$ (corresponding to

106   $\pm0.25PW$).

107   Here we employ three ocean reanalyses with different data assimilation approaches [ORAS4, Had

108   EN3 v2a (HEN3, Ingleby and Huddleston 2007), and Ensemble Coupled Data Assimilation system

109   (ECDA, Zhang et al. 2007)] and two third generation atmospheric reanalyses [ERA-Interim (ERA-

110   I, Dee et al. 2011) and Modern Era Retrospective-Analysis for Research and Applications

111   (MERRA, Rienecker et al. 2011)] from 1979-2012 to explore the energy budgets of the three

112   tropical ocean basins and the tropical atmosphere in one consistent framework. Using these

113   datasets and state of the art budget methods we will show that on the scale of individual basins the

114   signal-to-noise ratio in OHC data is sufficiently high to obtain robust signals of anomalous energy

115   exchanges and transports within as well as between ocean basins in association with ENSO.

4

116   Specifically, we will show that OHC changes in the tropical Pacific associated with ENSO are

117   much larger than the response of Rad_{TOA} to ENSO. This apparent discrepancy can be explained by

118   compensating OHC responses to ENSO in other tropical ocean basins that are of opposite sign

119   compared to the tropical Pacific OHC response to ENSO. Atmospheric circulation and associated

120   surface flux changes are responsible for these apparent energy exchanges across tropical ocean

121   basins.

122

123

124   **2. Data and methods**

125   We investigate the variability of the energy budgets of atmosphere and ocean in a vertically integrated

126   framework.

127   In an atmospheric column, net energy flux through the atmospheric lower boundary (F_S, positive

128   downward) is balanced by the local tendency of total atmospheric energy (AET), the divergence of

129   horizontal atmospheric energy (more precisely: moist static plus kinetic energy) transport out of the

130   column (DIVFA), and net radiation at TOA (throughout this article this means the sum of all radiation

131   components):

132

133    $$F_S = -AET - DIVFA + Rad_{TOA} \quad (1)$$

134

135   We compute F_S as a residual from the right side of Eq. (1). The energy tendency AET is calculated

136   from analyzed ERA-I fields, although the variability of AET in the tropics is small and almost

137   negligible on interannual timescales. The divergence of atmospheric energy transport (DIVFA) is

138   computed with the direct method from analyzed atmospheric state quantities as described in Mayer and

5

139   Haimberger (2012) employing data from ERA-I and MERRA. Radiation at TOA is known to be biased

140   in ERA-I forecasts (see e.g., Berrisford et al. 2011), but Mayer and Haimberger 2012 showed that

141   monthly anomalies agree well with independent satellite data from Clouds and Earth's Radiant Energy

142   System (CERES, Wielicki et al. 1996). Hence, we mainly employ Rad_{TOA} from ERA-I because of the

143   much longer period covered, but all computations are also performed with CERES data to confirm the

144   results at least for the shorter commonly covered period (here 2000/03 – 2012/02). We also tested

145   Rad_{TOA} from MERRA for 1979-2012, but it was much less homogeneous in time and thus excluded

146   from this study.

147   In an oceanic column, extending from the sea surface to the ocean bottom, net surface flux (F_S) is

148   balanced by the local tendency of ocean heat (more precisely: enthalpy) content (OHCT) and the

149   divergence of horizontal ocean heat (more precisely: enthalpy) transport (DIVFO) out of the column

150   (variability of other forms of energy in the ocean is negligible in this context):

151

152   $$F_S = OHCT + DIVFO \quad (2)$$

153

154   For the evaluation of OHCT in Eq. (2) we use three state of the art oceanic datasets covering 1979-

155   2012. ORAS4 employs an ocean model for data assimilation and ERA-I surface fluxes as boundary

156   conditions. As we here aim to obtain independent estimates of atmospheric-oceanic energy exchanges,

157   we additionally employ HEN3 and ECDA. The datasets partly differ in input data, but also in their data

158   assimilation approaches. HEN3 represents an objective analysis purely from in-situ data and hence is

159   fully independent of atmospheric data, and the ECDA dataset represents a coupled data assimilation

160   approach using the fully coupled climate model CM2.1.

161   The monthly mean ocean heat content tendency (OHCT) in Eq. (2) would ideally be obtained from the

6

162   difference of OHC snap shots at 00UTC on the first day of two consecutive months to be perfectly

163   consistent with the monthly averages of the other terms in Eqs. (1) and (2). However, generally no

164   ocean temperature snap shots are provided with ocean datasets and thus OHCT is obtained from

165   centered differences of monthly mean values of ocean heat content (OHC). On the time scales

166   considered here, the introduced error is small. Ocean heat content is computed as

167

168
$$OHC = c_p \rho_0 \int_0^{depth} \theta(z)\,dz \quad (3)$$

169

170   with the heat capacity of sea water $c_p = 3990\,\mathrm{Jkg^{-1}K^{-1}}$, the density of sea water $\rho_0 = 1026\,\mathrm{kgm^{-3}}$ [both

171   values are not independent of temperature, but their product tends to be (Trenberth and Fasullo 2008)]

172   and ocean potential temperature θ. The lower integration bound is the sea surface height above a

173   reference level. Tests have shown that variations of sea surface height on interannual time scales are

174   almost entirely due to steric effects and thus can be neglected when using constant density. This is a

175   common approximation in physical oceanography [see, e.g. Trenberth and Fasullo 2008]. The upper

176   integration bound (*depth*) ideally represents the ocean bottom.

177   It would certainly be perfectly consistent to integrate OHC to the bottom of the ocean everywhere, but

178   in general data quality decreases with depth as the number of measurements decreases with depth.

179   Hence, integration depth is a compromise between data quality and physical consistency. We tested

180   several values for the integration depth (300m, 400m, 700m, 2000m, and the ocean bottom) and the

181   agreement among the datasets in terms of variability was best for a depth of 300m. Moreover, the

182   satisfaction of global constraints such as the replication of Rad_{TOA} anomalies in OHCT was best, albeit

183   certainly not perfect, for an integration depth of 300m. As will be shown below, for depths greater than

7

184   300m the increase of noise in the data outweighs the increase in the signal. This is especially true for

185   the linear relation between OHC and ENSO, which we will focus on in the following sections.

186   Regarding DIVFO, the main focus of this paper is on ocean heat exports out of the three tropical ocean

187   basins. We can estimate these exports, i.e. area-integrated DIVFO, from the directly computed ocean

188   heat transports across the lateral boundaries of the basins. These are available from ORAS4 and we

189   employ full-depth ocean heat transport across selected ocean cross-sections: Pacific (1979-2012) and

190   Atlantic (1979-2009) ocean heat transport at 30N and 30S, Indian Ocean heat transport across 30S

191   (1979-2009) and heat transport by the Indonesian Throughflow (1979-2012). At least at the considered

192   cross-sections, ocean heat transport variability below 300m is small, and especially below 700m it is

193   very close to zero and in contrast to OHCT the noise does not increase with depth (see S1).

194   An alternative way to evaluate DIVFO is to compute it indirectly from F_S and OHCT (as described in

195   Trenberth and Fasullo 2008). In our case, the indirect estimate yields six different DIVFO estimates

196   (every possible combination of employed OHC and F_S data). The major disadvantage of this method is

197   the accumulation of uncertainties from all employed fields (DIVFA, Rad_{TOA}, AET and OHCT) in

198   DIVFO. As a consequence the global mean value of DIVFO and especially its anomalies are not equal

199   zero, which should be the case when neglecting contributions from river discharge and calving glaciers.

200   Moreover, Eq. (2) holds only if OHCT is integrated to the ocean bottom. If OHCT is integrated only to

201   a depth of 300m (to avoid noise from below 300m), a heat flux term across a depth of 300m has to be

202   added in Eq. (2). Since this flux is not known it contributes to the uncertainty of the indirect DIVFO

203   estimate. Tests showed that indirectly estimated DIVFO is not distinguishable from noise on the scale

204   of tropical ocean basins (30N-30S), independent of integration depth (see S2), but the signal-to-noise

205   ratio is much better when considering smaller regions with no spatially compensating anomaly

206   structures (e.g., equatorial Pacific). Overall, we found the direct approach to yield better results on a

8

207   basin-integrated scale, where anomaly signals are generally weak due to compensating processes

208   within the respective basins.

209   All anomaly fields and series shown in the present article represent monthly anomalies with the annual

210   cycle removed and are 13-point filtered in time (Trenberth et al. 2007). Fields have been detrended

211   before correlation and regression analysis.

212

213

214   **3. Results**

215   **a) Tropical Pacific and Atlantic budget variability**

216   We first consider time series of budget relevant terms over the Pacific and Atlantic oceans. Over the

217   Pacific (Fig. 1a), largest variability is found from DIVFA with stronger (weaker) atmospheric energy

218   export and OHCT with heat loss (gain) during warm (cold) ENSO phases. This behavior is most

219   conspicuous during the strong El Niños in 1982/83, 1987, 1997/98 and 2009/10. Compared to DIVFA,

220   the time series of OHCT exhibits considerable noise, but the ENSO-related heat discharge/recharge is

221   clearly visible. Radiation at TOA over the tropical Pacific also exhibits noticeable variability associated

222   with ENSO, with weaker (stronger) net energy input during El Niño (La Niña), which is a result of the

223   strong ENSO-related anomalies of outgoing longwave radiation in the subtropics (Trenberth et al.

224   2010). Comparison of Rad_{TOA} from ERA-I and independent CERES data for the limited period of the

225   satellite data set shows very good agreement between the two series (Fig. 1a, correlation coefficient

226   r=0.95), suggesting Rad_{TOA} anomalies from ERA-I to be reliable also prior to 2000. Significant

227   correlation is found between DIVFA, OHCT and Rad_{TOA} and the Niño 3.4 index [N34, anomaly index

228   (in units K) of SSTs area-averaged over 170W-120W, 5S-5N, see Fig. S3a].

229   Variance of the Pacific oceanic heat export, i.e. the sum of ITF heat transport and poleward ocean heat

9

230   export (here defined as difference of northward transport across 30N and 30S), is generally small.

231   However, the ITF heat transport shows a slight weakening following El Niño events, in accordance

232   with England and Huang (2005), and it is significantly correlated with N34 at six months lag (r=-0.65).

233   Poleward ocean heat export shows no significant correlation with ENSO (r=0.22), but nevertheless

234   there can be seen some variability, for example positive anomalies during the 1999 and 2008 La Niña

235   events.

236   Altogether, this suggests that Pacific ocean heat loss/gain associated with ENSO is mainly balanced by

237   atmospheric energy export and also Rad_{TOA}. Ocean heat transport apparently plays a minor role in

238   modulating basin-integrated OHC, with the strongest contribution from the ITF.

239   The behavior of DIVFA and OHCT in response to ENSO over the Atlantic Ocean is opposite compared

240   to the Pacific (Fig. 1b), which is a result of the opposite response of the Atlantic Hadley cell to ENSO

241   compared to the Pacific Hadley cell (see Klein et al. 1999). Atmospheric energy export is weaker

242   (stronger) and the ocean gains (loses) heat during El Niño (La Niña). Both DIVFA and OHCT over the

243   Atlantic are significantly correlated with N34 (Fig. S3b). Atlantic Ocean heat export varies weakly, and

244   the correlation with N34 is very low (r=-0.20). Radiation at TOA from ERA-I also exhibits very small

245   anomalies, in agreement with CERES. As for the Pacific, this suggests a balance between the

246   divergence of atmospheric energy transport and Atlantic OHC. A quantitative assessment of the

247   qualitative findings in this section will be given in sections 3d and 3e.

248   Despite the good qualitative agreement of the curves in Figs. 1a, b it is noted that the anomaly budget is

249   generally not perfectly closed, i.e. the sum of the atmospheric and oceanic anomalies do not exactly

250   add up to zero in the respective basins as would be required from the budget Eqs. (1) and (2) (e.g. after

251   the eruption of Mt. Pinatubo). One reason for the observed discrepancies between atmospheric and

252   oceanic budget anomalies is the absence of signals from major volcanic eruptions El Chichón (1982)

10

253   and Mt. Pinatubo (1991) in Rad_{TOA} from ERA-I because evolution of volcanic aerosols is not included

254   in the reanalysis (Dee et al. 2011), while ORAS4 clearly shows the impacts of these eruptions (see Fig.

255   1a or also Trenberth et al. 2014). In contrast to Rad_{TOA} from ERA-I, analyzed atmospheric fields in

256   ERA-I such as stratospheric temperature do show the impact of volcanic eruptions (Simmons et al.

257   2013), which necessarily introduces inconsistencies between Rad_{TOA} and other atmospheric and

258   oceanic fields. However, results in the following sections will show that these imbalances are

259   uncorrelated with ENSO.

260

261

262   **b) Regression analysis**

263   To explore the linear relationship between energy budget terms with ENSO more rigorously, we

264   consider local regression coefficients of DIVFA, F_S, OHCT and sea surface temperature with N34 at

265   zero lag, presented in Figs. 2a-d, respectively. First we focus on the tropical Pacific energy budget

266   variability with its strong ENSO imprint. Regression fields of DIVFA and F_S both show anomalies of

267   opposite sign over the western and eastern Pacific, respectively (see also Mayer et al. 2013). Note the

268   high structural and quantitative agreement of the two fields indicating their tight relationship, i.e.

269   anomalous atmospheric energy transports are largely driven by surface fluxes. Compared to F_S,

270   regressed Pacific OHCT exhibits different structures, which represent the signature of ocean heat

271   redistribution within the ocean (deepening thermocline and hence increase of ocean heat content in the

272   East Pacific in association with El Niño and vice versa for La Niña), a necessary prerequisite for

273   increased interaction of the ocean with the atmosphere via SST (Roemmich and Gilson 2011).

274   Additionally, negative OHCT regression coefficients much stronger than the surface flux coefficients

11

275 can be found along the equator at all Pacific longitudes, indicative of OHC changes due to Sverdrup

276 transports in association with El Niño/La Niña (Jin 1997). This aspect will be discussed in section 3c.

277 Scatter plots of N34 versus tropical Pacific DIVFA anomalies from ERA-Interim and OHCT anomalies

278 from ORAS4 are presented in Figs. 2e and f, respectively. They confirm the findings from Fig. 1a, i.e.

279 the regression lines show similar slopes but of opposite sign suggesting that ocean heat feeds the

280 atmospheric energy transport anomalies.

281 Tropical Atlantic local regression coefficients (Figs. 2a-d) are more uniform than those over the

282 Pacific. Uniformly negative coefficients are found for DIVFA, which is a result of a negative

283 correlation between Atlantic Hadley cell strength and ENSO (Wang 2005). As in the Pacific, net

284 surface flux regression coefficients are again very similar to those of DIVFA (but opposite sign). Ocean

285 heat content tendency shows moderate positive coefficients nearly everywhere in the tropical Atlantic,

286 consistent with the surface flux regression field (Fig. 2b), the well-known Atlantic SST maximum 5

287 months after El Niño (Enfield and Mayer 1997), and with Lohmann and Latif (2007) who found that

288 El-Niño-related Atlantic SST warming occurs due to surface fluxes rather than ocean dynamics. Scatter

289 plots of area-averaged tropical Atlantic (30S-30N) DIVFA and OHCT versus N34 (Figs. 2g, h) again

290 confirm findings from Fig. 1b, namely negative (positive) DIVFA and positive (negative) OHCT

291 anomalies in association with warm (cold) ENSO states.

292 Anomalous divergent atmospheric energy transports from the Eastern Pacific to the Indo-Pacific Warm

293 Pool and the Atlantic, represented by the vectors in Fig. 2a, indicate the anomalous energy transport by

294 the anomalous Walker cell, suggesting an energy exchange between the tropical Pacific and Atlantic

295 oceans via total energy transport within the atmosphere. This picture will be corroborated in section 3d.

296

297

12

298   **c) Budget of the equatorial Pacific**

299   So far we have not considered estimates of DIVFO, but these are potentially as large as the other terms.

300   As already found from Figs. 2a-c, structures of locally regressed OHCT are much stronger than those

301   of F_S and DIVFA, which must be due to DIVFO. To demonstrate the dominance of ocean heat

302   transports along the equatorial Pacific compared to atmospheric transports, we present regression

303   coefficients of Rad_{TOA}, DIVFA and OHCT from different datasets with N34 at different lags in Fig. 3.

304   Confidence intervals are estimated from the residual sum of squares, taking autocorrelation into

305   account (following Oort and Yienger 1996). Atmospheric energy export is in phase with N34 and

306   responds with $0.13\pm0.02PWK^{-1}$ to ENSO. The Rad_{TOA} response is negligible. The ensemble mean

307   ocean heat content tendency response shows much stronger values of opposite sign ($-0.49\pm0.10PWK^{-1}$

308   at lag 3). The difference between DIVFA and OHCT response (on the order of $0.36PWK^{-1}$) indicates

309   that OHC variations along the equator in association with ENSO must be mainly balanced by ocean

310   heat transport, while smaller amounts of energy are exchanged at the surface. This is consistent with

311   the recharge oscillator concept by Jin (1997) which predicts that equatorial OHC anomalies are

312   dominated by anomalous Sverdrup transports. Westerly wind anomalies responsible for these transports

313   are strongest during the ENSO-related SST peak (Clarke et al. 2007). Hence, during peak ENSO (peak

314   of SST anomalies) equatorial OHC changes are strongest both due to ocean dynamics (Sverdrup

315   transports) and surface fluxes (mainly evaporation, but also surface radiation), but DIVFO

316   quantitatively dominates in this region. However, as will be demonstrated below, DIVFO anomalies

317   related to ENSO almost vanish when averaged over 30S-30N.

318

319

320

13

321   **d) Quantification of energy exchanges between the tropical basins**

322   Tropical Pacific regression coefficients of Rad_{TOA}, DIVFA and OHCT from different datasets with N34

323   at different lags are presented in Fig. 4a. At zero lag, the Pacific atmosphere exports more energy than

324   normal on the order of 0.20 ± 0.04 PWK^{-1} during warm ENSO events. This is the extra energy driving

325   global teleconnections (Trenberth et al. 2002).   At the same time, area-averaged Rad_{TOA} responds

326   comparatively weakly, on the order of -0.06 ± 0.04 PWK^{-1}, in agreement with results from CERES for

327   the shorter period covered (not shown). The sum of these two values is in excellent agreement with

328   associated OHC changes of -0.26 ± 0.07 PWK^{-1}. OHCT regression coefficients from the three employed

329   datasets agree very well despite the different assimilation approaches, probably as a result of the

330   relatively dense ocean observation system in this region. Most convincingly, the combined DIVFA and

331   Rad_{TOA} regression coefficients from ERA-I at zero lag (0.26PWK^{-1}) are perfectly balanced by the

332   OHCT regression coefficient obtained from the fully independent HEN3 data set (-0.26PWK^{-1}). This

333   indirectly indicates that the contribution of DIVFO variability to the Pacific energy balance variability

334   should be close to zero. We also computed OHCT regression coefficients for an integration depth of

335   700m and found the signal to be increased by 10% on the expense of 50% increased noise (-

336   0.29 ± 0.11PWK^{-1}, not shown).

337   Additionally, we also performed a lagged regression analysis of ocean heat transport by the ITF and

338   Pacific poleward heat export computed directly from temperature and velocity fields of ORAS4,

339   presented in Fig. 5. While poleward ocean heat export shows insignificant response to ENSO at all

340   lags, the response of heat transport through the ITF is small at zero lag, but considerable at positive lags

341   (-0.10 ± 0.03PWK^{-1} at six months lag). Thus, the energy balance around six months lag has to include

342   also the ITF heat transport to be reasonably closed. The sum of the regression coefficients of DIVFA,

343   Rad_{TOA}, OHCT and ITF heat transport is close to zero at all lags (not shown). It is important to note

14

344   that this balance does not necessarily hold for individual ENSO events, but it holds for the average

345   response of the energy budget to ENSO.

346   We stress again the vital importance of ocean heat content (OHC) redistribution within the Pacific due

347   to ocean heat transports but that strong mutual cancellation of DIVFO anomalies leads to a small

348   residual signal in area-averaged DIVFO.

349   Regression curves for the tropical Atlantic (30S-30N) are presented in Fig. 4b. Compared to the Pacific

350   ocean, the response of Atlantic OHCT and DIVFA has a similar magnitude (larger regression

351   coefficients in an area-specific sense, smaller coefficients in the area integral due to the smaller basin

352   size), but opposite sign ($+0.12\pm0.04$ PWK^{-1} and -0.14 ± 0.04 PWK^{-1}, respectively). The Rad$_{TOA}$ response

353   is very small and Atlantic ocean heat export computed directly from ORAS4 shows no significant

354   ENSO response at lags less than one year (Fig. 5). Thus, we conclude that in the tropical Atlantic

355   ENSO-related variability in DIVFA is almost entirely balanced by OHCT. Note also that no net surface

356   flux data have been employed to obtain this result (F_S is eliminated when subtracting Eqs. (1) and (2)).

357   Analogous analysis for the Indian Ocean (Fig. 4c and Fig. S3c) suggests a similar balance between

358   OHCT and DIVFA, plus a small contribution from Rad$_{TOA}$, but the fields are less consistent than in the

359   Atlantic case ($+0.08\pm0.05$ PWK^{-1}, -0.06 ± 0.03 PWK^{-1}, and $+0.02\pm0.01$ PWK^{-1}, respectively). The

360   OHCT regression coefficients from the different datasets differ considerably and the Indian ocean heat

361   transport across 30S appears to compensate ITF transport anomalies to some degree (not shown), but it

362   is unclear how robust this result is. Hence, uncertainties appear higher for the Indian Ocean compared

363   to the other tropical basins.

364   Finally, we consider the sum of the three tropical ocean basins (Fig. 4d). At zero lag, we find almost

365   perfect mutual compensation of DIVFA anomalies over the three basins. Hence, the positive response

366   of poleward divergent atmospheric energy transports from the Central and Eastern tropical Pacific

15

367   region as indicated by Fig. 2a is compensated by a negative response of poleward atmospheric energy

368   transports over the Indo-Pacific Warm Pool and the Atlantic. There is, within uncertainty bounds, no

369   net atmospheric energy export anomaly from the tropics during the peak ENSO phase. This confirms

370   the results of Mayer and Haimberger (2012) finding only weak correlation of zonal mean tropical

371   atmospheric energy export with ENSO. OHC changes in the Indian and Atlantic Oceans for the most

372   part compensate Pacific OHC changes. Only for lags around six months, there is a net atmospheric

373   energy export anomaly from the tropics and also radiative energy loss at TOA (in quantitative

374   agreement with CERES, not shown). The atmospheric energy export a few months after the El Niño

375   peak phase probably is a result of increasing SSTs in the Atlantic and Indian Oceans reinvigorating the

376   regional Hadley cells. However, these signals are relatively weak and there is considerable uncertainty

377   (significant correlation only for MERRA DIVFA, but not ERA-I DIVFA, see Fig. S3d), but Rad_{TOA},

378   DIVFA and OHCT still agree within (large) error bounds.

379

380

381   **e) Constrained regression**

382   In section 3d we found that the sum of regression coefficients of those terms in Eqs. (1) and (2), which

383   are significantly different from zero, is close to but not exactly zero when considering basin-averaged

384   series. This closure is remarkable and it is certainly desirable to obtain budget closure without any

385   constraints.

386   However, in this section we illustrate how to obtain numerically exact budget closure by computing the

387   basin-averaged regression coefficients under the strong constraint of adding up to zero. Similar to the

388   approach of Bollmeyer and Hense (2014) to close the atmospheric energy budget, the idea here is to

389   minimize a cost function, which includes terms representing the squared errors for each field as known

16

390   from the ordinary least squares method and one term representing the strong constraint of our coupled

391   energy budget (see S5 for derivation). To be consistent, full-depth OHCT fields are employed for this

392   purpose. This introduces considerable noise in the OHCT fields from depths below 300m, as already

393   discussed. Moreover, the determination of uncertainty estimates associated with each field, especially

394   the ratios of uncertainties of different fields, is crucial for the results (see S5). Here, we take values

395   obtained from the ordinary least squares regression as presented in section 3d (see the left column of

396   table 1 for a summary of the used uncertainty values).

397   Results from the constrained regression exemplary for the tropical Pacific at zero lag are presented in

398   table 1. The constrained regression coefficients for all fields are well within uncertainty bounds of the

399   unconstrained estimates. The regression coefficient of OHCT is changed the most, because estimated

400   OHCT uncertainty is by far the highest compared to the other fields. Regression coefficients of the

401   other fields are adjusted only weakly. Note that uncertainties here are estimated only from sampling

402   uncertainty. The main difficulty of this method is that the tendency or flux fields with smallest

403   sampling uncertainties are not necessarily those with the smallest biases. The purpose of this section is

404   rather to illustrate this possible post-processing step. Generally, this method shifts the problem of

405   imperfect data reflected in imperfect budget closure (of the regression coefficients) to the difficulty

406   associated with estimation of the uncertainties required for the constrained regression. Therefore, and

407   because the imbalances of the unconstrained regression coefficients are mostly small, we will discuss

408   the unconstrained results in the following section.

409

410

411   **4. Discussion and conclusions**

412   Ample changes in circulation and associated changes in clouds, precipitation, and radiation in response

17

413   to ENSO (as described in section 1 and references given therein) lead to an indirect redistribution of

414   OHC across tropical ocean basins via the atmosphere. Most of the extra heat released (stored) from (in)

415   the tropical Pacific during El Niño (La Niña) indirectly leads to increasing (decreasing) OHC in the

416   other tropical basins. During peak ENSO conditions, tropical Atlantic OHC changes account for about

417   45% of Pacific OHC changes, although it comprises only 12% of the total ocean area, and Indian OHC

418   changes account for about 30%, which comprises about 11% of the total ocean area. Accompanied by

419   altered regional Hadley cells over the respective basins and anomalous zonal circulations between the

420   basins, horizontal atmospheric energy transports (DIVFA) show variations quantitatively consistent

421   with OHC changes, especially over the Atlantic.

422   Contribution of the ITF ocean heat transport variability to tropical Pacific OHC changes is not

423   negligible and has to be included to reasonably close the tropical Pacific energy budget. Poleward

424   oceanic heat export from the tropical Pacific shows little ENSO correlation. Hence, while anomalous

425   ocean heat transports in association with ENSO are large within the tropical Pacific (see section 3c),

426   the largest part of basin-averaged OHC changes is realized through surface fluxes and not through

427   lateral ocean heat transports out of that region. A similar conclusion can be drawn for the tropical

428   Atlantic, with the addition that there ENSO-related ocean heat transports are relatively small also

429   within the basin (in contrast to the Pacific).

430   The small regression coefficient of Pacific poleward ocean heat export does not necessarily exclude

431   that ENSO-related export anomalies may happen occasionally. Inspections of the time series in Fig. 1a

432   show positive ocean heat export anomalies out of the tropical Pacific in association with the strong La

433   Niña events in 1999 and 2008. Whether these anomalies are a random occurrence, or they are related

434   to the non-linearities of strong ENSO events, or they reflect the interaction with any other mode of the

435   climate system (such as the Pacific Decadal Oscillation) is an interesting question but beyond the scope

18

436   of this paper.

437   Variability of tropical Pacific Rad_{TOA} is correlated significantly with ENSO (r=-0.57 at six months lag

438   5), but according to our calculations only about 20% of the anomalous tropical Pacific OHC is

439   exchanged at TOA, mainly in the Pacific subtropics, and ENSO-related Rad_{TOA} anomalies over the

440   other basins are negligible. Hence, ENSO-related variability of atmospheric energy export from the

441   tropical Atlantic region is energetically strongly coupled to tropical Atlantic OHC (via net surface

442   fluxes), while net radiation at TOA plays a negligible role in this balance. Overall, our results explain

443   the comparatively small global mean TOA signal of ENSO, found e.g. by Loeb et al. (2012).

444   It is remarkable how distinct and robust the obtained results are despite of known shortcomings in the

445   data, e.g. the missing signature of volcanic eruptions in Rad_{TOA} from ERA-Interim. Tests also showed

446   that splitting background climatologies for computation of anomalies to reduce temporal data

447   inhomogeneities as carried out by Mayer et al. (2013) resulted in slightly higher correlations.

448   Regression and correlation, albeit highly significant, of course do not prove causality, but our results

449   are consistent with the physical understanding of the response of the tropical ocean-atmosphere system

450   to ENSO. The presented pathways of energy are summarized in a schematic exemplary for the Pacific

451   and Atlantic basins in Fig. 6. We also note that the presented results describe the first order linear

452   response of the energy budgets to an average canonical ENSO event and naturally neglect non-linear

453   effects of strong events, asymmetries between warm and cold events, as well as the different flavors of

454   single ENSO events. Yet, budget closure for single events proves elusive with current data sets.

455   Global climate models, by construction, satisfy global mean consistency requirements such as

456   replication of anomalous TOA fluxes in OHCT on interannual time scales (Wong et al. 2006), while

457   current oceanic reanalysis datasets practically fail to do so (Loeb et al. 2012, Trenberth et al. 2014). As

458   can be seen from our results, this is due to compensating processes in association with climate

19

459 variability, which only leave a small global mean residual signal. However, here we demonstrate that,

460 when carefully selecting regions to maximize signal-to-noise ratio, largely independent observation-

461 based data sets of the atmosphere and ocean exhibit very good agreement. Thus, these results provide a

462 new quantitative benchmark for the replication of ENSO-related energy flows and exchanges in

463 coupled climate models. It is intended to apply it to CMIP5 (Coupled Model Intercomparison Project

464 Phase 5) model output in the near future.

465

466 **Acknowledgements**

471

472 **References**

473 Balmaseda, M.A., Mogensen, K. and Weaver, A.T., 2012. Evaluation of the ECMWF ocean
474   reanalysis system ORAS4. *Quarterly Journal of the Royal Meteorological Society*, 139,
475   pp.1132 – 1161.

476 Balmaseda, M.A., Trenberth, K.E. and Källén, E., 2013. Distinctive climate signals in reanalysis of
477   global ocean heat content. *Geophysical Research Letters*, 40, pp.1754 – 1759.

478 Berrisford, P. et al., 2011. Atmospheric conservation properties in ERA-Interim. *Quarterly Journal*
479   *of the Royal Meteorological Society*, 137(659), pp.1381–1399.

480 Bollmeyer, C. and Hense, A., 2014. Inverse modeling of energy transports and budgets of the
481   atmosphere. *Climate Dynamics*, pp.1–16.

482 Clarke, A.J., Van Gorder, S. and Colantuono, G., 2007. Wind stress curl and ENSO
483   discharge/recharge in the equatorial Pacific. *Journal of physical oceanography*, 37(4),
484   pp.1077–1091.

20

485   Dee, D.P. et al., 2011. The ERA-Interim reanalysis: Configuration and performance of the data
486   assimilation system. *Quarterly Journal of the Royal Meteorological Society*, 137(656),
487   pp.553–597.

488   Enfield, D.B. and Mayer, D.A., 1997. Tropical Atlantic sea surface temperature variability and its
489   relation to El Niño-Southern Oscillation. *Journal of Geophysical Research: Oceans (1978–*
490   *2012)*, 102(C1), pp.929–945.

491   England, M.H. and Huang, F., 2005. On the interannual variability of the Indonesian Throughflow
492   and its linkage with ENSO. *Journal of climate*, 18(9), pp.1435–1444.

493   Grist, J.P. et al., 2010. The roles of surface heat flux and ocean heat transport convergence in
494   determining Atlantic Ocean temperature variability. *Ocean Dynamics*, 60(4), pp.771–790.

495   Hasegawa, T. and Hanawa, K., 2003. Heat content variability related to ENSO events in the Pacific.
496   *Journal of physical oceanography*, 33(2), pp.407–421.

497   Ingleby, B. and Huddleston, M., 2007. Quality control of ocean temperature and salinity profiles—
498   Historical and real-time data. *Journal of Marine Systems*, 65(1), pp.158–175.

499   Jin, F.F., 1997. An equatorial ocean recharge paradigm for ENSO. Part I: Conceptual model. *Journal*
500   *of the Atmospheric Sciences*, 54(7), pp.811–829.

501   Klein, S.A., Soden, B.J. and Lau, N.C., 1999. Remote sea surface temperature variations during
502   ENSO: Evidence for a tropical atmospheric bridge. *Journal of Climate*, 12(4), pp.917–932.

503   Lengaigne, M. et al., 2012. Mechanisms controlling warm water volume interannual variations in
504   the equatorial Pacific: diabatic versus adiabatic processes. *Climate dynamics*, 38(5-6),
505   pp.1031–1046.

506   Loeb, N.G. et al., 2012. Observed changes in top-of-the-atmosphere radiation and upper-ocean
507   heating consistent within uncertainty. *Nature Geoscience*, 5(2), pp.110–113.

508   Lohmann, K. and Latif, M., 2007. Influence of El Niño on the upper-ocean circulation in the
509   tropical Atlantic Ocean. *Journal of Climate*, 20(19), pp.5012–5018.

510   Mayer, M. et al., 2013. The Response of Tropical Atmospheric Energy Budgets to ENSO. *Journal of*
511   *Climate*, 26(2013), pp.4710–4724.

512   Mayer, M. and Haimberger, L., 2012. Poleward Atmospheric Energy Transports and Their
513   Variability as Evaluated from ECMWF Reanalysis Data. *J. Climate*, 25(2), pp.734–752.

514   Meinen, C.S. and McPhaden, M.J., 2000. Observations of warm water volume changes in the
515   equatorial Pacific and their relationship to El Niño and La Niña. *Journal of Climate*, 13(20),
516   pp.3551–3559.

517   Oort, A.H. and Yienger, J.J., 1996. Observed interannual variability in the Hadley circulation and
518   its connection to ENSO. *Journal of Climate*, 9(11), pp.2751–2767.

21

519   Rienecker, M.M. et al., 2011. MERRA: NASA's Modern-Era Retrospective Analysis for Research
520   and Applications. *Journal of Climate*, 24(14), pp.3624–3648.

521   Roemmich, D. and Gilson, J., 2011. The global ocean imprint of ENSO. *Geophysical Research
522   Letters*, 38(13), p.L13606.

523   Simmons, A.J. et al., 2013. Estimating low-frequency variability and trends in atmospheric
524   temperature using ERA-Interim. *Quarterly Journal of the Royal Meteorological Society*, 140,
525   pp.329–353.

526   Sun, D.-Z., 2000. The heat sources and sinks of the 1986-87 El Niño. *Journal of climate*, 13(20),
527   pp.3533–3550.

528   Trenberth, K.E. et al., 2002. Evolution of El Niño–Southern Oscillation and global atmospheric
529   surface temperatures. *Journal of geophysical research*, 107(D8), p.4065.

530   Trenberth, K.E. et al., 2007. *Observations: Surface and Atmospheric Climate Change, chap. 3 of
531   Climate Change 2007: The Physical Science Basis. Contribution of Working Group I to the
532   Fourth Assessment Report of the Intergovernmental Panel on Climate Change [Solomon, S.,
533   Qin, D., Manning, M., Marquis, M., Averyt, KB, Tignor, M., Miller, HL and Chen, Z.(eds.)]., 235–
534   336*, Cambridge University Press, Cambridge, UK and New York, NY, USA.

535   Trenberth, K.E. et al., 2010. Relationships between tropical sea surface temperature and top-of-
536   atmosphere radiation. *Geophys. Res. Lett*, 37, p.L03702.

537   Trenberth, K.E. and Fasullo, J.T., 2008. An Observational Estimate of Inferred Ocean Energy
538   Divergence. *Journal of Physical Oceanography*, 38(5), pp.984–999.

539   Trenberth, K.E. and Fasullo, J.T., 2012. Tracking Earth's energy: from El Niño to global warming.
540   *Surveys in geophysics*, 33(3-4), pp.413–426.

541   Trenberth, K.E., Fasullo, J.T. and Balmaseda, M.A., 2014. Earth's Energy Imbalance. *J. Climate, in
542   press*.

543   Trenberth, K.E., Stepaniak, D.P. and Caron, J.M., 2002. Interannual variations in the atmospheric
544   heat budget. *J. Geophys. Res*, 107(4066), p.10.1029.

545   Wang, C., 2005. ENSO, Atlantic Climate Variability, and the Walker and Hadley Circulations in
546   *Hadley Circulation: Present, Past, and Future* pp. 173–202 (Springer Amsterdam).

547   Wielicki, B.A. et al., 1996. Clouds and the Earth's Radiant Energy System (CERES): An Earth
548   Observing System Experiment. *Bulletin of the American Meteorological Society*, 77(5),
549   pp.853–868.

550   Wong, T. et al., 2006. Reexamination of the observed decadal variability of the earth radiation
551   budget using altitude-corrected ERBE/ERBS nonscanner WFOV data. *Journal of Climate*,
552   19(16), pp.4028–4040.

22

553   Zhang, S. et al., 2007. System design and evaluation of coupled ensemble data assimilation for
554   global oceanic climate studies. *Monthly Weather Review*, 135(10), pp.3541–3564.

555   **Tables**

	OLS	Constrained OLS
-Rad$_{TOA}$	**0.06±0.04**	**0.07±0.04**
DIVFA	**0.20±0.04**	**0.21±0.04**
AET	-0.01±0.02	-0.01±0.01
OHCT (0-300m)	**-0.26±0.07**	--
OHCT (0-bottom)	**-0.28±0.13**	**-0.21±0.08**
-ITF	**-0.04±0.04**	**-0.04±0.03**
Pacific 30N-30S	-0.03±0.05	-0.02±0.04

556

557   **Table 1.** Regression coefficients of all budget terms at zero lag for tropical Pacific from ordinary least

558   squares (OLS) and constrained OLS with 95%-confidence intervals. Units are PWK^{-1}. Bold values are

559   significantly different from zero. Uncertainties for the constrained OLS results are estimated with a

560   block bootstrap method (length of the blocks is set to six months).

561

562

563

564

565

566

567

568

23

569

570   **Figure caption list**

571

572   **Fig. 1.** Time series of budget-relevant fields area-integrated over (a) the tropical Pacific (30N-30S) and

573   (b) the Atlantic Ocean (units are PW). Shown are 13-point-filtered anomalies (annual cycle removed)

574   with the respective long-term mean added. For the ERA-I curve, the CERES mean is added. The ITF

575   heat transport is defined positive westward. Vertical light red and blue bars indicate warm and cold

576   ENSO events, respectively, as defined by the National Oceanic and Atmospheric Administration.

577

578   **Fig. 2. Regression of energy budget fields onto N34.** Regression of (a) ERA-I DIVFA and divergent

579   energy transport, (b) indirectly estimated F_S, (c) ORAS4 OHCT and (d) SST with N34 at zero lag.

580   Scatter plots of area-averaged tropical (e) Pacific and (g) Atlantic (30S-30N) DIVFA (ERA-I)

581   anomalies with N34 (red squares represent all Decembers – ENSO events usually peak in December).

582   Scatter plots of area-averaged tropical (f) Pacific and (h) Atlantic (30S-30N) OHCT (ORAS4)

583   anomalies with N34 (blue squares represent all Decembers). Continuous red/blue regression lines in e-h

584   are computed from the full 1979-2012 sample, dashed regression lines from the 34 December sample.

585   Yellow dot in (e) denotes the regression coefficient of tropical Pacific DIVFA in $Wm^{-2}K^{-1}$. 1 PW
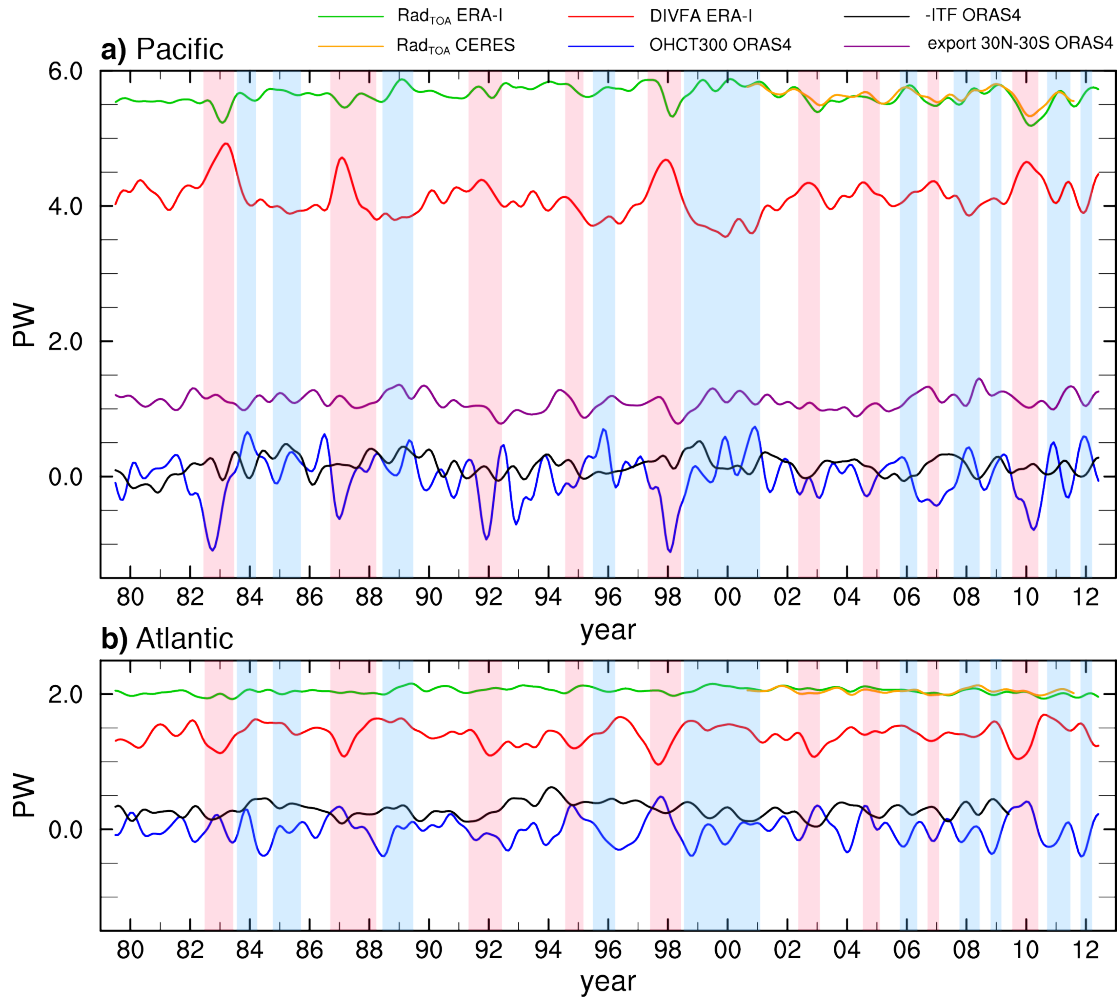
586   corresponds to 2 Wm^{-2} globally.

587

588   **Fig. 3.** Regression of area-averaged Rad_{TOA}, DIVFA and OHCT with N34 as a function of lag for

589   equatorial Pacific (5S-5N). Left axis gives area-specific values, right axis gives area-integrated values

590   for each curve. Shading represents 95%-confidence intervals of the regression coefficients, computed

591   from the residual sum of squares of the respective ensemble mean, taking autocorrelation into account.

24

592   **Fig. 4.** Regression of area-averaged Rad_{TOA}, DIVFA and OHCT with N34 as a function of lag, (a) for

593   tropical Pacific (30S-30N), (b) for tropical Atlantic (30S-30N), (c) for Indian Ocean (30S-30N), (d) for

594   all tropical ocean basins (360°, 30S-30N). Left axes give area-specific values, right axes give area-

595   integrated values for each curve. Shading represents 95%-confidence intervals of the regression

596   coefficients, analogous to Fig. 3. Yellow dot represents the regression coefficient of DIVFA at lag 0,

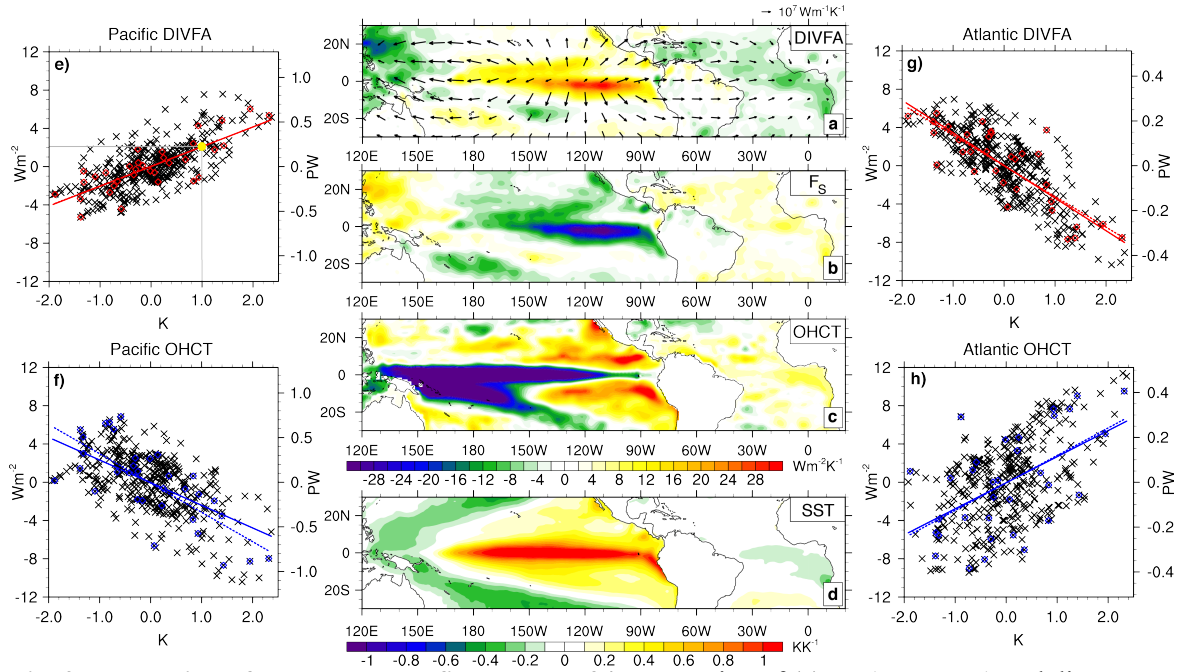597   i.e. the same value as the yellow dot in Fig. 2e.

598

599   F**ig. 5.** Regression of ITF, Pacific poleward heat export and Atlantic poleward heat export from ORAS4

600   with N34 as a function of lag. Shading represents 95%-confidence intervals, analogous to Fig. 3.

601

602   **Fig. 6. Schematic of anomalous energy fluxes within and between tropical atmosphere and**

603   **oceans**. Depicted is anomalous divergence of atmospheric energy transport, anomalous fluxes at the

604   surface (Rad_S denotes net radiation at the surface, LH and SH latent and sensible heat flux,

605   respectively), at TOA and anomalous heat transport by the ITF (yellow arrows), as well as anomalous

606   SSTs and OHCT as a response to El Niño (based on regression with N34 at zero lag). Note the strong

607   west-east compensation of OHCT in the Pacific which is due to zonal oceanic heat transports. White

608   arrows in the atmosphere indicate circulation anomalies in the vertical-equatorial plane associated with

609   the Walker cells.

610

611

612

613

614

25

615   **Figures**

616

617   **Fig. 1.** Time series of budget-relevant fields area-integrated over (a) the tropical Pacific (30N-30S) and

618   (b) the Atlantic Ocean (units are PW). Shown are 13-point-filtered anomalies (annual cycle removed)

619   with the respective long-term mean added. For the ERA-I curve, the CERES mean is added. The ITF

620   heat transport is defined positive westward. Vertical light red and blue bars indicate warm and cold

621   ENSO events, respectively, as defined by the National Oceanic and Atmospheric Administration.

622

26

623
624   **Fig. 2. Regression of energy budget fields onto N34.** Regression of (a) ERA-I DIVFA and divergent

625   energy transport, (b) indirectly estimated F_S, (c) ORAS4 OHCT and (d) SST with N34 at zero lag.

626   Scatter plots of area-averaged tropical (e) Pacific and (g) Atlantic (30S-30N) DIVFA (ERA-I)

627   anomalies with N34 (red squares represent all Decembers – ENSO events usually peak in December).
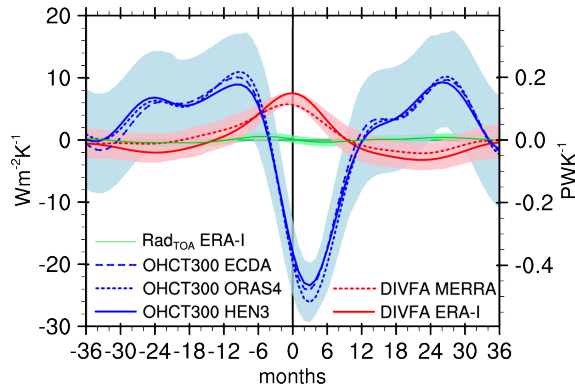
628   Scatter plots of area-averaged tropical (f) Pacific and (h) Atlantic (30S-30N) OHCT (ORAS4)

629   anomalies with N34 (blue squares represent all Decembers). Continuous red/blue regression lines in e-h

630   are computed from the full 1979-2012 sample, dashed regression lines from the 34 December sample.

631   Yellow dot in (e) denotes the regression coefficient of tropical Pacific DIVFA in $Wm^{-2}K^{-1}$. 1 PW
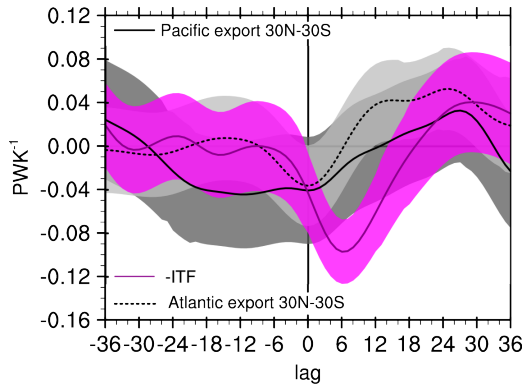
632   corresponds to 2 Wm^{-2} globally.

27

Fig. 3. Regression of area-averaged Rad_{TOA}, DIVFA and OHCT with N34 as a function of lag for equatorial Pacific (5S-5N). Left axis gives area-specific values, right axis gives area-integrated values for each curve. Shading represents 95%-confidence intervals of the regression coefficients, computed from the residual sum of squares of the respective ensemble mean, taking autocorrelation into account.
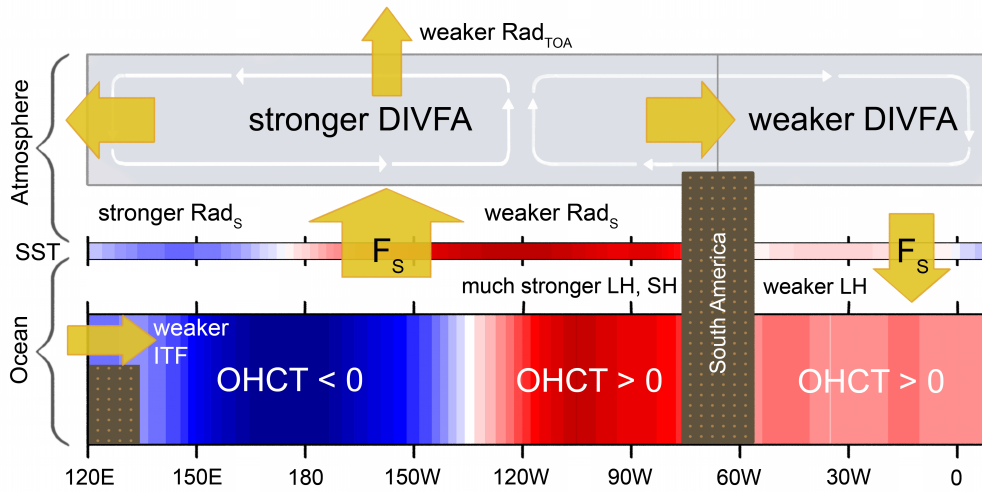
28
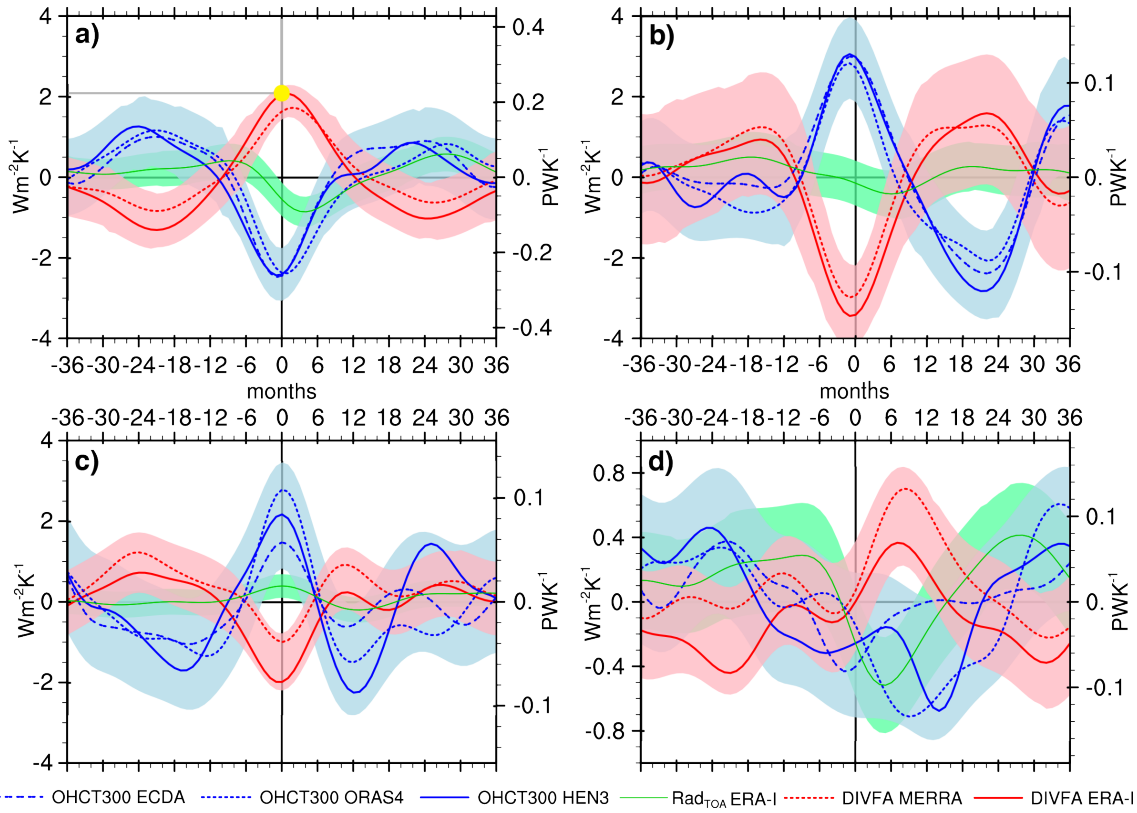
Fig. 4. Regression of area-averaged Rad$_{TOA}$, DIVFA and OHCT with N34 as a function of lag, (a) for tropical Pacific (30S-30N), (b) for tropical Atlantic (30S-30N), (c) for Indian Ocean (30S-30N), (d) for all tropical ocean basins (360°, 30S-30N). Left axes give area-specific values, right axes give area-integrated values for each curve. Shading represents 95%-confidence intervals of the regression coefficients, analogous to Fig. 3. Yellow dot represents the regression coefficient of DIVFA at lag 0, i.e. the same value as the yellow dot in Fig. 2e.

29

659

660   **Fig. 5.** Regression of ITF, Pacific poleward heat export and Atlantic poleward heat export from

661   ORAS4 with N34 as a function of lag. Shading represents 95%-confidence intervals, analogous to Fig.

662   3.

663

664

665   **Fig. 6. Schematic of anomalous energy fluxes within and between tropical atmosphere and**

666   **oceans**. Depicted is anomalous divergence of atmospheric energy transport, anomalous fluxes at the

667   surface (Rad$_S$ denotes net radiation at the surface, LH and SH latent and sensible heat flux,

668   respectively), at TOA and anomalous heat transport by the ITF (yellow arrows), as well as anomalous

30

669   SSTs and OHCT as a response to El Niño (based on regression with N34 at zero lag). Note the strong

670   west-east compensation of OHCT in the Pacific which is due to zonal oceanic heat transports. White

671   arrows in the atmosphere indicate circulation anomalies in the vertical-equatorial plane associated with

672   the Walker cells.

31

Supplemental material for

On the energy exchange between tropical ocean basins related to ENSO

Michael Mayer, Leopold Haimberger and Magdalena A. Balmaseda

S1 Pacific ocean heat export
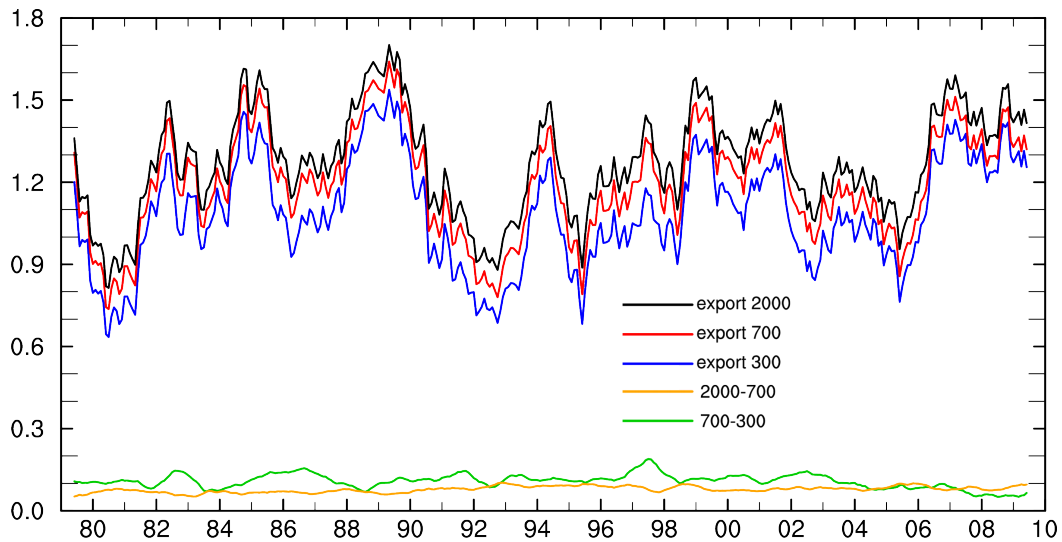
Fig. S1. Time series of ORAS4 ocean heat export from the tropical Pacific, i.e. the sum of the transports across 30N, 30S and by the ITF, computed directly from velocity and temperature fields (units are PW). Shown are curves for 300m, 700m, 2000m integration depth and the difference between the curves. Series represent 13-point-filtered anomalies (annual cycle removed) with the respective long-term mean added.

S2 Timeseries of area-averaged divergence of ocean heat transport

a)
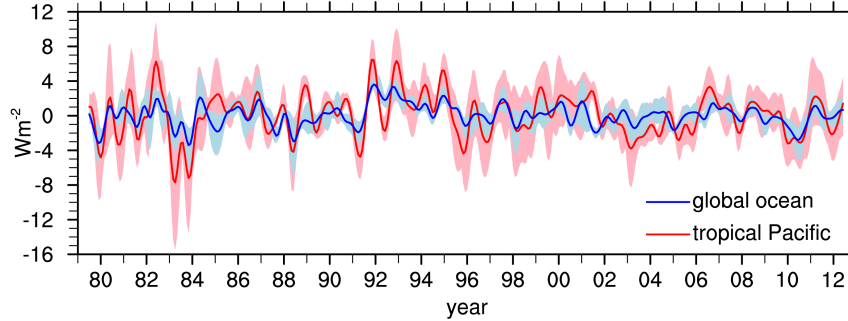
b)
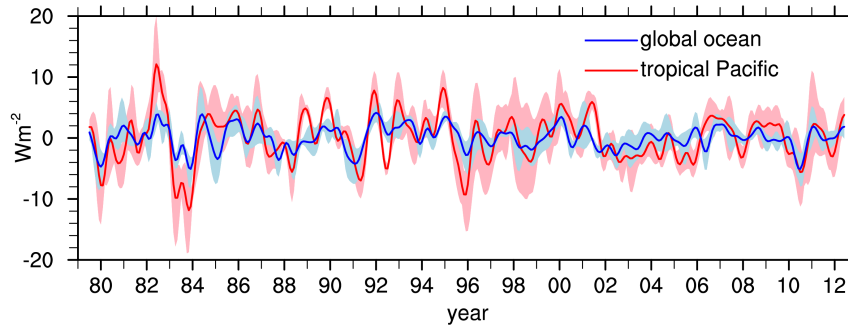
Fig. S2. Indirectly estimated DIVFO anomalies averaged globally, and over the Pacific (30S-30N), employing OHCT of the (a) upper 300m and (b) upper 700m from ORAS4, HEN3 and ECDA. Shading represents the range of different DIVFO estimates obtained from all possible combinations of F_S and OHCT fields. Solid lines represent the respective ensemble means. Note the overlap of the shaded areas during most of the period and the high correlation of the curves (r=0.69), indicating that tropical Pacific DIVFO is indistinguishable from global DIVFO (i.e. noise).

S3 Correlation of energy budget fields for the tropical Pacific, Atlantic, Indian

Oceans and the tropical belt with N34
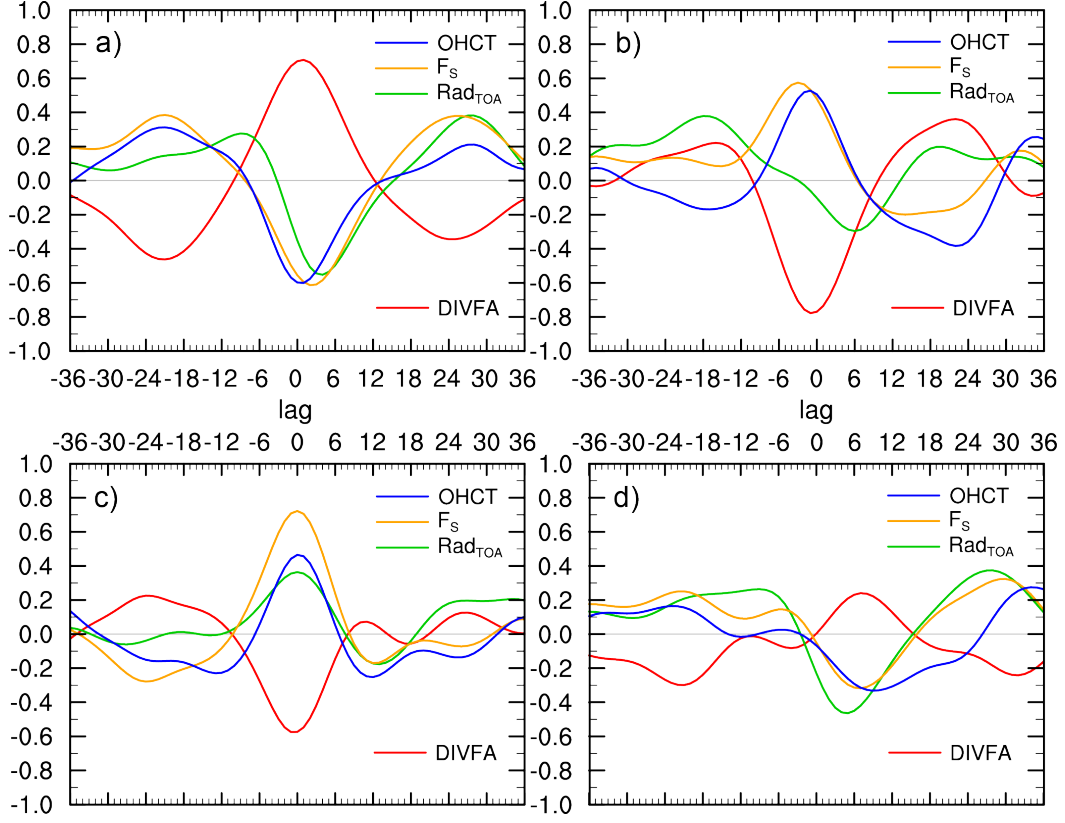
Fig. S3a. Cross-correlation of **Rad$_{TOA}$** (48 degrees of freedom (dof)), **F$_S$** (dof=43), **OHCT** (dof=66), and **DIVFA** (dof=44) anomalies averaged over tropical Pacific (30S-30N) with N34.

Fig. S3b. Cross-correlation of **Rad$_{TOA}$** (dof=45), **F$_S$** (dof=51), **OHCT** (dof=67), and **DIVFA** (dof=51) anomalies averaged over tropical Atlantic (30S-30N) with N34.

Fig. S3c. Cross-correlation of **Rad$_{TOA}$** (dof=49), **F$_S$** (dof=53), **OHCT** (dof=71), and **DIVFA** (dof=56) anomalies averaged over tropical Indian Ocean (30S-30N) with N34.

Fig. S3d. Cross-correlation of **Rad$_{TOA}$** (dof=42), F$_S$ (dof=40), **OHCT** (dof=57), and DIVFA (dof=42) anomalies averaged over all tropical ocean basins (30S-30N) with N34.

Fields with maximum correlation coefficients with confidence >95% are printed bold.

Degrees of freedom are given at the respective lag of maximum correlation with N34. All

curves shown here are derived from ERA-I and ORAS4, respectively.

S4 Impact of larger integration depth on Pacific OHCT regression
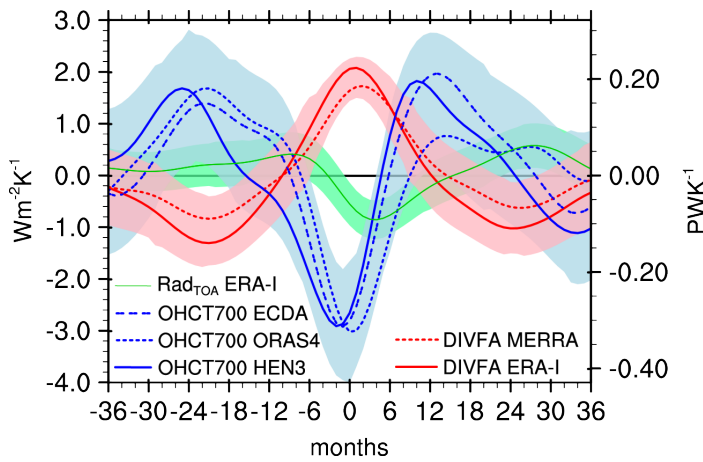
Fig. S4. Regression of area-averaged Rad_{TOA}, DIVFA and OHCT (integration depth

700m) with N34 as a function of lag for tropical Pacific (30S-30N).

Shading represents 95%-confidence intervals of the regression coefficients, analogous to

Fig. 3 in the main text. Note the similar OHCT regression coefficients but their much

larger uncertainty bounds compared to Fig. 4a in the main text.

S5 Derivation of the equations for the constrained regression method

The constrained ordinary least squares method seeks to minimize the cost function

$$J(\beta_{DIVFA},...,\beta_{OHCT},\lambda) = \frac{1}{\sigma_{DIVFA}^2}(\mathbf{X}^T\mathbf{X}\beta_{DIVFA} - \mathbf{X}^T\mathbf{Y}_{DIVFA}) + ... +$$

$$+ \frac{1}{\sigma_{OHCT}^2}(\mathbf{X}^T\mathbf{X}\beta_{OHCT} - \mathbf{X}^T\mathbf{Y}_{OHCT}) + \lambda(\beta_{DIVFA} + ... + \beta_{OHCT}),$$

with σ_j representing the uncertainty of the respective field (j=DIVFA, Rad$_{TOA}$, AET, OHCT, DIVFO), $\mathbf{X}$ representing the vector of all Niño 3.4 index values, $\mathbf{Y}_j$ representing the observation vector of the respective field, and β_j representing the regression coefficient of the respective field. For convenience, here the signs of all fields are chosen to contribute positively to J.

The strong constraint (consistent with Eq. (1) and Eq. (2) in the main text) is defined as

$$\beta_{DIVFA} + \beta_{AET} + \beta_{Rad_{TOA}} + \beta_{DIVFO} + \beta_{OHCT} = 0.$$

Derivation of J with respect to each variable yields a set of six linear equations with six unknowns. This system can be easily solved. For example, the constrained regression coefficient of OHCT reads as follows:

$$\beta_{OHCT} = (\mathbf{X}^T\mathbf{X})^{-1}\mathbf{X}^T\mathbf{Y}_{OHCT} - (\mathbf{X}^T\mathbf{X})^{-1}\sigma_{OHCT}^2\lambda, \text{ with}$$

$$\lambda = \frac{\mathbf{X}^T\mathbf{Y}_{DIVFA} + ... + \mathbf{X}^T\mathbf{Y}_{OHCT}}{\sigma_{DIVFA}^2 + ... + \sigma_{OHCT}^2}.$$

The constrained regression coefficients for all other fields are computed analogously. In case of the Pacific ocean, DIVFO is further split into the sum of i) ITF transports and ii) poleward heat export across 30N and 30S. Hence, in this case J is dependent on seven variables, but computation of the regression coefficients is analogous to the procedure described above.

6 Discussion and conclusions

In the introduction of the present thesis three main research goals were defined: (i) providing an up-to-date quantification of time-averaged poleward atmospheric energy transports, (ii) exploration of zonally resolved variability of atmospheric energy budgets in the tropical belt in association with ENSO and, as extension of (ii), (iii) exploration of variability of the coupled atmospheric and oceanic energy budget on the scale of tropical ocean basins to assess pathways of energy through the climate system in association with ENSO.

Research question (i) was assessed by employing state-of-the-art reanalysis ERA-Interim, to evaluate climatological mean poleward atmospheric energy transports with an indirect and a direct method. Results from both methods agree quite well with each other quantitatively. The respective peaks of meridional transports on the Northern and Southern Hemisphere obtained from the direct method are 4.8±0.1PW and -5.4±0.2PW. The result for the Northern Hemisphere agrees with the value of 5.1±0.5PW obtained by Fasullo and Trenberth (2008b), who employed older atmospheric datasets such as ECMWF's 40-year Reanalysis (ERA-40, Uppala et al. 2005). However, their result for the Southern Hemisphere peak transport (-4.9±0.2PW) is significantly weaker than suggested by the results presented in Mayer and Haimberger (2012). Hence, although the evaluation methods for the transports, especially the mass adjustment, are similar in Mayer and Haimberger (2012) and Fasullo and Trenberth (2008b), obtained values for these fundamental quantities still vary considerably from one generation of reanalysis datasets to another.

A different approach for evaluation of mean poleward energy transports within the atmosphere has been taken by Bollmeyer and Hense (2014), who employed a variational method to adjust atmospheric transports from ERA-40 with the information from satellite radiation at TOA and surface fluxes from different datasets. Their results for the peak transports agree with those given in Mayer and Haimberger (2012), but they use dated satellite data, not the newest generation of atmospheric reanalyses, and winds without mass adjustment, making their results less reliable despite the innovative method. However, their variational approach is promising and applied to mass adjusted fields of energy transports from more recent reanalyses as well as up-to-date satellite data could certainly lead to improved estimates. Thus, the values for the climatological peak transports provided by Mayer and Haimberger (2012) probably represent the current best estimate for the mean poleward atmospheric energy transport, but it is certainly not definitive. This means that comparison of poleward energy transports from climate models to the transports from reanalyses remains a problematic task.

The second part of Mayer and Haimberger (2012) is dedicated to interannual variability of the atmospheric energy budget in ERA-I. In this context temporal homogeneity of ERA-Interim was assessed. Net radiation at TOA from ERA-I was compared with Rad_{TOA} from independent satellite data. This comparison revealed that anomaly agreement between ERA-

I and CERES data is quite good for the period commonly covered at the time of this study (2000/03 - 2010/02), and in terms of temporal homogeneity both data sets appeared to be of equal quality. Comparison of Rad_{TOA} and Rad_S from ERA-I with the respective fields from the older Cloud Climatology Project Flux (ISCCP-FD, Zhang 2004) product demonstrated the clearly better temporal homogeneity of ERA-I, underscoring the high quality of ERA-I. The good quantitative agreement of ERA-I with CERES, which is generally viewed as current reference dataset for Rad_{TOA}, was the reason to trust ERA-I net radiation at TOA also in earlier periods, which are not covered by CERES, in a later part of this thesis (Mayer et al., 2014).

Generally, strong variability associated with ENSO is documented in tropical energy budgets from ERA-I. It is also shown that anomalies of analysis increments (defined as forecasted tendency minus analyzed tendency of atmospheric total energy storage) show some correlation with ENSO and also with net surface fluxes in the tropical Pacific region, i.e., anomalies of forecasted surface fluxes from ERA-I and anomalies of the other budget terms are not fully balanced. This shows that variations in analysis increments do not only arise from changes in the observation system but that they can also be due to true circulation anomalies which are inadequately simulated by the forecast model. One conclusion from this finding was that the indirect evaluation method for the atmospheric energy transports (relying, besides other fields, on surface flux forecasts) is probably less trustworthy compared to the direct method (relying on analyzed atmospheric state variables) when investigating atmospheric budget anomalies. As a consequence, all conclusions drawn later during the course of this thesis are based on direct estimates of the atmospheric energy transports.

The novel transient signals of eastward propagating anomaly patterns of meridional divergent atmospheric energy export from the tropics (30S-30N) in association with ENSO presented in Fig. 13 of Mayer and Haimberger (2012) led to the definition of research goal (ii), namely the exploration of these signals in regard to robustness of these patterns and underlying processes. Therefore, the zonally resolved anomaly structures of the divergence of latent heat transport (LEDIV), dry-static energy transport (DSEDIV) and total energy transport (TEDIV) in the tropics (20N-20S) were investigated in Mayer et al. (2013), employing data from three third-generation reanalysis products ERA-I, MERRA, and National Centers for Environmental Prediction (NCEP) Climate Forecast System Reanalysis (CFSR, Saha et al. 2010). The reason for considering divergences of transports rather than the divergent transports themselves is that, while divergent transports at one grid point are not necessarily associated with a divergence at this grid point, the value of the local divergence is really a result of local processes, i.e., it is associated with the local energy budget. Prior to data analysis, temporal homogeneity of the LEDIV series, which exhibit much stronger inhomogeneities than TEDIV because inhomogeneities in latent heat and dry-static energy tend to compensate each other, from the three reanalyses was improved by a simple homogenization algorithm. The relatively simple

method removes the two largest inhomogeneities from each dataset and improved the results of the subsequent analyses to some degree in certain sensitive regions [see supplemental material of Mayer et al. (2013) for details of the algorithm].

Cross-correlation analysis of the energy divergence fields with the Niño 3.4 index [N34, anomaly index of SSTs area-averaged over 170W-120W, 5S-5N] used as a proxy for the ENSO state showed that especially LEDIV and DSEDIV, which are strongly anti-correlated because latent heating from precipitation appears in both fields with opposite sign, exhibit a quadrupole anomaly structure in association with ENSO. During warm events, tropical (20N-20S) LEDIV exhibits negative anomalies, i.e., stronger moisture convergence than normal, over the central and eastern Pacific as well as over the western Indian Ocean, and positive anomalies, i.e., weaker moisture convergence than normal, over the Indo-Pacific Warm Pool (IPWP) and the Atlantic. The anomaly response of LEDIV during cold ENSO events is reversed. The response of DSE-DIV to ENSO is opposite compared to LEDIV. The main driver of this quadrupole structure of tropical energy divergence anomalies probably is SST. Regional changes in the strength and position of the Hadley cells are associated with regional SST anomalies, which are known to be strongest in the Central and Eastern Pacific (Clarke, 2008). As a consequence of the changes in the Hadley cells, patterns of vertical motion and hence LEDIV and DSEDIV are altered as well. These regional anomalies are linked to the other tropical regions via zonal circulation cells (e.g., Walker circulation, see, e.g., Klein et al. 1999), resulting in the observed quadrupole response of LEDIV and DSEDIV to ENSO.

The eastward propagating anomaly structures are associated with the ENSO phase change. For example, during a La Niña event, negative LEDIV anomalies are found over the IPWP, while positive LEDIV anomalies can be found over the central and eastern Pacific. During a phase change to warm ENSO conditions, warm SSTs from the IPWP will be advected eastward. As SSTs drive atmospheric low level convergence and consequently also LEDIV in the tropics, the negative LEDIV anomalies found over the IPWP during La Niña will also move eastward gradually, arriving in the central to eastern Pacific during El Niño. The other maxima of the quadrupole anomaly structure propagate accordingly due to the connection via anomalous zonal circulation cells, leading to the observed seamless transition between warm and cold ENSO states in the energy budgets.

Further investigation with an EOF analysis revealed that two EOFs are required to adequately describe the eastward propagation of LEDIV and DSEDIV anomalies, a result already noted by von Storch and Zwiers (2002) in a more general context. Additionally, taking LEDIV as a proxy for low-level wind convergence, it was found that the first EOF of LEDIV represents circulation patterns associated with canonical ENSO events and the second EOF of LEDIV represents circulation patterns associated with El Niño Modoki (Ashok et al., 2007) events. Regarding TEDIV, results of Mayer et al. (2013) show that this field also exhibits a quadrupole

anomaly response to ENSO with the same sign as DSEDIV but weaker, because the main driver of TEDIV anomalies in the tropics are surface fluxes which exhibit generally weaker anomalies than precipitation (latent heating) anomalies. EOF analysis reveals that there is a TEDIV pattern associated with El Niño Modoki (EOF-2 of TEDIV), but the explained variance of this EOF is low (<9% for ERA-I data). Hence, the transitionary pattern with eastward propagating anomaly centers as found from LEDIV and DSEDIV is comparably weak in TEDIV. In terms of energy exchanges between ocean and atmosphere, the results suggest that noteworthy total energy exchanges occur only during canonical ENSO events, while El Niño Modoki-like conditions lead to circulation changes but only weak alteration of net surface fluxes and hence weak ocean/atmosphere energy exchanges. Moreover, these results suggest that El Niño Modoki is but part of the overall evolutionary patterns of ENSO, while other authors view El Niño Modoki as a distinct type of ENSO events (e.g., Ashok et al. 2007).

After exploration of the response of tropical atmospheric energy budgets to ENSO it appeared natural to extend the domain of research to the ocean to investigate if the response of tropical oceanic energy budgets to ENSO are quantitatively consistent with the results for the atmosphere found in Mayer et al. (2013). Another motivation for this part of the thesis were the results of Loeb et al. (2012) and Trenberth et al. (2014) showing that current OHC datasets practically fail to satisfy the constraint of replication of global mean OHC variability in variations of global mean net radiation at TOA. These results rose the question on which temporal and spatial scale the signal-to-noise ration of OHC data is high enough to provide meaningful results, especially if the energy exchanges between atmosphere and ocean in association with ENSO can be reasonably quantified on the scale of tropical ocean basins. Research goal (iii) was to answer these questions. This goal has been beyond reach a few years ago, but recent developments in ocean observation and analysis techniques have made this feasible.

Three state-of-the-art oceanic datasets ORAS4, HEN3, and Ensemble Coupled Data Assimilation system (ECDA, Zhang et al. 2007) were employed to compute OHC and its tendency (OHCT). Data from two atmospheric reanalyses were employed for evaluation of the atmospheric energy budgets. While ORAS4 and ECDA both use atmospheric fields as forcing fields, HEN3 is obtained purely from in-situ measurements in the ocean. Thus, HEN3 provides an estimate of OHC which is fully independent of the two employed atmospheric reanalyses ERA-I and MERRA. During the course of this study it was found that computation of the divergence of ocean heat transport (DIVFO) as a residual from OHCT and atmospheric fields, as done for example by (Trenberth and Fasullo, 2008), is too inaccurate to yield meaningful results when investigating interannual variability on a basin-averaged scale, mainly because of the accumulation of uncertainties from all fields in this term. Therefore, ocean heat transports directly computed from ORAS4 were used instead.

Using mainly an ordinary least squares regression method (again, using N34 as a proxy

for the ENSO state), quantitatively consistent exchanges between the tropical (30N-30S) Pacific, Atlantic and Indian Ocean and the atmosphere in association with ENSO could be shown (Mayer et al., 2014). It was found that the tropical Pacific ocean loses (gains) energy on the order of 0.26±0.07 PWK^{-1} during the peak of warm (cold) ENSO events, but Pacific ocean heat export across 30N and 30S as well as via the Indonesian Throughflow varies comparatively weakly. Consequently, the Pacific OHC loss (gain) must be realized through anomalous net surface fluxes and thus has to be replicated in atmospheric budgets if the datasets are consistent. Indeed, it was found that the tropical Pacific atmosphere responds with stronger (weaker) horizontal energy export (on the order of 0.20±0.04 PWK^{-1}) and net radiative flux at TOA responds with weaker (stronger) net energy input (on the order of 0.06±0.04 PWK^{-1}) than normal during El Niño (La Niña).

Stronger (Weaker) atmospheric energy export from the tropical Pacific region must lead to anomalous convergence (divergence) of atmospheric transports in other regions, because the global mean of TEDIV and also its anomalies is zero by definition. In Mayer et al. (2014) it is shown that TEDIV over the tropical Indian Ocean and the Atlantic responds conversely to ENSO when compared to Pacific Ocean TEDIV (consistent with Mayer et al. 2013), i.e., the atmosphere over the tropical Indian Ocean and the Atlantic exports less (more) energy than normal during warm (cold) ENSO events. In a next step it is shown that OHC changes of the Indian Ocean and the Atlantic are quantitatively consistent with the response of regional TEDIV to ENSO, i.e., Atlantic OHC increases (decreases) in association with El Niño (La Niña) and consistently accounts for the weakened (enhanced) atmospheric energy export from that region. The same is valid for the Indian Ocean, but with larger uncertainty bounds. In total, OHC increase (decrease) during the peak of El Niño (La Niña) in the tropical Atlantic and Indian Ocean accounts for about 85% of the OHC decrease (increase) in the tropical Pacific. Only the remaining small fraction of about 15% is exchanged at TOA (mainly via stronger OLR in the Pacific subtropics) and with the extratropics via atmospheric transports (in the zonal mean). The amount of energy exchanged at TOA over the tropical Pacific increases at positive lags (peaking at six months lag), but the regression coefficient remains below 0.10PWK^{-1}. This robust pattern of energy exchange between tropical ocean basins can be attributed to atmospheric circulation changes, especially the response of zonal circulation cells and associated remote responses of winds and surface fluxes to ENSO as described, for example, by Klein et al. (1999) or Lohmann and Latif (2007).

One main result of Mayer et al. (2014) is that compensating OHC exchanges between tropical ocean basins in association with ENSO explain the small (global and tropical) signal in net radiation at TOA found, for example, by Loeb et al. (2012) when compared to ENSO-related tropical Pacific OHC changes. Hence, ENSO leads to the well-known pronounced redistribution of OHC within the tropical Pacific (see, e.g., Roemmich and Gilson 2011), but it also leads

to a remarkable redistribution of OHC across the three tropical ocean basins, leading to a relatively small zonal mean OHC response to ENSO. Considering the tropical Pacific on its own for derivation of a conceptual picture of ENSO like the recharge/discharge-oscillator paradigm by Jin (1997) is certainly a valid approach and can describe very well the key processes in ocean and atmosphere associated with ENSO. However, from an energy budget standpoint, this is not sufficient and a conceptual picture of energy pathways through the ENSO cycle must involve all three tropical ocean basins, as OHC tends to oscillate between these basins and not only within the tropical Pacific. A first step in this direction is the schematic presented in Fig. 6 in Mayer et al. (2014) which at least involves the tropical Atlantic and Pacific oceans.

Another important implication of the results of Mayer et al. (2014) is the corroboration of the fact that correlation of zonal average tropical atmospheric energy export with ENSO is weak, which has already been found by Mayer and Haimberger (2012): While the response of TEDIV to ENSO is strong regionally, i.e., on a basin-averaged scale, strong zonal compensation leads to a comparatively weak zonal mean ENSO-response of TEDIV. The quantitatively consistent OHC changes in the respective basins, obtained from largely independent oceanic datasets, confirm the at first glance surprising result that ENSO-related energy exchange between tropics and extratropics is relatively small in the zonal average. However, it is important to note that anomalous energy exchanges between tropics and extratropics in association with ENSO are certainly strong regionally, as suggested by results of, e.g., Trenberth et al. (1998).

7 Outlook

The results presented in this thesis, especially of Mayer et al. (2013) and Mayer et al. (2014) motivate basically two ideas for future research. First, the exploration of coupled energy budgets is planned to be deepened. It is one big goal of climate diagnostics to quantify means and variations of energy fluxes through the earth's climate system. The results of Mayer et al. (2014) certainly represent a significant contribution to this aim. However, many interesting questions remain, especially concerning the ocean energy budget, for example regarding the partitioning of atmospheric and oceanic poleward heat transport in dependence of latitude or how variations of cross-equatorial transports in the atmosphere and ocean and the hemispheric energy balance at TOA interact. These questions have been addressed in theoretical, modeling and to some degree already in observational studies (see, e.g. Czaja and Marshall 2006, Bischoff and Schneider 2014, or Donohoe et al. 2014) but the recent development in ocean data assimilation and the tremendous improvement of the global ocean observing system since the introduction of ARGO in 2000 make a much more detailed assessment of these issues possible. Moreover, new reanalysis projects extending much further backward in time than the period considered throughout this thesis (starting in 1979), such as ECMWF's reanalysis project of the 20th century (ERA-CLIM), will allow to almost triple the length of the studied period.

A second future project is to apply the diagnostic tools developed in the course of the work for this thesis to output from coupled global climate models to check how realistically atmospheric and oceanic energy budgets in these models respond to ENSO, especially if the pathways of energy through the ENSO cycle in models agree quantitatively with the results of Mayer et al. (2014). Preliminary results with data from the Coupled Model Intercomparison Project Phase 5 (CMIP5) show at least qualitative agreement in some aspects, for example the energy exchange across tropical ocean basins is also seen from models. However, preliminary examination of tropical Pacific OHC variability in CMIP5 models in association with ENSO revealed quite substantial quantitative disagreement with reanalyses, especially in depths greater than 300m. The intensity of heat discharge during El Niño in ocean reanalyses diminishes with depth, nevertheless the signal extends far below 300m. In contrast, this area-averaged cooling during El Niño is not existent below 300m in CMIP5 models. Thus, ENSO as simulated by these models apparently affects a shallower layer of the tropical Pacific ocean than it seems to be the case in nature. This is an interesting result, especially in the light of the ongoing discussion concerning the apparent global warming hiatus (see, e.g. Meehl et al. 2011, Kosaka and Xie 2013, or England et al. 2014), as Balmaseda et al. (2013) showed that the strong El Niño in 1997/98, marking the beginning of the current hiatus period, was associated with excessively strong cooling of the deep tropical Pacific ocean - a process which current climate models apparently are not capable of simulating. These interesting first results are planned to be explored in more detail.

References

Ashok, K., Behera, S. K., Rao, S. a., Weng, H., and Yamagata, T. (2007). El Niño Modoki and its possible teleconnection. *Journal of Geophysical Research*, 112(C11).

Balmaseda, M. A., Mogensen, K., and Weaver, A. T. (2012). Evaluation of the ECMWF ocean reanalysis system ORAS4. *Quarterly Journal of the Royal Meteorological Society*, 139:1132 – 1161.

Balmaseda, M. A., Trenberth, K. E., and Källén, E. (2013). Distinctive climate signals in reanalysis of global ocean heat content. *Geophysical Research Letters*, 40:1754 – 1759.

Berrisford, P., Kållberg, P., Kobayashi, S., Dee, D., Uppala, S., Simmons, A. J., Poli, P., and Sato, H. (2011). Atmospheric conservation properties in ERA-Interim. *Quarterly Journal of the Royal Meteorological Society*, 137(659):1381–1399.

Bischoff, T. and Schneider, T. (2014). Energetic constraints on the position of the intertropical convergence zone. *Journal of Climate, in press*.

Bjerknes, J., J. (1969). Atmospheric teleconnections from the equatorial Pacific. *Monthly Weather Review*, 97(3):163–172.

Bollmeyer, C. and Hense, A. (2014). Inverse modeling of energy transports and budgets of the atmosphere. *Climate Dynamics*, pages 1–16.

Bryden, H. L. and Hall, M. M. (1980). Heat transport by currents across 25°N latitude in the Atlantic Ocean. *Science*, 207(4433):884–886.

Chiodo, G. and Haimberger, L. (2010). Interannual changes in mass consistent energy budgets from ERA-Interim and satellite data. *Journal of Geophysical Research*, 115(D2).

Clarke, A. J. (2008). *An introduction to the dynamics of El Niño and the Southern Oscillation*. Academic Press, 324pp.

Czaja, A. and Marshall, J. (2006). The partitioning of poleward heat transport between the atmosphere and ocean. *Journal of the atmospheric sciences*, 63(5):1498–1511.

Dee, D. and Uppala, S. (2009). Variational bias correction of satellite radiance data in the ERA-Interim reanalysis. *Quarterly Journal of the Royal Meteorological Society*, 135(644):1830–1841.

Dee, D. P., Uppala, S. M., Simmons, A. J., Berrisford, P., Poli, P., Kobayashi, S., Andrae, U., Balmaseda, M. A., Balsamo, G., and Bauer, P. (2011). The ERA-Interim reanalysis: Configuration and performance of the data assimilation system. *Quarterly Journal of the Royal Meteorological Society*, 137(656):553–597.

Donohoe, A., Marshall, J., Ferreira, D., Armour, K., and McGee, D. (2014). The inter-annual variability of tropical precipitation and inter-hemispheric energy transport. *Journal of Climate, in press*.

England, M. H., McGregor, S., Spence, P., Meehl, G. A., Timmermann, A., Cai, W., Gupta, A. S., McPhaden, M. J., Purich, A., and Santoso, A. (2014). Recent intensification of wind-driven circulation in the Pacific and the ongoing warming hiatus. *Nature Climate Change*, 4(3):222–227.

Fasullo, J. T. and Trenberth, K. E. (2008a). The annual cycle of the energy budget. part I: Global mean and Land-Ocean exchanges. *Journal of Climate*, 21(10):2297–2312.

Fasullo, J. T. and Trenberth, K. E. (2008b). The annual cycle of the energy budget. part II: meridional structures and poleward transports. *Journal of Climate*, 21(10):2313–2325.

Göber, M., Hagenbrock, R., Ament, F., and Hense, A. (2003). Comparing mass-consistent atmospheric moisture budgets on an irregular grid: An Arctic example. *Quarterly Journal of the Royal Meteorological Society*, 129(592):2383–2400.

Haimberger, L. (2007). Homogenization of radiosonde temperature time series using innovation statistics. *Journal of Climate*, 20(7):1377–1403.

Haines, K., Valdivieso, M., Zuo, H., and Stepanov, V. N. (2012). Transports and budgets in a 1/4° global ocean reanalysis 1989-2010. *Ocean Science Discussions*, 9(1).

Hantel, M., Brasseur, G., Cramer, W., Ehrendorfer, M., Emmons, L., Erhard, M., Gerten, D., Gouretski, V., Granier, C., and Haberlandt, U. (2005). Observed global climate, Vol. 6 of Landolt Börnstein New Series. Springer, 588pp.

Hantel, M. and Haase, S. (1983). *Mass consistent heat budget of the zonal atmosphere*. Dümmler, 84pp.

Held, I. M. (2001). The partitioning of the poleward energy transport between the tropical ocean and atmosphere. *Journal of the Atmospheric Sciences*, 58(8):943–948.

Ingleby, B. and Huddleston, M. (2007). Quality control of ocean temperature and salinity profiles – Historical and real-time data. *Journal of Marine Systems*, 65(1):158–175.

Jin, F. F. (1997). An equatorial ocean recharge paradigm for ENSO. Part I: Conceptual model. *Journal of the Atmospheric Sciences*, 54(7):811–829.

Johns, W. E., Baringer, M. O., Beal, L. M., Cunningham, S. A., Kanzow, T., Bryden, H. L., Hirschi, J. J. M., Marotzke, J., Meinen, C. S., and Shaw, B. (2011). Continuous, array-based estimates of Atlantic Ocean heat transport at 26.5°N. *Journal of Climate*, 24(10).

Klein, S. A., Soden, B. J., and Lau, N. C. (1999). Remote sea surface temperature variations during ENSO: Evidence for a tropical atmospheric bridge. *Journal of Climate*, 12(4):917–932.

Kosaka, Y. and Xie, S.-P. (2013). Recent global-warming hiatus tied to equatorial Pacific surface cooling. *Nature*, 501(7467):403–407.

Loeb, N. G., Lyman, J. M., Johnson, G. C., Allan, R. P., Doelling, D. R., Wong, T., Soden, B. J., and Stephens, G. L. (2012). Observed changes in top-of-the-atmosphere radiation and upper-ocean heating consistent within uncertainty. *Nature Geoscience*, 5(2):110–113.

Lohmann, K. and Latif, M. (2007). Influence of El Niño on the upper-ocean circulation in the tropical Atlantic Ocean. *Journal of Climate*, 20(19):5012–5018.

Lorenz, E. (1967). *Nature and Theory of the General Circulation of the Atmosphere*. WMO, 161pp.

Mayer, M. (2010). Corrected energy fluxes as evaluated from reanalysis data. Master's thesis, University of Vienna.

Mayer, M. and Haimberger, L. (2012). Poleward atmospheric energy transports and their variability as evaluated from ECMWF reanalysis data. *Journal of Climate*, 25(2):734–752.

Mayer, M., Haimberger, L., and Balmaseda, M. (2014). On the energy exchange between tropical ocean basins in association with ENSO. *Journal of Climate, in press*.

Mayer, M., Trenberth, K. E., Haimberger, L., and Fasullo, J. T. (2013). The response of tropical atmospheric energy budgets to ENSO. *Journal of Climate*, 26(2013):4710–4724.

Meehl, G. A., Arblaster, J. M., Fasullo, J. T., Hu, A., and Trenberth, K. E. (2011). Model-based evidence of deep-ocean heat uptake during surface-temperature hiatus periods. *Nature Climate Change*, 1(7):360–364.

Michaud, R. and Derome, J. (1991). On the mean meridional transport of energy in the atmosphere and oceans as derived from six years of ECMWF analyses. *Tellus A*, 43(1):1–14.

Nielsen, A. C. W. and Chen, T.-C. (1993). *Fundamentals of atmospheric energetics*. Oxford University Press, 400pp.

Oort, A. H. (1971). The observed annual cycle in the meridional transport of atmospheric energy. *Journal of the Atmospheric Sciences*, 28(3):325–339.

Peixoto, J. P. and Oort, A. H. (1992). *Physics of climate*. Springer, 520pp.

Pierrehumbert, R. T. (2010). *Principles of planetary climate*. Cambridge University Press, 680pp.

Rienecker, M. M., Suarez, M. J., Gelaro, R., Todling, R., Bacmeister, J., Liu, E., Bosilovich, M. G., Schubert, S. D., Takacs, L., and Kim, G. K. (2011). MERRA-NASA's Modern-Era Retrospective analysis for Research and Applications. *Bulletin of the American Meteorological Society*.

Roemmich, D. and Gilson, J. (2011). The global ocean imprint of ENSO. *Geophysical Research Letters*, 38(13):L13606.

Saha, S., Moorthi, S., Pan, H. L., Wu, X., Wang, J., Nadiga, S., Tripp, P., Kistler, R., Woollen, J., and Behringer, D. (2010). The NCEP climate forecast system reanalysis. *Bulletin of the American Meteorological Society*, 91(8):1015–1057.

Sorokina, S. A. and Esau, I. N. (2011). Meridional energy flux in the arctic from data of the radiosonde archive IGRA. *Izvestiya, Atmospheric and Oceanic Physics*, 47(5):572–583.

Stone, P. (2008). The atmospheric general circulation: Some unresolved issues. *Dynamics of Atmospheres and Oceans*, 44(3-4):244–250.

Trenberth, K. E. (2002). Evolution of El Niño-Southern Oscillation and global atmospheric surface temperatures. *Journal of Geophysical Research*, 107(D8):14.

Trenberth, K. E., Branstator, G. W., Karoly, D., Kumar, A., Lau, N.-C., and Ropelewski, C. (1998). Progress during TOGA in understanding and modeling global teleconnections associated with tropical sea surface temperatures. *Journal of Geophysical Research*, 103(C7):14291–14324.

Trenberth, K. E. and Caron, J. M. (2001). Estimates of meridional atmosphere and ocean heat transports. *Journal of Climate*, 14(16):3433–3443.

Trenberth, K. E., Caron, J. M., and Stepaniak, D. P. (2001). The atmospheric energy budget and implications for surface fluxes and ocean heat transports. *Climate Dynamics*, 17(4):259–276.

Trenberth, K. E. and Fasullo, J. T. (2008). An observational estimate of inferred ocean energy divergence. *Journal of Physical Oceanography*, 38(5):984–999.

Trenberth, K. E. and Fasullo, J. T. (2010). Simulation of present-day and twenty-first-century energy budgets of the southern oceans. *Journal of Climate*, 23(2):440–454.

Trenberth, K. E. and Fasullo, J. T. (2012). Tracking Earth's energy: from El Niño to global warming. *Surveys in Geophysics*, 33(3-4):413–426.

Trenberth, K. E., Fasullo, J. T., and Balmaseda, M. A. (2014). Earth's energy imbalance. *Journal of Climate, in press*.

Uppala, S. M., Kållberg, P. W., Simmons, A. J., Andrae, U., Bechtold, V. D. C., Fiorino, M., Gibson, J. K., Haseler, J., Hernandez, A., elly, G., Li, Y., Onogi, K., Saarinen, S., Sokka, N., Allan, R. P., Andersson, E., Arpe, K., Balmaseda, M. A., Beljaars, A. C. ., Berg, L. V. D., Bidlot, J., Bormann, N., Caires, S., hevallier, F., Dethof, A., Dragosavac, M., Fisher, M., Fuentes, M., Hagemann, S., Hólm, E., , Hoskins, B. J., Isaksen, L., Janssen, P. A. E. M., Jenne, R., McNally, A. P., Mahfouf, J.-F., Morcrette, J.-J., Rayner, N. A., Saunders, R., Simon, P., Sterl, A., Trenberth, K. E., Untch, A., Vasiljevic, F., Viterbo, P., and Woollen, J. (2005). The ERA-40 re-analysis. *Quarterly Journal of the Royal Meteorological Society*, 131:2961–3012.

von Storch, H. and Zwiers, F. W. (2002). *Statistical analysis in climate research*. Cambridge University Press, UK, 484pp.

Vonder Haar, T. H. and Oort, A. H. (1973). New estimate of annual poleward energy transport by northern hemisphere oceans. *Journal of Physical Oceanography*, 3(2):169–172.

Wielicki, B., Barkstrom, B., Harrison, E., Lee, R., Smith, G., and Cooper, J. (1996). Clouds and the Earth's radiant energy system (CERES): an Earth observing system experiment. *Bulletin of the American Meteorological Society*, 77(5):853–868.

Zhang, S., Harrison, M. J., Rosati, A., and Wittenberg, A. (2007). System design and evaluation of coupled ensemble data assimilation for global oceanic climate studies. *Monthly Weather Review*, 135(10):3541–3564.

Zhang, Y. (2004). Calculation of radiative fluxes from the surface to top of atmosphere based on ISCCP and other global data sets: Refinements of the radiative transfer model and the input data. *Journal of Geophysical Research*, 109(D19):1–27.

Acknowledgements

First of all, I am greatly indebted to my advisor Leo Haimberger. He helped me to design and develop the study presented in this thesis, and he gave me free rein to pursue my own ideas. Leo always took the time for discussion of results and technical difficulties, and he was also a great supporter in other matters such as my application for my stay at NCAR. That is certainly not to be taken for granted. Moreover, Leo gave me the opportunity to be employed within his research projects.

I would also like to thank Magdalena Balmaseda, Kevin Trenberth, John Fasullo and Dennis Shea, who all helped me a lot regarding scientific and technical aspects during various stages of my work.

This is also the right place to thank my friends and family for highlighting and discussing other things in life than this thesis. Special thanks go to my parents, who supported my goal to become a meteorologist and made my studies possible financially.

Last but not least, thanks go to Teresa, for supporting me with her design skills [she designed Fig. 1 of this thesis and Fig. 6 in Mayer et al. (2014)], for being understanding when I was absorbed in thought about (in a non-climatologist's view) obscure things, and for being a true sunshine.

Curriculum vitae

Personal Data

Name:	Mag. Michael Mayer
Nationality:	Austria
Date of birth:	23 December 1984
Place of birth:	Kirchdorf/Krems
Addresse:	Gentzgasse 2/1, A-1180 Vienna
e-Mail:	mima@univie.ac.at

Education

1990 – 1994	Elementary school in Pettenbach
1994 – 2003	Secondary education at "Stiftsgymnasium der Abtei Schlierbach"
06/2003	Examinations for university entrance (equivalent to A–levels)

Studies

10/2003 – 09/2004	Studies of Regional Development at TU Vienna
10/2003 – 09/2006	Studies of organ at Anton Bruckner Private University (teacher: Brett Leighton)
10/2004 – 08/2010	Studies of Meteorology at University of Vienna, course specialization in Theoretical Meteorology; Title of diploma thesis: "Corrected energy fluxes as evaluated from reanalysis data" (advisor: Prof. Leopold Haimberger); academic degree: Magister (equivalent to Master's degree)
since 10/2010	Doctoral program in natural sciences at University of Vienna; Working title of doctoral thesis: "Low–frequency variability in global energy budgets" (advisor: Prof. Leopold Haimberger)

Work experience

09/2008	Weather forecasting at "Blue Sky Wetteranalysen"
Since 09/2009	Project staff member at the Department of Meteorology and Geophysics, University of Vienna
02/2011 – 07/2011	ASP Graduate Visitor at CAS at NCAR, Boulder, Colorado (advisor: Kevin Trenberth)

Teaching experience

SS 2012 and SS2014	Instructor in exercise course on climate diagnostics and forecasting

Training courses

09/2009	ECMWF Seminar on Diagnosis of Forecasting and Data Assimilation Systems - ECMWF, Reading, UK
08/2013	Community Earth System Model Tutorial 2013 - NCAR, Boulder, Colorado, USA

Practical trainings

04/2008	Glacier mass balance evaluation at Mount Sonnblick

Publications

– Mayer, M., Haimberger, L., and Balmaseda, M. A., 2014: *On the energy exchange between tropical ocean basins related to ENSO*. Journal of Climate, in press.

– Mayer, M., Trenberth, K. E., Haimberger, L, and Fasullo, J. T., 2013: *The Response of Tropical Atmospheric Energy Budgets to ENSO*. Journal of Climate, 26, 4710–4724.

– Mayer, M., and Haimberger, L., 2012: *Poleward atmospheric energy transports and their variability as evaluated from ECMWF reanalysis data*. Journal of Climate, 25, 734–752.

Presentations

Posters:

2013	*"ENSO in CMIP5 models from an energy budget perspective – Comparison to ocean and atmosphere reanalyses"* at 4th WGNE workshop on systematic errors in weather and climate models, Exeter, UK
2012	*"Zonal Structure of anomalies in tropical atmospheric energy budgets"* at 4th International Conference on Reanalyses, Silver Spring, Maryland, USA
2011	*"Variability of poleward atmospheric energy transports as evaluated from reanalyses"* at European Geosciences Union Meeting, Vienna (presented by Leo Haimberger)

Oral Presentations:

2013	*"Tacking energy budget anomalies through the ENSO cycle"* at 13th EMS Annual Meeting and 11th European Conference on Applications of Meteorology, Reading, UK
2013	*"Kombinierte Auswertung atmosphärisch-ozeanischer Energiehaushalte"* at DACH, Innsbruck, Austria

2012	*"Estimating uncertainty of reanalyses using energy budget diagnostics"* at ERA-CLIM Workpackage 4 Workshop on observation errors , Vienna, Austria
2011	*"Temporal homogeneity of energy budget relevant datasets"* at NCAR, Boulder, Colorado
2011	*"Variabilität atmosphärischer Energiehaushalte aus Reanalysen"* at Austrian Meteorological Society meeting, Klagenfurt, Austria
2010	*"Korrigierte meridionale Energieflüsse aus Reanalysedaten"* at DACH, Bonn, Germany

Specialized knowledge

Operating Systems	GNU/Linux Windows (XP, 7, 8) Mac OS X
Programming Languages	Matlab NCAR Command Language (NCL) Interactive Data Language (IDL) LaTeX Knowledge in Fortran 95, Linux Shell Script
Special Software Skills	MS Office (Word, Excel, PowerPoint) Adobe Illustrator VirtualBox
Languages	German (native) English (C1 Level) French (A2 Level)